$\mathbf{Fe_{1-x}Cu_xCr_2S_4}$ Studied by Mössbauer Spectroscopy and Muon Spin Rotation and Relaxation

Von der Fakultät für Elektrotechnik, Informationstechnik, Physik
der Technischen Universität Carolo-Wilhelmina zu Braunschweig

zur Erlangung des Grades einer Doktorin

der Naturwissenschaften (Dr. rer. nat.)

genehmigte Dissertation

von Elaheh Sadrollahi

aus Damghan

eingereicht am: 03.05.2018

mündliche Prüfung am: 14.08.2018

1. Referent: Prof. Dr. F. J. Litterst

2. Referent: apl. Prof. Dr. S. Süllow

3. Referent: Prof. Dr. A. Hangleiter

Druckjahr: 2018

Dissertation an der Technischen Universität Braunschweig,
Fakultät für Elektrotechnik, Informationstechnik, Physik

Zusammenfassung

Ziel dieser Doktorarbeit ist eine systematische Untersuchung des Magnetismus und der Orbitalzustände im Thiospinellsystem $Fe_{1-x}Cu_xCr_2S_4$ über die lokalen Sondenmethoden ^{57}Fe Mössbauerspektroskopie und Myonenspin rotation und - relaxation (μSR) sowie Standardmagnetisierungsmessungen. Während die über Mössbauereffekt gemessenen Hyperfeinwechselwirkungen Informationen zu Valenzzustand, Symmetrie der lokalen Koordination und das magnetische Moment des Eisens liefern, befinden sich die für μSR verwendeten positiven Myonen μ^+ auf Zwischengitterplätzen, vermutlich nahe bei Schwefel, und sind sensitiv auf lokale Magnetfelder und deren durch magnetische Ionen verursachte Fluktuationsdynamik.

Mössbauer- und μSR-Spektren der Serie $Fe_{1-x}Cu_xCr_2S_4$ ($0,1 \leqslant x \leqslant 0,9$) wurden über einen weiten Temperaturbereich aufgenommen und ausgewertet. Dabei wurden auch Daten aus früheren Messungen einbezogen, die neu analysiert wurden, um ein vollständigeres Bild zu erhalten.

Die Kupferkonzentrationsabhängigkeit der relativen spektralen Beiträge von zwei- und dreiwertigem Eisen zu den Mössbauerspektren kann durch eine statistische Verteilung von Cu auf den nächsten Tetraedernachbarplätzen von Eisen in dem Spinellgitter erklärt werden. Die nichtverschwindenden Fe^{2+} Beiträge oberhalb $x = 0,5$ deuten auf die Bildung von Cu^{2+}. Diese ist im Gegensatz zu gängigen und kontrovers diskutierten Modellen zu den Valenzen der Kationen in $Fe_{1-x}Cu_xCr_2S_4$, ist jedoch in Übereinstimmung mit einem früheren von Goodenough vorgeschlagenen Modell.

Die temperaturabhängige Entwicklung der elektrischen Quadrupolwechselwirkung und der magnetischen Hyperfeinwechselwirkung an $^{57}Fe^{2+}$ erlaubt es, die magnetisch induzierte Aufspaltung des e_g Orbitalgrundzustands von Fe^{2+} und die Entwicklung eines dynamischen Pseudo-Jahn-Teller-Effekts zu verfolgen, der wiederum die Spinstruktur durch eine Veränderung der magnetischen Anisotropie beeinflusst.

Die Temperaturabhängigkeiten der spontanen Myonenrotationsfrequenzen und Relaxationsraten zeigen mehrere Übergänge über den gesamten Konzentrationsbereich x. Für $x \geqslant 0,5$ konnten diese Veränderungen nicht mehr über Mössbauerspektroskopie an Fe^{2+} nachgewiesen werden, da die Tetraederplätze dominant von Fe^{3+} besetzt sind, das nicht Jahn-Teller aktiv und insensitiv auf Änderungen in den Orbitalzuständen ist. Die wesentlichen Informationen in diesem Konzentrationsbereich ergeben sich aus μSR.

Die Änderungen in der magnetischen Ordnung und der Spindynamik für $x \geqslant 0,5$ deuten auf eine Spinumorientierung der Cr^{3+} und/oder Cu^{2+} Momente. Mögliche Ursachen sind Orbitaleffekte, jetzt allerdings verursacht durch Jahn-Teller Effekt in den t_{2g} Orbitalen von Cu^{2+}.

Die beobachteten Veränderungen in der magnetischen Struktur und in den Orbitalzuständen werden im Zusammenhang mit den Isolator-Metallübergangs des $Fe_{1-x}Cu_xCr_2S_4$ Systems diskutiert. Oberhalb des Isolator-Metallübergangs lässt sich über Nullfeld-μSR eine besondere Entwicklung der Spindynamik verfolgen. Im metallischen Bereich wer-

den koexistierende rasch und langsam relaxierende Beiträge gefunden, die leitenden und isolierenden Gebieten zugeschrieben werden. Diese Inhomogenität in der kollinearen Spinstruktur tritt in einem Temperaturbereich auf, in dem ein Kolossaler Magnetowiderstand beobachtet wird. In diesem System wird dieser üblicherweise über Austauschmechanismen und eventuell Jahn-Teller-Effekt erklärt. Nach unseren μSR Ergebnissen scheint auch das inhomogene dynamische Ladungs- und Spinsystem eine Rolle zu spielen, ähnlich zu den Beobachtungen im System $(\mathrm{La},\mathrm{Ca})\mathrm{MnO}_3$.

Schließlich war es möglich, ein Phasendiagramm für die magnetischen und orbitalen Zustände zu entwerfen. Das Zusammenwirken von Spin-, Ladungs- und Orbitalwechselwirkungen führt zu mehreren Spinumorientierungen.

Abstract

Aim of this thesis is a systematic investigation of the magnetism and orbital states in the thio-spinel system $Fe_{1-x}Cu_xCr_2S_4$ by means of the local probe methods of ^{57}Fe Mössbauer spectroscopy and Muon Spin Relaxation and Rotation (μSR) and standard magnetization measurements. While the Mössbauer hyperfine interactions give information on the iron valence state, symmetry of local coordination and the magnetic moment of iron, positive muons μ^+ used for μSR are positioned at interstitial sites supposedly close to sulfur and are sensitive to local magnetic fields and their fluctuation dynamics due to the magnetic ions.

Mössbauer and μSR spectra of the series $Fe_{1-x}Cu_xCr_2S_4$ ($0.1 \leqslant x \leqslant 0.9$) have been collected over a wide temperature range and were analyzed. Also earlier data from previous investigations have been included, re-analyzed and discussed for reaching a more complete view.

The dependence of the relative spectral contributions by divalent and trivalent iron to the Mössbauer spectra on Cu concentration can be explained by a random distribution of Cu among the tetrahedral nearest neighbor sites of the iron in the spinel lattice. These non-vanishing contributions Fe^{2+} even beyond x = 0.5 indicate the presence of Cu^{2+}. This is in contrast to current, controversially discussed models for the valencies of cations in $Fe_{1-x}Cu_xCr_2S_4$, yet in agreement with an earlier one proposed by Goodenough.

The temperature dependent development of electric quadrupole and magnetic hyperfine interaction at $^{57}Fe^{2+}$ allows following the magnetically induced splitting of its e_g orbital ground state and the development of a dynamic pseudo Jahn-Teller effect that is affecting the spin structure due to a change in magnetic anisotropy. The temperature dependence of the spontaneous muon spin rotation frequencies and relaxation rates indicate the presence of several transitions for the whole concentration range x. For $x \geqslant 0.5$, these changes could not be traced by Mössbauer spectroscopy since the tetrahedral sites are dominantly occupied by Fe^{3+} that is Jahn-Teller inactive and therefore insensitive to changes in orbital states. In this concentration range the essential information comes via μSR. The changes in magnetic order and spin dynamics for $x \geqslant 0.5$ point to spin re-orientation connected with Cr^{3+} and/or Cu^{2+} moments. Possible origin may be orbital effects, now however due to a Jahn-Teller effect in the t_{2g} orbitals of Cu^{2+}.

The observed changes in magnetic structure and orbital states are discussed in relation to the insulator-metal transitions observed in $Fe_{1-x}Cu_xCr_2S_4$. Zero-field μSR allowed to trace peculiar spin dynamics above the insulator-metal transition. In the metallic regime a coexistence of fast and slow relaxing contributions are found that are related to conducting and insulating regions. This inhomogeneity in the collinear spin structure occurs in a temperature range where colossal magenetoresistance is found in this system. In this system, this effect is usually explained with exchange mechanisms and eventual Jahn-Teller effect. From our μSR data also the inhomogeneous dynamic charge and spin system appears to play a role, similar to observations in the system $(La, Ca)MnO_3$.

Finally, it was possible to design a tentative magnetic and orbital phase diagram. The interplay of spin, charge, and orbital interactions leads to several spin re-orientations.

Contents

Chapter 1

Introduction

The synthesis and investigation of $Fe_{1-x}Cu_xCr_2S_4$ have been started since the 1960s. This thio-spinel system has attracted attention due to its electronic and magnetic properties. The magnetic coupling between Fe^{2+} and Cr^{3+} in the undoped compound is complicated by frustration (e.g. Kalvius et al. [2010], Krimmel et al. [2006]). Further complications arise from the Jahn-Teller active Fe^{2+} in tetrahedral coordination leading to orbital order and also influencing the spin structure (e.g. Fichtl et al. [2005], Kalvius et al. [2008], Tsurkan et al. [2010]).

Cu doping results in an increase of ordering temperature and the ferrimagnetic semiconductor turns to a metallic ferromagnet for $CuCr_2S_4$. Various models how cation valencies are changing upon *Cu* doping, are under controversial discussion. No systematic investigation of the magnetic behavior and its relation to orbital ground state properties in dependence on Cu doping exists.

This was the motivation for the here presented thesis using the local probe methods of Mössbauer spectroscopy and μSR. Mössbauer spectroscopy probes valency, magnetism, and orbital state of Fe. μSR gives a picture from an interstitial site viewing magnetic field and their fluctuations caused by all involved cations, i.e. Fe, Cr, and eventually Cu.

We will show that there is an interplay between magnetic exchange interaction and orbital effects that are strongly influenced by Jahn-Teller distortions. We finally will be able to suggest a tentative magnetic/orbital phase diagram. Our μSR data also propose a relation between the observed relaxation behavior with metal-insulator transition and CMR effects.

The presented thesis is structured as follows:

- chapter 1 briefly introduces to the structural and magnetic properties of spinels together with a short introduction of Jahn-Teller effect and possible magnetic interaction mechanisms;
- chapter 2 will give a short description of the experimental methods used in this work. The aim is to explain why we use these characterization methods and what we can learn from using them;
- chapter 3 is a review of what is known from these compounds by now, which helps the reader to get an overview of many open questions related in this system;
- in chapter 4 the results collected from magnetization measurement, Mössbauer spectroscopy, and μSR are presented;
- in chapter 5 the results derived from each experimental method are discussed and compared in order to explain the changes and transitions in the temperature dependence of parameters. We get information about the valence state, orbital and spin structure, and the conduction mechanism, which has been under debate for long time;

- finally, in chapter 6 we introduce a magnetic phase diagram as a main conclusion and sum up the main results.

Chapter 2

General Properties of Spinel Compounds

2.1

Structural Properties of Spinel

Numerous compounds with the general formula AB_2X_4 have the same structure as the mineral $MgAl_2O_4$, spinel, which originally was referred to as red gemstone. The mineral gemstone $MgAl_2O_4$ exists with a crystal lattice, which has now simply been termed the spinel structure (Fig. 2.1).
Spinel itself belongs to a much bigger family, which occurs naturally. Starting with the mineral spinel $Mg^{2+}Al_2^{3+}O_4$ one may substitute Mg^{2+} and Al^{3+} with a wide range of divalent and trivalent cations. Hence, the general chemical formula for the spinel compounds is $A^{2+}B_2^{3+}X_4^{2-}$ where the A-sites often include divalent cations and the B-sites trivalent ones. The X represents the oxygen and chalcogen ions. Spinels with sulfur are called Thiospinels. For the first time, Bragg [1915] and Nishikawa [1915] determined the spinel structure which belongs to the space group O_h^7 (Fd3m). The "normal" spinel structure is shown in Fig. 2.1 which is based on a cubic close-packed structure of O^{2-} anions introducing two types of interstitial positions. One is the A-site which is coordinated tetrahedrally with point symmetry 43m; the octahedral B-sites have point symmetry m3m.

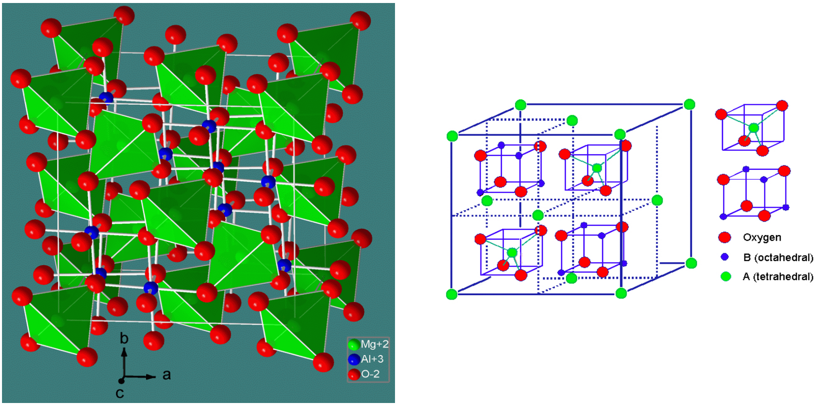

Figure 2.1: Crystal structure of spinel (left). A tetrahedral sites with four and B octahedral sites with six nearest neighbor oxygen (right) (taken from Wikibooks [2017]).

Each anion in the spinel structure is surrounded by one A- and one B-cation. The distribution of the cations, divalent and trivalent, among the two sites A, B may vary between normal spinel (divalent on A site, trivalent on B site) and inverse spinel (divalent and trivalent on B site, trivalent on A site). The cation distribution is influenced by several energy terms such as (Sickafus et al. [1999]):

- anions and cations exhibit repulsion and attraction due to electrostatic energy. This energy term implies that the A-site is occupied by either large ions with low charge or small ions with high charge;
- on the same sublattice, there exists an ordering energy between different ions. This energy term happens when two transition metals sit on the same site, which is not our case. In $Fe_{1-x}Cu_xCr_2S_4$, Fe and Cr sit in different sites;
- site preference energy of certain ions. Some ions show a pronounced preference for certain coordination numbers, e.g. Fe^{2+} for tetrahedral and Cr^{3+} for octahedral coordination.

The site preference of spinel structure results from the difference between the stabilization of this ion on B-sites and that on A-sites. The site preference has been deduced by the electrostatic model (Dunitz and Orgel [1957], McClure [1957]) given in the following:

- octahedral site preference: ions with d^3 configuration
- no site preference: ions with d^0, d^1, d^2, d^4, d^8 configuration
- tetrahedral site preference: ions with d^5, d^6, d^7, d^9, d^{10} configuration.

In our case of $Fe_{1-x}Cu_xCr_2S_4$, the energy stabilization and electrostatic interaction play an important role, which will be explained in the following to investigate the novel ground state of this material.

2.1.1

Crystal Field and Jahn-Teller Effect

In order to better understand the orbital physics, which is directly related to orbital ordering in $Fe_{1-x}Cu_xCr_2S_4$, we need to have more information about the Jahn-Teller effect that is essential to explain the electronic and magnetic ground states in these compounds.

In the spinel structure, the five d levels of transition metals are responsible for orbital ordering and other peculiar ground states. It is well-known that the degeneracy of the five d orbitals is removed by the crystal field caused by the electrostatic interaction between d orbitals of the cations and p orbitals of nearby anions (Goodenough [1968]).

Fig. 2.2 shows the splitting of the five degenerate d levels of A tetrahedral and B octahedral sites into two levels by the crystal field. One is the triplet (t_{2g}[1]) which consists of d_{xy}, d_{yz}, and d_{zx} levels, and the other is doublet (e_g) which consists of the d_{z^2} and $d_{x^2-y^2}$ levels.

---

[1] The subscript "g" is not used in tetrahedral environment because it indicates an inversion symmetry which is absent in the tetrahedral environment

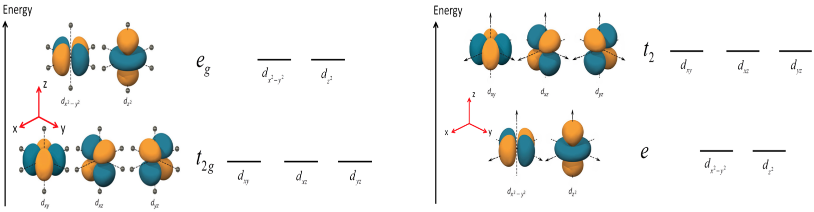

Figure 2.2: Energy splitting of the octahedral environment due to electrostatic interactions (left). Energy splitting of the tetrahedral environment (right). In contrast to the octahedral environment, the e orbitals have a lower energy compared to the t$_2$ orbitals (adopted from The Chemistry LibreTexts library [2017]).

Firstly, the lower energy orbitals will be filled by the electrons, but there is an energy consideration due to the splitting which leads to introduce high-spin and low-spin configurations. The important point of the orbital filling in our case is whether an uneven orbital occupation among degenerate orbitals is present or not. In our case, i.e. Fe$_{1-x}$Cu$_x$Cr$_2$S$_4$ (at least for $x \lesssim 0.5$, where iron is dominantly in the Fe^{2+} state), an uneven orbital filling is given by for Fe^{2+} ($3d^6$) in tetrahedral environment. Due to this unequal filling, the fully occupied orbitals experience a stronger repulsion which cause the structural distortion. A structural distortion results: the lifting of the degeneracy of either t$_2$ or e orbitals due to uneven orbital occupation among degenerate orbitals and is known as the Jahn-Teller effect which states that a non-linear molecule in an electronic state with orbital degeneracy will distort so as to lower its symmetry and remove the degeneracy (Goodenough [1964]). In the case of Fe$_{1-x}$Cu$_x$Cr$_2$S$_4$ both Fe and Cu are expected to behave as Jahn-Teller active ions, if their valence states are Fe^{2+}(d^6) and Cu^{2+}(d^9) (the Fe^{2+} ion with S = 2 has a hole in the lower doublet).

2.2

Magnetic Properties

2.2.1

General Magnetic States

The magnetic behavior of materials may roughly be classified as ferromagnetic, ferrimagnetic, antiferromagnetic, paramagnetic, and diamagnetic. More complex magnetic arrangements are, e.g., spin glasses with random spin orientation.

Diamagnetic materials consist of atoms that originally or through the binding have filled electron shells and therefore do in principle not show any magnetism. However, when applying a magnetic field a small negative susceptibility is observed, which can be qualitatively understood by Lenz's law.

Paramagnetic materials consist of atoms having partially filled shells giving rise to magnetic moments. These moments are in fact subject to thermal agitation, possessing only a net moment in a magnetic field. This gives a susceptibility $\chi = \mathrm{M/H}$, which, in the case of not too high magnetic fields, follows the well-known Curie law, $\chi = \mathrm{C/T}$, with C the Curie constant dependent on the kind of magnetic atoms. However, the magnetic atoms are rarely free of magnetic interactions and the temperature behavior is then expressed by the Curie-Weiss law $\chi = \mathrm{C}/(\mathrm{T} - \theta)$ where θ is a positive value in the case of magnetic interaction tending to align the atomic moments in the same direction and a negative value in the opposite case. When strong magnetic interactions between the paramagnetic atoms occur, the materials become magnetically ordered below a certain temperature.

If the atomic moments tend to align parallel, the material is ferromagnetic. If on the other hand, the moments tend to align antiparallel in equal amounts we speak of antiferromagnetism. However, there exists also the possibility, in which the moments align antiparallel, but, are not equal. In that case the materials are called ferrimagnetic.

This ferrimagnetism was discovered and described in the late forties of the previous century by Néel (1948). Hereby, spinel compounds were the first examples of ferrimagnetism, in which such magnetic behavior of two sublattice systems with unequal and antiparallel moments are present. In the theoretical description of this ferrimagnetism, based on the concept of the Weiss molecular field, it was suggested that the magnetic interactions between the sublattices are negative, favoring antiparallel arrangements, and predominate over the magnetic interactions within each sublattice. However, it has later been shown that the interactions within a sublattice are often comparable to the inter-sublattice interactions leading to much more complicated magnetic structures as outlined in the next sections.

Note that here only a small selection of concepts describing the microscopic origin of magnetism can be given. Issues that are important for the present work are emphasized. For further studies please refer to appropriate literature, for example Blundell [2001].

2.2.2

Magnetic Exchange Interactions

In spite of the fact that an electron with its spin can be looked at as a small magnet, the alignment of spins cannot be originated by a classical dipolar magnetic interaction of spins. Compared with the electric interactions, the direct magnetic interaction is too small. In fact the origin of the spin alignment is purely quantum mechanical. Its origin is the Pauli exclusion principle found by Wolfgang Ernst Pauli in 1925 and the exchange interaction discovered by Werner Heisenberg and P. A. M. Dirac in 1926.

The Pauli exclusion principle expresses that ”the total wavefunction is antisymmetric for a system of identical fermions (particles with half-integer spin)”. In many cases it is possible to separate the total wavefunction in the position-space wavefunction and the spin wavefunction. If one now supposes a symmetric position-space wavefunction, with the electrons located at the same position, the spin wavefunction has to be antisymmetric according to get an antisymmetric total wavefunction, meaning the spins of two electrons are antiparallel aligned. In the case of parallel alignment of spin the position-space wavefunction should be antisymmetric. That is to say, the Pauli exclusion principle declares that two electrons are not allowed to be identical in their spin direction and position, thus in all their quantum numbers.

The exchange interaction is a logical result of the Pauli exclusion principle. The wavefunction of identical neighboring particles can overlap. The Pauli principle implies that the two electrons can be aligned parallel or antiparallel, but it does not favor one configuration. The system energetically prefers a configuration in which the average distance between the electrons is higher due to the Coulomb repulsion with an antisymmetric position-space wavefunction causing the parallel alignment of the spins. Therefore the exchange interaction cannot be assigned the meaning of a force, but as a quantum mechanical effect. The exchange Hamiltonian can be given by

$$\hat{H} = -2J_{ij} \sum_{i,j} S_i . S_j \tag{2.1}$$

It directly causes the Hund’s rules and in many cases ferromagnetism. In solids the exchange interaction also can cause antiferromagnetic ordering of the electron spins. The reason for it, can be the distance between the atomic nuclei. If the atomic distances are very small, it is energetically preferable that the electrons are located between the atomic cores to reduce the repulsive force of the positive nuclei. Consequently a symmetric position-space wavefunction results and therefore an antiferromagnetic ordering of the spins. Also some other additional phenomena like for instance the *superexchange* or the *double-exchange* can influence and dominate the spin alignment in a solid. In the following these mechanisms are presented.

2.2.2.1
Superexchange Interaction and Double-Exchange Interaction

The difference between the superexchange and the above described direct exchange is that the direct exchange is coupling between nearest neighbor cations not involving an intermediary anion. Kramers [1934] observed that the Mn atoms in MnO interact with each other despite having intermediary non-magnetic oxygen atoms. He suggested an exchange interaction that occurs via a non-magnetic ligand, the so called superexchange interaction. Later Anderson [1950] explained that the magnetic exchange mechanisms in insulators occur by superexchange.

Kanamori [1959] showed the dependence between the sign of superexchange interaction and the cation orbital state on the crystalline field, which arises from octahedrally and tetrahedrally surrounding anions that influence the cations. There is a considerable overlap between the orbitals of cations and that of the anions, but some orbitals are orthogonal. This leads to ferromagnetic or antiferromagnetic superexchange interactions which depend on the 3d electron number of the involved cations and also the bonding angles between the ligands and the cations. Many studies show that the dominant magnetic interactions in the spinel structure are 125° A-X-B interaction, 90° B-X-B interaction and direct B-B interaction, for example the interaction between Cr^{3+} in an octahedral site via oxygen is ferromagnetic via 90° interaction, while it is antiferromagnetic, if they interact via 180°. The magnetic ordering, found in $Fe_{1-x}Cu_xCr_2S_4$ studied in this thesis, is ferrimagnetic.

There is still an another mechanism, which can affect the spin alignment. It is different from the direct exchange and superexchange interaction: the so called double-exchange which was introduced by Zener [1951]. This mechanism is related to the exchange of electrons between the cations. The double-exchange refers to situations where electron hopping between the cations is energetically more favorable than a change of spin direction in order to conform with Hund's rules.

It should be mentioned here that the spin alignment in the direct exchange and superexchange occur between the same valence states of atoms, while double- (and eventually triple-) exchange are only between atoms with different valence states.

Chapter 3

Characterization Methods

In following section there will be briefly introduced the methods used by us for studying $Fe_{1-x}Cu_xCr_2S_4$. The main goal, is to express why we use these methods and what we can learn from them.

3.1

Magnetization Measurements

Magnetization measurements are a global technique, where the total magnetization is recorded. In the work presented here, the magnetization measurements have been carried out in a SQUID magnetometer. Its output is the molar susceptibility χ_M = MZ/Hm. where Z is the formula/molecular mass of sample, M is the magnetization, H is applied field and m is the mass of the sample.

What we can learn from the magnetization and susceptibility data of our samples:

- one can calculate the magnetic moment (μ_{eff}) from the magnetic susceptibility (χ) of a sample;
- the nature of magnetism in material, be it antiferromagnetic, ferromagnetic, or paramagnetic from the temperature and field dependent susceptibility measurements;
- the Curie temperature T_c for each concentration and its variation with the Cu concentration and also temperature;
- tracing eventual changes in magnetic structure (as suspected for $FeCr_2S_4$ around T_m = 60 K);
- eventual indication for orbital ordering (as suspected for $FeCr_2S_4$ around $T_{oo} \sim 10$ K);
- eventual occurring spin-glass or orbital-glass state;

An important way to study the temperature dependence of the magnetic susceptibility data is to compare zero field cooling (ZFC) and field cooled (FC) data. ZFC, i.e. cooling the sample without any applied magnetic field to the desired temperature, M then measured upon warming in an applied field. FC, i.e. cooling the sample in applied magnetic field to the desired temperature, then the data can be collected during heating. Splitting of the ZFC and FC curves is a sign for presence of the irreversible magnetization processes.

3.2

Mössbauer Spectroscopy

Mössbauer spectroscopy is a spectroscopic technique based on the recoil-free γ-ray resonant absorption and emission in solids. Rudolf Mössbauer during his doctoral thesis in 1957 observed this resonant absorption and emission, which is named the Mössbauer effect in his honor. And hence he became a winner of the Nobel Prize in Physics in 1961 (Mössbauer [1962]).

Mössbauer spectroscopy is a versatile tool to describe via the hyperfine interactions, the valence state and the electron density at the iron nucleus as well as the spin state and also the symmetry of the surrounding atoms. With considering these capabilities, using this method in our work is very instructive to get some information about magnetic and orbital structure, the long standing problem of electronic configuration and its ground state.

A description of the theory behind the Mössbauer effect has been, e.g., reported by Mössbauer [1962] and Gütlich et al. [2011], and will not be described in detail here. For Mössbauer nuclei (^{57}Fe) a transmission from a ground state to an excited nuclear level may occur by absorption of a γ quantum, and vice versa an emission from the excited to the ground state level. In case of a free nucleus the γ-ray does not have enough energy to be absorbed by another nucleus of the same type undergoing a transition between the same states due to recoil energy; the recoil energy is high and the resonant absorption will be suppressed. As Rudolf Mössbauer proposed, for emitting and absorbing atoms in a solid lattice resonant absorption can be observed. There the recoil energy can only be transformed into phonons. At low temperature these can be excited only to a low extent and the recoil is transferred to the large mass of the crystal. Therefore, the recoil energy at the nucleus is negligible. The probability of the recoil-free processes is characterized by the Lamb-Mössbauer factor (f) which is increasing with decreasing of temperature (less probable excitation of phonon) and γ-ray energy.

When the atoms are bound in a lattice, nuclear energy levels have very small shifts or are split by hyperfine interactions. Relative motion between the source (emitter) and the absorber (our compound) by use of Doppler effect allows an energy scan to resolve different absorption lines. A Mössbauer spectrum is represented by the plot of the γ-ray transmission through the absorbing sample as a function of Doppler velocity which is correlated to the γ ray energy.

The resonant absorption peaks change between different compounds and reflect details of the environment of the Mössbauer atoms (e.g. of Fe in $Fe_{1-x}Cu_xCr_2S_4$ compounds). The positions and intensities of absorption lines give information about the hyperfine interactions: chemical shift CS, nuclear electric quadrupole hyperfine interaction (or quadrupole splitting QS), magnetic dipole hyperfine interaction (or magnetic hyperfine field B_{hf}).

In the following, we will briefly introduce these hyperfine interactions in general and relate to what would can be expected for the analysis of our data.

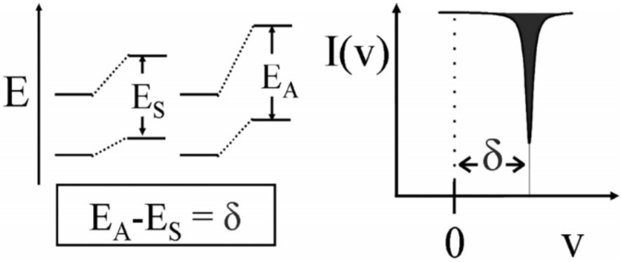

Figure 3.1: Energy difference between E_S and E_A in the source and absorber is given by the isomer shift δ (left). The difference of the transition energies appears in the spectrum as the shift from the zero Doppler velocity (adopted from Gütlich [2012]).

3.2.1

Electric Monopole Hyperfine Interaction; Isomer Shift

Isomer shift (IS) is caused by electrostatic Coulomb interaction between the nuclear charge distributed over a finite volume and the electrons in it (i.e. dominantly CS-electrons when neglecting relativistic effects). It gives information about the electronic charge density at the Mössbauer atoms such as: oxidation state, electronegativity of ligand character of bonds and spin state (high spin, low spin or intermediate).

In typical Mössbauer measurements the source and absorber materials are different, the electron densities are not equal ($|\rho_s(0)_E| \neq |\rho_s(0)_A|$) resulting in different Coulomb interaction in the source and absorber. In addition nuclear radii of the ground and excited states are different ($R_e \neq R_g$). The small changes in the electronic charge density at the Mössbauer atom yields a small shift in the nuclear energy levels of the source and absorber. The energy difference between E_S and E_A in the source and absorber due to the different electrostatic Coulomb interactions is given by the isomer shift δ

$$\delta = \frac{2}{3}\pi Z e^2 \{|\rho_s(0)_E| - |\rho_s(0)_A|\}\{\langle R_e^2\rangle - \langle R_g^2\rangle\} \tag{3.1}$$

where Z is the atomic number, $|\rho_s(0)_E|$ and $|\rho_s(0)_A|$ are the electron densities at the emitting and absorbing atom, $\langle R_e^2\rangle$ and $\langle R_g^2\rangle$ are the mean square radii of the ground and excited nuclear states. Any change in the s electron environment between the source and absorber gives rise a shift in the resonance absorption lines. For more details of this hyperfine interaction refer to the book by Gütlich et al. [2011].

The isomer shift depends on the s electron density influenced by shielding effects of p, d and f electrons. For example, Fe^{2+} and Fe^{3+} have electron configurations of ($3d^6$) and ($3d^5$), respectively. The ferrous ions have less s electron density at the nucleus due to the greater screening of the d electrons resulting in an isomer shift that is greater in ferrous iron than in ferric. Hence the most valuable information taken from isomer shift analyses is related

to the valence state of the Mössbauer atom embedded in a solid material.
In fact, the *measured* shift of the center of gravity of a Mössbauer spectrum, center shift (CS) is composed of two terms;

$$\mathrm{CS} = \delta + \delta_{SOD} \tag{3.2}$$

The first term is the chemical isomer shift δ (as defined above) which is usually temperature-independent (exception e.g. valency change with temperature change or charge hopping). The second term is varying with temperature. It is the second order Doppler shift δ_{SOD} which is a relativistic effect. δ_{SOD} is proportional to the mean square velocity $\langle v^2 \rangle$ of lattice vibration in direction of the γ ray propagation.

$$\delta_{SOD} = -\frac{\langle v^2 \rangle}{2c} \tag{3.3}$$

With increasing temperature $\langle v^2 \rangle$ increases and consequently, the center shift decreases. It is quite common in Mössbauer spectroscopy that ”center shift” and ”isomer shift” are used synonymously, though not correct.
In this work, we report the temperature and Cu concentration dependence of the center shift which may give an answer to the long-standing problems of valence state and electronic configurations which are still under debate. We try to give a systematic description of the electronic configuration of Fe in $\mathrm{Fe}_{1-x}\mathrm{Cu}_x\mathrm{Cr}_2\mathrm{S}_4$ compounds with $(0 < x < 1)$ by means of Mössbauer spectroscopy.
The investigation of the center shift and thus the isomer shift of Fe in $\mathrm{Fe}_{1-x}\mathrm{Cu}_x\mathrm{Cr}_2\mathrm{S}_4$ has the aim to answer the following issues:

- the distribution of iron valencies as a function of Cu doping. Earlier Mössbauer spectra show that Cu substitution leads to formation of Fe^{+3} instead of Fe^{2+} in the undoped compound. The value of isomer shift indicating the oxidation state of Fe will be traced systematically;

- from change in isomer shift we want to trace an eventual formation of intermediate valency and its dynamics (proposed by Fritsch et al. [2003], Palmer and Greaves [1999]).

3.2.2

Nuclear Electric Quadrupole Hyperfine Interaction

Investigating the nuclear quadrupole interactions by means of the Mössbauer spectroscopy, enables us to determine the magnitude, sign and the asymmetry of the electric quadrupole coupling. The electrostatic interaction between the electric quadrupole moment of the nucleus (eQ) and the electric field gradient (EFG) at the nucleus is called electric quadrupole hyperfine interaction which splits nuclear spin levels with $I \geqslant 1$. This interaction occurs, if at least one of the nuclear states has a non-zero quadrupole moment and senses a non-zero electric field gradient (Goldanskii and Herber [1968]).

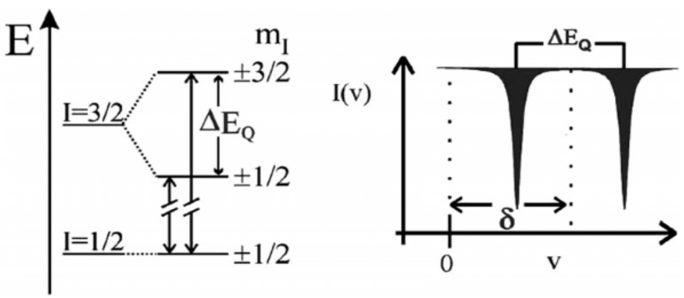

Figure 3.2: Excited state of the ^{57}Fe nucleus is split, thus two nuclear transitions from the ground state to the excited states rather than just one occur resulting in two corresponding peaks in the Mössbauer spectrum. The energy difference between the two peaks describes the energy difference between the two excited states, i.e. the quadrupole splitting (adopted from Gütlich [2012]).

The EFG at the Mössbauer nucleus is non-zero in a non-cubic valence electron distribution i.e. in non-cubic lattice site symmetry. The quadrupole Hamiltonian operator of the interaction is described by

$$\hat{\mathbf{H}}_Q = \frac{eQV_{zz}}{4I(2I-1)}\left[3\hat{\mathbf{I}}_z^2 - I(I+1) + \frac{\eta}{2}(\hat{\mathbf{I}}_+^2 + \hat{\mathbf{I}}_-^2)\right] \tag{3.4}$$

where the V_{ij} tensor consists of the second derivatives of electric potential, which represent the EFG tensor. In the principle axis system, the EFG tensor can be reduced to two independent parameters, $V_{zz}(= eq)$ and the asymmetry parameter $\eta = (\frac{V_{xx}-V_{yy}}{V_{zz}})$; $0 \leq \eta \leq 1$ with $|V_{zz}| \geq |V_{xx}| \geq |V_{yy}|$. One can derive the eigenvalues by diagonalization of the quadrupole Hamiltonian. From these equations we can derive the energy splitting etc. The eigenvalues indicate that the energy level for $I = 3/2$ splits into doubly degenerated sub-levels denoted by the magnetic quantum number m_I (see Fig. 3.2). For more details about the theory and origin of the EFG and nuclear moment refer to the book by Gütlich et al. [2011].

In our case, ^{57}Fe, the energy difference between the two split sub-levels with $m_I = \pm 3/2$ and $m_I = \pm 1/2$ (because of only the excited state splitting) is called the quadrupole splitting defined by

$$\Delta E_q = E_q(\pm\frac{3}{2}) - E_q(\pm\frac{1}{2}) = \frac{eQV_{zz}}{2}(1 + \frac{\eta^2}{3})^{\frac{1}{2}} \tag{3.5}$$

The Mössbauer spectrum is a simple doublet resulting from two allowed magnetic dipole transitions for γ radiation between the states of $I = 3/2$ and $1/2$ (see Fig. 3.2). The electric quadrupole splitting can give some information finally about the local symmetry but also on the oxidation and spin state.

In this thesis we investigate the influence of Cu doping in $FeCr_2S_4$ to answer some questions as are listed below:

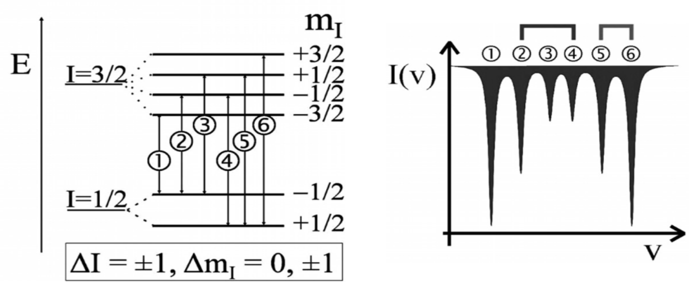

Figure 3.3: In the case of ^{57}Fe the excited state ($I = 3/2$) is split into four sub-levels and the ground state ($I = 1/2$) is split into two sub-levels resulting in a peak sextet in the Mössbauer spectrum (taken from Gütlich [2012]).

- earlier Mössbauer data revealed an unexpected appearance of an EFG in the magnetically ordered state. The origin is under debate;
- in this context the role of the Jahn-Teller effect as observed by many authors for undoped $FeCr_2S_4$ should be clarified. We will systematically study the influence of the substitution Cu on the Jahn-Teller effect.;
- we want to give a more detailed description of the orbital ground state and orbital ordering, respective orbital glassy behavior.

3.2.3

Magnetic Dipole Hyperfine Interaction

The magnetic hyperfine interaction is the interaction between the nuclear magnetic moment ($\boldsymbol{\mu}$) and the induced magnetic field of the electrons at the nucleus (see Fig. 3.3). The magnetic dipole interaction can be described by the following Hamiltonian

$$\hat{\mathbf{H}}_M = -\boldsymbol{\mu}.\boldsymbol{B_{hf}} = -g_N \mu_N \boldsymbol{I}.\boldsymbol{B_{hf}} \tag{3.6}$$

where $\boldsymbol{B_{hf}}$ is the effective field acting at the nucleus, g_N the nuclear g factor, μ_N the nuclear magneton, $\boldsymbol{I}$ the nuclear spin. In the case of ^{57}Fe atoms, B_{hf} is related to the magnetic properties of the partially filled $3d$ shells. The magnetic dipole interaction is also known as nuclear Zeeman effect which splits the ground state ($I = 1/2$) into two sub-states and excited state ($I = 3/2$) into four sub-states with the following energy shifts

$$E_m = -g_N \mu_N B_{hf} m_I \tag{3.7}$$

Fig. 3.3 shows the six allowed transition due to the splitting of the nuclear states and considering the selection rule $\Delta m_I = 0, \pm 1$ (magnetic dipole transitions) leading to a symmetric spectrum with six lines (sextet) in magnetically ordered materials. Information on the type of magnetism, the onset of magnetic ordering, the magnetic structure and the magnetization can be obtained by investigating of magnetic dipole hyperfine interaction. The average of hyperfine field is zero in paramagnetic materials due to the rapid fluctuations of the atomic moments and consequently an un-split line in the Mössbauer spectrum.

3.2.4

Combined Magnetic and Quadrupole Interactions

It is very common that a nuclear state is perturbed simultaneously by all three interactions (isomer shift, electric quadrupole, and magnetic dipole hyperfine interactions). Dealing with the monopole hyperfine interaction is easy, because it only shifts uniformly all resonance lines with no changes in their relative separations with by an additive isomer shift to all transition lines. The case will be different considering both electric quadrupole interaction ($\hat{\mathbf{H}}_Q$) and magnetic dipole interaction ($\hat{\mathbf{H}}_M$). They both depend on the magnetic quantum number of the nuclear spin, which means the interpretation of the spectrum gets much more difficult when evaluating their combined Hamiltonian which can be written;

$$\hat{\mathbf{H}} = \hat{\mathbf{H}}_M + \hat{\mathbf{H}}_Q \tag{3.8}$$

where

$$\hat{\mathbf{H}}_M = -g\mu_N B_{hf}(\hat{\mathbf{I}}_z \cos\theta + \hat{\mathbf{I}}_x \sin\theta\cos\phi + \hat{\mathbf{I}}_y \sin\theta\sin\phi) \tag{3.9}$$

$$\hat{\mathbf{H}}_Q = \frac{eQV_{zz}}{4I(2I-1)}\left[3\hat{\mathbf{I}}_z^2 - I(I+1) + \frac{\eta}{2}(\hat{\mathbf{I}}_+^2 + \hat{\mathbf{I}}_-^2)\right] \tag{3.10}$$

the polar and azimuthal angles θ and ϕ refer to the relative orientation of B_{hf} with respect to the EFG (Hoy [1967], Kündig [1967]).

The ground state ($I = 1/2$) of ^{57}Fe has no quadrupole moment resulting in no competing hyperfine interactions. But for the excited state ($I = 3/2$) there must be considered the contributions from both hyperfine interactions, magnetic dipole and electric quadrupole. If one of the two contributing hyperfine interaction is weak, it can be treated as a perturbation and help to simplify the solution of the Hamiltonian, such as the cases for the high-field condition ($g_N\mu_N B_{hf} \gg eQV_{zz}/2$) which is the most abundant case, and also the low-field condition ($eQV_{zz}/2 \gg g_N\mu_N B_{hf}$. But if these two contributing hyperfine interactions are of the same order of magnitude, $g_N\mu_N B_{hf} \approx eQV_{zz}/2$ with non-collinear principal axes, the mixed interaction would be more complex and there are no solutions in closed form for this Hamiltonian.

Kündig [1967] described a numerical method to find the solution of the problem for powder samples and fixed orientation between the EFG and B_{hf}. A similar approach was introduced earlier by Gabriel and Ruby [1965], which also treated the calculation of more complex Mössbauer spectra with the EFG randomly oriented in an external field. Also Häggström [1974] introduced a complicated analytical solution of the combined Hamiltonian which was improved later by Hasselbach and Spiering [1980]. With this refinement a more faster and precise calculation was achieved by using the new method for spherical angular averages.

Then again, for the least square fitting of measured spectra, this solution is still time consuming and inconvenient.
All mentioned methods suggest a numerical way to solve the secular equation of the nuclear excited state Hamiltonian in order to obtain the eigenvectors and eigenvalues via the transition matrix (solving for ground state is quite simple). Note that in the general case of non-collinear hyperfine interaction of comparable strength, a Mössbauer spectrum will consist of 8 lines where positions are determined by the eigenvalues of the hyperfine Hamiltonian. For a proper calculation of the intensities of the lines, it is necessary to use the eigenvectors of the excited and ground nuclear states connected by $M1$ dipolar γ-radiation. Here, in this thesis the Mössbauer spectra have been evaluated by the "Recoil", Mössbauer Spectral Analysis Software. The code and documentation have been performed by Lagarec and Rancourt [1998] considering various models relevant to different kind of sample properties. As outlined above, the combined Hamiltonian could be evaluated by a model named "Full Static Hamiltonian Site Analysis" in this software which is based on Blaes et al. [1985].
What we expect to see in our analyses:

- onset and development of magnetic order with temperature;
- its eventual dependency on valence state;
- can we find a variation of B_{hf} related to Jahn-Teller effect?
- can we determine the orientation between B_{hf} and EFG and possible variation with temperature?

3.3

Muon Spin Relaxation and Rotation

The acronym *μSR* denotes *Muon Spin Rotation, Relaxation or Resonance.* The μSR technique is an experimental method that can probe deep inside materials by using a short-lived subatomic particle, *a muon*, whose spin and charge are sensitive to local magnetic and electronic properties. Among other experimental methods such as NMR, EPR and Mössbauer spectroscopy, which all are using a magnetic moment as a probe to study matter, the role of μSR is important by its high sensitivity to magnetism and its time window for dynamical processes. This is sufficiently wide for studies of fast itinerant electron spin fluctuations down to slow, distributed spin relaxation in spin glasses, or for fast muon hopping down to slow diffusional processes and also is sufficiently sensitive for very small magnetic moments to be detected.

Table 3.1: Muon properties

Mass	m_μ	105.658 MeVc^{-2} $\approx 207m_e \approx 0.112m_p$
Charge	$\pm e$	interstitial position (generally), local probe
Spin	$\lvert\mathbf{S}_\mu\rvert$	1/2
Magnetic moment	μ_μ	$3.18\mu_p$
Gyromagnetic ratio	γ_μ	$2\pi \times 135.5$ MHzT^{-1}
Lifetime	τ_μ	$2.19714\ \mu s$

In 1936, the muon was discovered by Anderson and Neddermeyer [1936] as secondary radiation from cosmic rays. Table 3.1 shows properties of polarized (positive) muons. The discovery of muon has actually a complicated story and by following the discovery of radioactivity in 1899, one can say that the muon slowly emerged over almost a half-century (Blundell [1999]). There are two types of the muons in nature, i.e. positively and negatively charged, which are obtained from the following decays from pions (π)

$$\pi^+ \rightarrow \mu^+ + \nu_\mu \tag{3.11}$$

$$\pi^- \rightarrow \mu^- + \bar{\nu}_\mu \tag{3.12}$$

In condensed matter physics, the positive muon μ^+ is mainly used (ν_μ denoted the corresponding muon neutrinos). Because the μ^+ usually sits at an interstitial lattice site and thus well away from an atomic nucleus it is much more sensitive to the phenomena of interest to condensed matter physics (such as magnetism, superconductivity, frustration, etc.) than μ^- that is positioned close to nuclei and therefore during its lifetime τ_μ loses a significant amount of spin polarization.

Muons provided by cosmic rays do not have enough intensities to be used in experiments. For having higher intensity muons requires a particle accelerator. Typically high energy proton beams are fired into a target. Then pions (π^+) are produced via

$$p + p \rightarrow \pi^+ + p + n \tag{3.13}$$

The pions will decay into muons (eq. 3.11). The parity violation in the decay of pion allows the production of 100% spin polarized muons which is commonly used for producing muon beams for condensed matter physics research. For more information about the parity violation and basics of muon beam production see, e.g. Morenzoni [2017] or Blundell [1999]. The muon beam is guided from the production target to the sample to be studied down an evacuated beampipe by a series of electromagnetic devices. The muons are stopped in the sample and decay after a time t with probability proportional to $\exp(\frac{-t}{\tau_\mu})$ with $\tau_\mu = 2.197\mu s$ (Conversi et al. [1947]). The muon decay is a three body process

$$\mu^+ \longrightarrow e^+ + \nu_e + \bar{\nu}_\mu \tag{3.14}$$

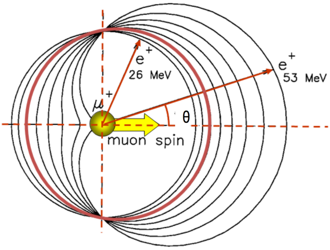

Figure 3.4: Angular distribution of the positron from the muon decay; The anisotropy of the distribution 100% for the highest positron energy, $E_{max} = 52.83$MeV and zero (isotropic distribution) for $E_{e^+} = E_{max}/2$. For the energy smaller than E_{e^+}, the asymmetry is negative. The red curve is the integration over all possible energies, $a = 1/3$ (taken from Morenzoni [2017])

creating a positron, an electron-neutrino and a muon-antineutrino. Like π-decay , the μ^+-decay is a weak nuclear interaction and consequently violates parity (Garwin et al. [1957]). The parity violation leads to a preferential emission of positrons along the muon spin direction upon decay.

In equation 3.14 the positron is the only particle which can be detected directly. Yet the positron need not be emitted exactly along the muon spin direction; there is an angular distribution of the emitted positrons from μ-decay given by

$$W(E, \theta) = 1 + a(E)cos(\theta) \tag{3.15}$$

where $a(E)$ is an energy dependent asymmetry parameter, and θ is the angle between muon spin and emitted positron path (see Fig. 3.4). The time evolution of the muon spin can be monitored e.g. by scintillation detectors which are set up around the sample to count the outgoing positron emission as a function of time and angle. The simplest experimental setup involves only two forward (F) and backward (B) detectors with respect to the initial muon spin direction which are generally arranged in opposing pairs, 180° to each other, see Fig. 3.5.

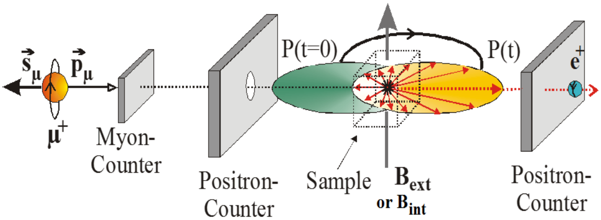

Figure 3.5: Schematic of a simple μSR setup with the muons implanted in a sample and experiencing a local field perpendicular to their direction. The sample is positioned between the forward and backward detectors (taken from Morenzoni [2017]).

For each detector, a histogram of detected positrons is kept as a function of the time interval between muon implantation into the sample and its decay. This process is recorded several million times and data are collected for further analysis. The positron count rate in a single detector has the form

$$N(t) = N_0 \exp\left(\frac{-t}{\tau_\mu}\right)(1 + a_0 P(t)) \tag{3.16}$$

where $N(t)$ is the time dependent count rate; N_0 is the initial count rate at time zero; and $P(t)$ is the polarization function describing the evolution of the muon spin polarization over time and gives the information on the local magnetic field and its distribution at the muon site (see below). The experimental quantity of interest is the positron asymmetry which is the difference in count rate between the F and B detectors monitored as a function of time divided by the total count rate for normalization

$$A(t) = \frac{N_F - \alpha N_B}{N_F + \alpha N_B} \tag{3.17}$$

α is an empirical constant to take into account in-equivalencies between the forward and backward detectors. These can result from efficiency differences in the detectors and electronics, asymmetric sample positioning, difference in solid angle coverage of the detectors, and so on. $A(t)$ is directly proportional to $P(t)$ meaning that the measured quantity $A(t)$ gives us access to the information of local magnetic structure of the studied material. In an ideal equipment, the initial asymmetry, when all spin of muons are polarized towards the forward detector, would be $A(t = 0) = a(E) = 1/3$, which is the energy integrated value of $a(E)$ from eq. 3.17. However, a typical initial asymmetry is reduced by various factors (such as, cryostat or detector wrapping, the exclusion of low energy positron which stop in the sample, effect of magnetic field on the positron trajectories, and etc.) and is around $A(t = 0) = 0.25$ (King et al. [2003]).

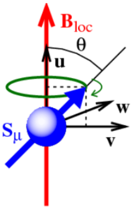

Figure 3.6: Semi-classical picture of muon spin, $\mathbf{S}_\mu$, precessing around the local field $\mathbf{B}_{loc}$ (adopted from Dalmas de Reotier [2010]).

μSR spectra are typically fitted in the time domain and the fitting function used is known as a *relaxation function*. The sensitivity of the muon to magnetism comes from its relatively large magnetic moment of $3.18\mu_p$. In a locally acting magnetic field $\mathbf{B}$ and its spin rotates around $\mathbf{B}$ with the Larmor frequency. The evolution of the muon spin is given by the Larmor equation (precession). The time derivative of angular momentum is equal to the sum of the torques;

$$\frac{d\hbar\mathbf{S}_\mu(t)}{dt} = \mathbf{m}_\mu(t) \times \mathbf{B}_{loc}(t) \tag{3.18}$$

since

$$\mathbf{m}_\mu = \gamma_\mu \hbar \mathbf{S}_\mu \tag{3.19}$$

and thus

$$\frac{d\mathbf{S}_\mu(t)}{dt} = \gamma_\mu \mathbf{S}_\mu(t) \times \mathbf{B}_{loc}(t) \tag{3.20}$$

Semi-classically, we can consider the Larmor precession as the spin of muon precessing at the end of a cone of half-angle θ which is the angle between the local field direction and muon spin direction (see Fig. 3.6). If we assume a static local magnetic field ($\mathbf{B}_{loc}(t) = \mathbf{B}_{loc}$) considering the denoted orientation in Fig. 3.6, we have

$$\mathbf{S}_\mu(t) = S_\mu^{\parallel}(0)\mathbf{u} + S_\mu^{\perp}(0)\left[\cos(\omega_\mu t)\mathbf{v} - \sin(\omega_\mu t)\mathbf{w}\right] \tag{3.21}$$

where the $\omega_\mu = \gamma_\mu B_{loc}$ is the Larmor frequency which only depends on the local magnetic field not on the angle θ between $\mathbf{S}_\mu$ and $\mathbf{B}_{loc}$. Then the projection of $\mathbf{S}_\mu(t)$ along $\mathbf{S}_\mu \equiv \mathbf{S}_\mu(t=0)$ reads

$$S_\mu^\alpha(t) = S_\mu\left[\cos^2\theta + \sin^2\theta\cos(\omega_\mu t)\right] \tag{3.22}$$

The polarization at later time in the α direction is defined by

$$P_\alpha(t) = \int \frac{S_\mu^\alpha(t)}{S_\mu} D_v(\mathbf{B}_{loc}) d\mathbf{B}_{loc} \tag{3.23}$$

$D_v(\mathbf{B}_{loc})$ is the static distribution function of the magnetic field $\mathbf{B}_{loc}$ at the muon site. When there is only one possible field value B_0, the field distribution can be defined by $D_v(\mathbf{B}_{loc}) = \delta(B_{loc} - B_0)$. In case of polycrystalline sample, the orientation of B_0 will be different from one crystallite to another according to the angle θ. Therefore the field distribution $D_v(\mathbf{B}_{loc})$ for a random orientation of these crystallites is given by

$$D_v(\mathbf{B}_{loc}) = \delta(B_{loc} - B_0)/(4\pi^2 B_0^2) \tag{3.24}$$

The integration of equation 3.23 leads to the relaxation function in the ordered phase

$$P_z(t) = \frac{1}{3} + \frac{2}{3}\cos(\omega_\mu t) \tag{3.25}$$

This means $\frac{1}{3}$ of orientations of the local field in the polycrystal are oriented parallel to the initial muon spin components (longitudinal term) and $\frac{2}{3}$ of the cases is aligned perpendicular to the initial muon spin direction causing Larmor precession (transverse term). Thus, the onset of magnetic order can be indicated by two effects: firstly, the presence of oscillations of $P_z(t)$ (and thus also of $A(t)$), and secondly the emergence of a $\frac{1}{3}$-tail, a baseline at high times.

For a single muon site, which is magnetically equivalent throughout the crystal, this results simply in a cosinusoidal oscillation in asymmetry $A(t)$. In more complex static fields, the resulting asymmetry function is somewhat like a cosine Fourier transform of the local fields at the muon sites, and an appropriate angular average has to be taken.

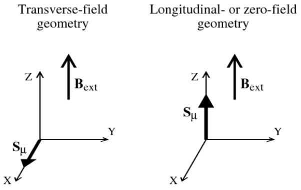

Figure 3.7: Axes definitions for the two geometries (adopted from Dalmas de Reotier [2010]).

In this thesis, the μSR spectra have been measured in zero applied field (ZF) and weak transverse field (TF). In general, when any magnetic field B_{ext} is applied parallel to the initial muon spin direction, the configuration is termed as the *longitudinal field* or *LF* configuration. The zero applied field or ZF configuration is the special case of no applied longitudinal field. The second configuration is the transverse field or TF configuration in which the field is applied perpendicular to the initial muon spin direction. Often the direction of applied field is taken as z-axis and the direction of polarization function is normally defined by the direction of the incoming muon beam or of the initial polarization $\mathbf{P}(0)$ which indicate the polarization direction $P_z(t)$ for *LF* and ZF configuration, and $P_x(t)$ for TF configuration (see Fig. 3.7).

Complex distributions of field may arise in case of modulated spin structures. E.g., incommensurate structures result in Bessel-shaped depolarization functions (see e.g. case of $FeCr_2S_4$, to be discussed later).

A prominent case is that of frozen electronic moments in a spin glass phase or static nuclear moments with relaxation times much larger than muon lifetime. The spectral response of an ideal spin glass is the so-called Kubo-Toyabe pattern. In this case, random local fields at the muon sites are distributed about a mean value of zero. For a concentrated system of randomly oriented static dipoles the probability distribution of internal local field is a Gaussian field distribution given by

$$D_v(\mathbf{B}_{loc}) = \left(\frac{1}{\sqrt{2\pi}\Delta_G}\right)^3 \exp\left(\frac{-B_{loc}^2}{2\Delta_G^2}\right) \tag{3.26}$$

The so- called static Gaussian Kubo-Toyabe function in zero external field (ZF) is

$$P_z(t) = P_{KT}(t) = \frac{1}{3} + \frac{2}{3}(1 - \gamma_\mu^2\Delta_G^2 t^2)\exp\left(\frac{-\gamma_\mu^2\Delta_G^2 t^2}{2}\right) \tag{3.27}$$

and in applied transverse field (TF);

$$P_x(t) = \exp\left(\frac{-\gamma_\mu^2\Delta_G^2 t^2}{2}\right)\cos(\omega_\mu t) \tag{3.28}$$

Here $\omega_\mu = \gamma_\mu B_{ext}$, the damping $\gamma_\mu^2\Delta_G^2$ represents the second moment of the field distribution along one direction perpendicular to the initial muon polarization (the field width). However, Gaussian field distributions are only appropriate for concentrated dipole moments. For dilute dipole moments the field distribution is better described by a Lorentzian function (Uemura et al. [1985]):

$$D_v(\mathbf{B}_{loc,i}) = \frac{\gamma_\mu}{\pi}\frac{a}{a^2 + \gamma_\mu^2 B_{loc,i}^2} \tag{3.29}$$

with $i = x$, y and z. a/γ_μ is a half-width at half maximum (HWHM) to describe the random local fields at muon sites. For the case of zero external field, taking a statistical average over the time dependent of the muon spin obtains the muon spin relaxation function, which derived by Kubo [1981] is

$$P_z(t) = \frac{1}{3} + \frac{2}{3}(1 - at)\exp(-at) \tag{3.30}$$

This is known as *static Lorentzian Kubo-Toyabe relaxation function.* Both Gaussian and Lorentzian Kubo-Toyabe functions will play a role, when the local field is static.

The effect of dynamic fluctuation of moments especially in the case of spin glass was considered by Uemura et al. [1985], who proposed a Gaussian distribution of the local field at each muon site. The muon spin relaxation function at each site was calculated by the strong collision approximation for the dynamic modulation of random field (Hayano et al. [1979]).

To get a dynamic relaxation function it has been assumed that the local field at μ^+ is suddenly changed by a collision, after which it is randomly distributed with no correlation to fields before collision. Collisions are taking place with a rate ν. This type of the dynamical process is a so-called 'Markovian' leading to an exponential decay of the auto-correlation function of fluctuating field:

$$\frac{\langle B(t)B(0)\rangle}{\langle (B(0)^2)\rangle} = \exp(\nu t) \tag{3.31}$$

The dynamic relaxation function can be defined as following:
$P_z(t,\nu)$ = muons that do not collide up to time t + muons that do one collision + muons that do two collision + ... = $\sum_{n=0}^{\infty} p_z^{(n)}(t)$
Then

$$P_z(t) = \\ \exp(\nu t)\left\{p_z(t) + \nu\int_0^t p_z(t_1)p_z(t-t_1)dt_1 + \nu^2\int_0^{t_1}\int_0^{t_2} p_z(t_1)p_z(t_2-t_1)p_z(t-t_2)dt_1dt_2 + ...\right\} \tag{3.32}$$

An analytic solutions can be found by Laplace transforms:

$$F_z(s) = \int_0^{\infty} P_z(t)e^{-st}dt = \frac{f_z(s+\nu)}{1-\nu f_z(s+\nu)} \tag{3.33}$$

where $f_z(s) = \int_0^{\infty} g_z(t)e^{-st}dt$. This dynamical Kubo-Toyabe function can be applied at any distribution of local field or collision rate.
The data analysis with this function is more cumbersome since non-analytical. This function will later play a rule while fitting our ZF μSR data.
μSR was used in our study of $Fe_{1-x}Cu_xCr_2S_4$ since it gives a complementary local view of magnetism to Mössbauer spectroscopy. While Mössbauer spectroscopy senses magnetism at Fe, μ^+ is a probe at an interstitial site. As with Mössbauer spectroscopy we will follow the dependence on Cu doping.
We will study:

- temperature dependence of spontaneous rotations, i.e. of fields acting at muon site;
- distribution of fields, eventual spin dynamics;
- eventual indication for changing spin structures, spin glassy behavior;
- eventual relation to Jahn-Teller effect or orbital order;
- eventual correlations of local field distribution/fluctuation with appearance of CMR.

Chapter 4

$\mathbf{Fe_{1-x}Cu_xCr_2S_4}$: What Is Known by Now - A Review

This chapter summarizes some known results of physical properties of $Fe_{1-x}Cu_xCr_2S_4$ which will explain why we reinvestigate this system more thoroughly. The aim is to clarify still open questions related to this complicated system by means of two local probe methods, Mössbauer spectroscopy and μSR in addition to standard characterization by XRD and magnetization.

4.1

Structural Properties of $\mathbf{Fe_{1-x}Cu_xCr_2S_4}$

The Cr based chalcogenide system $Fe_{1-x}Cu_xCr_2S_4$ has a normal spinel structure AB_2X_4 in which X represents the sulfur; B-sites (octahedral) are occupied by chromium and A-sites (tetrahedral) have a mixture of iron and copper depending on concentration x (Goodenough [1964]). The lattice constant is 9.997 ± 0.001 $\mathring{A}$ for $x = 0$ and varies with x following Vegard's low (e.g. Büttgen et al. [2004] and Tsurkan et al. [2005], see also section 5.1).

4.2

Magnetism in $\mathbf{Fe_{1-x}Cu_xCr_2S_4}$

$Fe_{1-x}Cu_xCr_2S_4$ are ferrimagnets for the whole substitution range except $x = 1$. $CuCr_2S_4$ is ferromagnetic (Haacke and Beegle [1967], Lotgering et al. [1969]).

Two superexchange interactions are predicted to be present in $Fe_{1-x}Cu_xCr_2S_4$. One is an antiferromagnetic intersublattice superexchange interactions between Fe(A)-Cr(B), the other an intrasublattice superexchange interaction between Cr(B)-Cr(B) that is ferromagnetic (Tsurkan et al. [2005]). This results in a ferrimagnet ground state. In Fig. 4.1 the magnetic ground state and the two superexchange interactions are illustrated.

Often also a superexchange between the Fe ions is mentioned to play a role but this should only be present in inverse spinels. Since $Fe_{1-x}Cu_xCr_2S_4$ has a normal spinel structure, where Fe only occupies the A site, such an interaction is not possible. In the 90° Cr^{3+}-anion-Cr^{3+} interaction, the half-filled π-bonding t orbital shares a common anion p orbital with an empty σ-bonding e orbital on the neighboring cation. According to Kanamori [1959], this results in a ferromagnetic spin interaction. In case of the 123.2° Fe^{2+}-anion-Cr^{3+} interaction (not shown here), the prediction of the resulting spin interaction is difficult due to the changing symmetry and not vanishing orbital moment of the Fe^{2+} ion. But experimental results prove antiferromagnetic interactions (Haacke and Beegle [1967], Lotgering et al. [1969]).

The assumption of superexchange interactions to be responsible for the magnetism in $Fe_{1-x}Cu_xCr_2S_4$ is supported by Tsurkan et al. [2005]. Here it is pointed out that the varia-

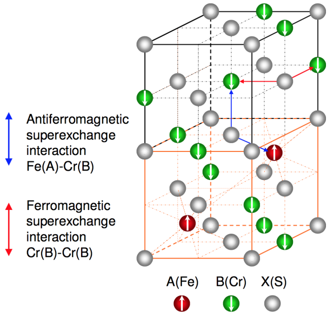

Figure 4.1: Illustration of two superexchange interactions in $Fe_{1-x}Cu_xCr_2S_4$. One is an antiferromagnetic interaction between Fe(A)-Cr(B), the other a ferromagnetic interaction between Cr(B)-Cr(B). Here only the main part of the unit cell is shown. The spin direction is indicated by white arrows (figure adopted from Taubitz [2010]).

tion of the basic magnetic parameters such as the increasing of Curie temperature T_c and decreasing of lattice constant a_0 for the whole substitution range (except $x = 1$) indicate the superexchange to be the dominant magnetic exchange mechanism in $Fe_{1-x}Cu_xCr_2S_4$ resulting in ferrimagnetic order.

On the other hand, to describe the magnetoresistance in $Fe_{1-x}Cu_xCr_2S_4$, one can suppose the double exchange interactions mechanism to be the same as in manganese perovskites. As mentioned already, the Mn ions in perovskites exchange interactions occur at the same site between Mn^{4+} and Mn^{5+}. But unlike the perovskites, the double exchange cannot be applied for spinel because the magnetic ions in spinel occupy two different sites, tetrahedral and octahedral site.

Palmer and Greaves [1999] proposed the so-called triple-exchange for this problem considering a mixed iron valence state. A ionic band-structure picture of the triple-exchange reproduced by Fritsch et al. [2003] which will be discussed later. The electron hopping in triple-exchange for $Fe_{1-x}Cu_xCr_2S_4$ occurs between three metallic ions; Fe^{2+}, Cr^{3+} and Fe^{3+} via a non-metallic ligand (Taubitz et al. [2009]).

However, in chalcogenide spinel systems additional more distant neighbor interactions can be present and compete with the superexchange interactions. This leads to frustration effects and spin canting (which is an ingredient of spin-glass state).

Frustration is originated from competing interactions between nearest and next nearest exchange couplings (Fritsch et al. [2004], Roth [1964]). The A ions form a diamond sublattice (two fcc lattices at $(0, 0, 0)$ and $(1/4, 1/4, 1/4)$) coupled antiferromagnetically by the magnetic superexchange interactions. Büttgen et al. [2004] explained the frustration in AB_2X_4 spinel: "An illustration of the A site and its exchange paths is given in Fig. 4.2. Considering the entire lattice, the exchange between the two A site sublattices is transferred as follows: the four nearest neighbors (NN) are connected via six A-X-B-X-A exchange paths (J) including nearly rectangular X-B-X bonds. The 12 next-next-nearest neighbors (NNN) are connected via two equivalent A-X-B-X-A exchange paths (J), including again nearly rectangular X – B – X bonds of non-magnetic ions. The 12 next-next-neighbors ($NNNN$) are coupled via one A-X-B-X-A exchange paths (J''), including a 180° X-B-X bond. Note that the NNN in the entire lattice corresponds to the nearest neighbors within each fcc sublattice. We conclude that each fcc sublattice is coupled antiferromagnetically and, hence, is frustrated. In addition, the two sublattices are coupled again antiferromagnetically, strongly enforcing the frustration effect".

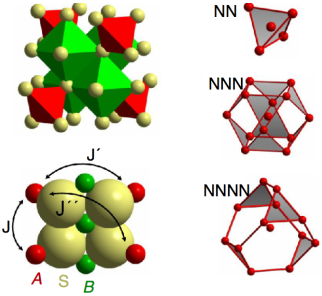

Figure 4.2: Three different types of A-S-B-S-A interaction paths (J, J', J'') via A sites (adopted from Büttgen et al. [2004]).

It was also mentioned that the ferromagnetic ground state of $CuCr_2S_4 (x = 1)$ could not be explained by the existing interaction models. As a possible explanation the interaction of conduction electrons and local magnetic moments supporting ferromagnetism was mentioned e.g. by Fritsch et al. [2003], Haacke and Beegle [1967], Tsurkan et al. [2010].
In order to understand further features of the orbital physics and magnetic properties in $Fe_{1-x}Cu_xCr_2S_4$, we first give a general summery of what is known about undoped $FeCr_2S_4$. Then in separate sections, a short history of using Mössbauer spectroscopy and μSR on $Fe_{1-x}Cu_xCr_2S_4$ and some other related measurements to our work will be given.
The ferrimagnetic normal spinel $FeCr_2S_4$ has been studied in a large number of crystallographic, magnetic, and electric investigations since 1956 by Lotgering. These investigations have shown that the Cr^{3+} sublattice with an electronic configuration of $3d^3$ and S = 3/2 is dominated by ferromagnetic exchange via the 90° Cr-S-Cr bonds. For the A site, the $3d^6$ electrons are Hund's rule coupled revealing a high spin configuration with $S = 2$. The A site ions are only weakly antiferromagnetically coupled within sublattice, but much stronger to the B site chromium ions and ferrimagnetic order is established below $T_c = 167$ K with the Fe^{2+} and Cr^{3+} magnetic moments aligned anti-parallel to each other (Shirane et al. [1964], Tsurkan et al. [2010]).

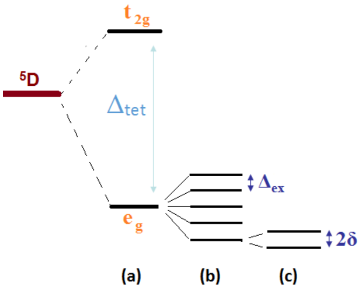

Figure 4.3: Electronic level structure of tetrahedrally coordinated Fe^{2+}.(a) The cubic crystal field at the tetrahedral site splits the ^5D free-ion ground state into a lower doublet and and an excited orbital triplet. (b) At $T < T_c$, the spin degeneracy is removed by the exchange field, which splits the ^5e_g into five e_g orbital doublets. (c) Spin-spin interaction and second order spin-orbit represent a final perturbation which splits the lowest e_g doublet to two component by 2δ. then the mean value of the principal component of electric-field gradient (EFG) does not vanish and the thermal average of that leads one to observe a quadrupole interaction in the presence of hyperfine magnetic field. The EFG is therefore induced by magnetic order (Eibschütz et al. [1967], Feiner [1982]).

An anomaly in the low-field magnetization data at T ~ 60 K is ascribed to a change in the magnetic configuration (Maurer et al. [2003], Mertinat et al. [2005], Shen et al. [2009], Tsurkan et al. [2001a,b, 2010]). This has recently been attributed to the formation of a non-collinear (possibly helical) spin configuration with an incommensurate modulation involving three different Fe sites as indicated by μSR and Mössbauer spectroscopy (Engelke et al. [2011], Kalvius et al. [2010]). The same temperature has also been associated with the onset of short-range orbital order and dynamic Jahn-Teller distortion, suggesting a mutual influence of spin configuration and orbital correlation (Tsurkan et al. [2010]).

Below T ~ 60 K, the orbital moment of Cr^{3+} ions in octahedral symmetry is quenched due to half-filled $F_{t_{2g}}$ ground state until an orbital ordering occurs at $T_{oo} = 8 \sim 10$ K, which however, arises from the orbital ground state of the Fe ions ($Fe^{2+}: 3d^6, S = 2$) with unfilled e_g state rather than Cr^{3+} ions (Fichtl et al. [2005]). As seen in Fig. 4.3 and as discussed by Feiner [1982] for Fe^{2+} ions, the five-fold degenerate ground state is split by the crystal field into a lower orbital doublet and an excited triplet. In the magnetically ordered state, the exchange field further splits the spin degeneracy of the e doublet into $2S + 1 = 5$, which can be split by spin-orbit coupling or an additional low symmetry crystal field component originating from Jahn-Teller effect.

This transition has been also observed in Mössbauer spectroscopy and heat capacity measurements by Lotgering et al. [1975] that indicated a λ anomaly in the specific heat at low temperature(13 K) accompanied by a strong change in the character of Mössbauer spectra. Spender and Morrish [1972] proposed a static to dynamic Jahn-Teller transition.

4.3

Mössbauer Spectroscopy

Here, we report Mössbauer studies on $FeCr_2S_4$ and refer to the data performed in our group by Engelke et al. [2011] on the same sample used by Tsurkan et al. [2010] and Kalvius et al. [2010]. For other concentrations ($x \neq 0$), most research has been done related to the valence state and also to the mechanism behind the CMR as reported also in the following.

Already, early Mössbauer studies on the $FeCr_2S_4$ report a surprising non-zero quadrupole splitting of the hyperfine pattern indicating substantial deviations from cubic symmetry at the tetrahedral A-sites (Eibschütz et al. [1967], Hoy [1967], Hoy and Singh [1968], Spender and Morrish [1972]). This is in contradiction with the neutron powder diffraction data at 4.2 K reported by Shirane et al. [1964] . The reported data show that the compound remains cubic down to low temperatures, the spin arrangement is of a simple collinear ferrimagnetic type, and observed magnetic intensities are in good accordance with $\mu_{Cr} = 2.9\mu_B$ and $\mu_{Fe} = 4.2\mu_B$. There is therefore no direct crystallographic reason for an electric field gradient at the Fe nucleus.

In this context, Eibschütz et al. [1967] interpreted their Mössbauer spectra assuming an electric-field gradient (EFG) induced by the magnetic order (using the molecular field approximation). They supposed that the magnetic ordering of the spins will remove the orbital degeneracy of ^5E_g via the spin-orbit coupling below the Curie point T_c (see Fig. 4.3) causing the appearance of an electric field gradient (thus no EFG above T_c). The major component of the EFG tensor V_{zz} induced by magnetic order is positive, axial and the principle axis of the electric-field gradient is parallel to the easy axis of magnetization directed along [100]. These results have been confirmed by Hoy and Singh [1968]. They concluded that apart from the magnetically induced contribution there must be a temperature dependent lattice distortion, which results in an EFG that is larger than expected. In order to investigate the low temperature transition in $FeCr_2S_4$, Spender and Morrish [1972] presented also Mössbauer measurements at temperatures below 20 K. They also concluded a deviation from cubic symmetry at the tetrahedral Fe^{2+} sites due to nonzero quadrupole splitting and distinct changes in Mössbauer spectra below T = 10 K. For T > 10 K, the variation of the hyperfine magnetic field and EFG agree with Eibschütz's results. For T < 10 K, the EFG becomes negative and the asymmetry parameter η is nonzero which is attributed to the static distortion of the Fe^{2+} sites due to a Jahn-Teller distortion.

A very detailed analysis of Mössbauer spectra was given by Brossard et al. [1979], who proposed that the observed changes around 13 K are due to an orbital transition. They explained the situation above 13 K with orbital paramagnetism, where the e_g orbitals z^2 and $x^2 - y^2$ are equally populated. At lower temperatures the sixth 3d electron occupies the z^2 orbital at all sites, which they call ferromagnetic orbital ordering.

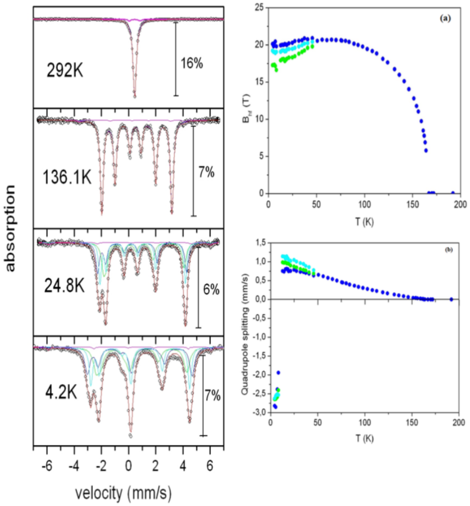

Figure 4.4: Temperature dependence of ^{57}Fe absorption spectra of $FeCr_2S_4$ characteristic for the different regimes (left). At 292 K above T_c, only a dominant single Lorentzian resonance indicated paramagnetic phase. At 136 K below T_c, a six line pattern typical for the collinear ferromagnetic structure in company with only a magnetically induced axial EFG. At 24 K the regime between 50 K and 20 K, three superimposed sextet with an axially symmetric EFG. Between 20 K and 10 K, starting of line broadening. Below 10 K, a clear rotation of EFG by $\theta = 90°$, $\varphi = 0°$and 45°, the major component of EFG (V_{zz}) becomes negative and doubles in value with symmetry lower than axial. Temperature dependence of hyperfine field and quadrupole interaction (right).(taken from Engelke et al. [2011])

Feiner [1982] has interpreted Mössbauer results using a mean field theory taking into account local vibronic dynamics and ascribed the phase transition around 10 K as a cooperative Jahn-Teller effect.

We will now concentrate on the most recent work done in by Engelke et al. [2011]. The Mössbauer data were recorded on the same sample material as used for muon spin rotation and also heat capacity in order to preclude any problems with varying sample quality. Preliminary reports were given in Kalvius et al. [2010]. Fig. 4.4 presents a series of absorption spectra for different temperature. Each spectrum in this figure is representative for a the different temperature regime.

Above T_c = 165 K a singlet is dominant which is accompanied by a less than 5% of spectral area impurity signal. This has been interpreted with a slight local deviation from stoichiometry as indicated already by Lotgering et al. [1975]. Engelke et al. [2011] compare their result above T_c with the results from muon spin rotation where partial long range order is found already above T_c. They observe no indication for this phase from their Fe hyperfine spectra and conclude this may be related to the Cr and not the Fe sublattice.

The spectra below T_c shown in Fig. 4.4, have 6-line patterns that are typical for the collinear ferromagnetic structure. A small quadrupole interaction due to an axially symmetric electric field gradient appears, which is increasing with increasing magnetic hyperfine field as given in Fig. 4.4a and 4.4b. This quadrupole interaction can be related to a magnetically induced electric field gradient as proposed by Eibschütz et al. [1967]. For fitting the spectra between about 50 K and 20 K three sets of hyperfine interactions had to be introduced shown in Fig. 4.4a. They interpret these non-equivalent sites below 50 K with the onset of short-range orbital ordering accompanied with a spin reorientation that is also concluded from μSR and X-ray data by Kalvius et al. [2010].

The lines become strongly broadened below 20 K as seen in Fig. 4.4. This is in parallel to a maximum in mean-square displacement observed in X-ray data (Tsurkan et al. [2010] (see later in Fig. 4.22)). It can be related to a dynamical JT distortion.

Finally, the quadrupole interaction has a dramatic change below 10 K due to a change of sign and a reorientation of the electric field gradient. It has been interpreted with the orbital ordering below 10 K which is in agreement with a peak in specific heat (Tsurkan et al. [2010] (see later in Fig. 4.23)).

We now turn to the doped compounds $Fe_{1-x}Cu_xCr_2S_4$. The investigations of the magnetic properties and valence state of the $Fe_{1-x}Cu_xCr_2S_4$ started by the studies of Goodenough [1967], Haacke and Nozik [1968], Lotgering et al. [1969].

Lotgering et al. [1969] proposed a strictly ionic model for $Fe_{1-x}Cu_xCr_2S_4$ from X-ray diffraction studies in which the iron in tetrahedral sites is divalent and trivalent for Cu concentrations $x < 0.5$. For $x \geq 0.5$ iron is trivalent. In this model Cu stays monovalent for whole range of doping while octahedral Cr is trivalent and tetravalent. Their Mössbauer data on $Fe_{0.5}Cu_{0.5}Cr_2S_4$ observed no quadrupole splitting, i.e. the symmetry of iron sites is cubic. Also the isomer shift is in the range of Fe^{3+} in agreement with their model.

Thus, in the so-called Lotgering model:

$$\begin{array}{lr}
\mathrm{Fe^{2+}}{}_{1-2x}\mathrm{Fe}_x^{3+}\mathrm{Cu}_x^{+}[\mathrm{Cr}_2^{3+}]\mathrm{S}_4^{2-} & 0 \leq x \leq 1/2 \\
\mathrm{Fe^{3+}}{}_{1-x}\mathrm{Cu}_x^{+}[\mathrm{Cr}_2^{3+}]\mathrm{S}_{5-2x}^{2-}\mathrm{S}_{2x-1}^{-} & 1/2 \leq x \leq (1+\delta_0)/2 \\
\mathrm{Fe^{3+}}{}_{1-x}\mathrm{Cu}_x^{+}[\mathrm{Cr}_{3-2x+\delta_0}^{3+}\mathrm{Cr}_{2x-1-\delta_0}^{4+}]\mathrm{S}_{4-\delta_0}^{2-}\mathrm{S}_{\delta_0}^{-} & (1+\delta_0)/2 \leq x \leq 1
\end{array}$$

Where S^- indicates a hole in the valence band and δ_0 an unknown parameter. The Lotgering model begins with the valence state $Fe^{2+}Cr_2^{3+}S_4^{2-}$ at $x = 0$. The valence state of iron ions are gradually changed to Fe^{3+} with increasing the monovalent Cu concentration, and finally for $x = 0.5$ is trivalent for all of iron ions. For $x > 0.5$, S ions are expected to possess holes in the 3p band (S^-) to achieve charge neutrality. And for very high copper concentrations, the Cr ions are postulated to get a valence state of 4+.

This model is in contrast to a proposal of Goodenough [1967] explaining metallic Cu and its ferromagnetism (Goodenough [1967]) by delocalized electrons for Cu^{2+} in tetrahedral sites and localized Cr^{3+} in octahedral sites, $Cu^{2+}Cr_2^{3+}S_4^{2-}$.

At the same time, Haacke and Nozik [1968] performed Mössbauer spectroscopy to realize which model is compatible for $Fe_{1-x}Cu_xCr_2S_4$ for six different copper concentrations which x

varies from zero to 0.7 at 77° K. Their interpretation supports the proposal by Lotgering for the valence state of the involved cations, but it is not a strictly ionic model. Their Mössbauer measurements indicated that the covalency increases with increasing of Cu substitution, which is in agreement with a covalent band description proposed by Goodenough [1967]. They found two composition regions below T_c; $0.0 < x < 0.5$ and $0.5 \leq x < 1.0$. Above T_c, the spectra for $x = 0.3$ and $x = 0.5$ (representative of both composition regions) do not show any hyperfine splitting and only one resonance peak is observed which is typical for the paramagnetic region. For $x \geq 0.5$ below T_c, the spectra splits into six lines with negligible quadrupole splitting and larger hyperfine field compared with $FeCr_2S_4$, and they conclude the existence of Fe^{3+} for $0.5 \leq x < 1.0$. They have also compared the isomer shifts for these two compound with the purely ionic Fe^{2+} and Fe^{3+}. The observed isomer shift was smaller than for purely ionic one indicating appreciable covalent effects and delocalization of Cu d-electrons. For $x < 0.5$ below T_c, the superposition of two magnetic hyperfine spectra have been suggested signifying the two site of Fe^{2+} and Fe^{3+}.
Later, Kim et al. [2004] and Klencsár et al. [2005] also reported Mössbauer studies of $Fe_{1-x}Cu_xCr_2S_4$ for different copper concentrations.

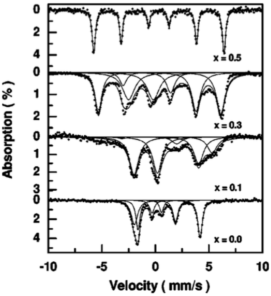

Figure 4.5: Magnetization curves of $Fe_{0.9}Cu_{0.1}Cr_2S_4$ as a function of temperature (left). Mössbauer spectra of $Fe_{1-x}Cu_xCr_2S_4$ for $x = 0.0, 0.1, 0.3$, and 0.5 at 13 K (right)(from Kim et al. [2004]).

Fig. 4.5 shows selected Mössbauer spectra from Kim et al. [2004] indicating Fe^{3+} for Cu doping $x = 0.3$ and $x = 0.5$ with nearly symmetrical sextet patterns (below T_c) and Fe^{2+} for concentration $x = 0.1$ with an asymmetrical line broadening interpreted as a sign for dynamic Jahn-Teller relaxation (no Fe^{3+} in low Cu concentration). For temperatures below 110 K they observe a decrease of magnetic hyperfine field (for $x = 0.1$). They connect it to an onset of orbital field contribution related to a metal-semiconductor transition around 110 K as found by Fritsch et al. [2003].

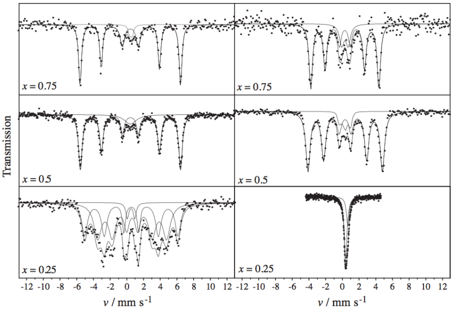

Figure 4.6: Mössbauer spectra of $Fe_{1-x}Cu_xCr_2S_4$ ($x = 0.25, 0.5, 0.75$) at 77 K (left) and at room temperature (right) (taken from Klencsár et al. [2005]).

Klencsár et al. [2005] also confirmed the Lotgering model that the Fe^{2+} and Fe^{3+} coexist in tetrahedral site for low copper concentration. They have also mentioned still a paramagnetic fraction to occur below T_c for all Cu concentrations. Their interpretation was that small superparamagnetic clusters of about 10 nm are formed. Fig. 4.6 shows this paramagnetic fraction in the center of all spectra.
Recently, Taubitz et al. [2009] reinvestigated the valence state of the constituent elements in $Fe^{2+}Cr_2^{3+}S_4^{2-}$ using XPS spectroscopy, resulting in monovalent Cu and trivalent Cr, and also Fe^{2+} and Fe^{3+} for $x < 0.5$ and $x \geq 0.5$, respectively.
In summery, the valence state of the $Fe_{1-x}Cu_xCr_2S_4$ was investigated by many authors using various methods. But results are controversial described within the mutually excluding models.

4.4

μSR

μSR studies on $Fe_{1-x}Cu_xCr_2S_4$ have been done only for the Cu concentrations $x = 0.0, 0.2, 0.5, 0.8$ between 5 and 300 K (Kalvius et al. [2008, 2010, 2013]). The following interpretation has been taken from these papers. It is obvious from their results that the idea of a simple collinear ferrimagnetic structure throughout the whole concentration range x and at all temperatures below T_c cannot be maintained, meaning that there is no simple relation between Cu substitution on the Fe site and the spin structure.

4.4.1

$FeCr_2S_4$

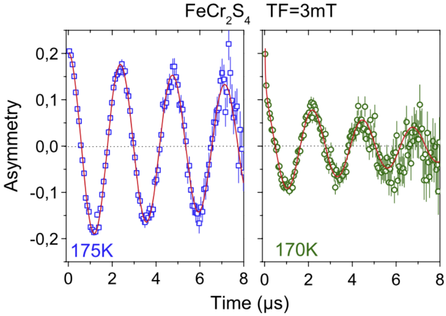

Figure 4.7: Transverse field spectra of $FeCr_2S_4$ above and near the magnetic ordering temperature. The solid lines are least squares fits to a single oscillatory signal (eq. 4.1) at 175 K and to two signals at 170 K (from Kalvius et al. [2010]).

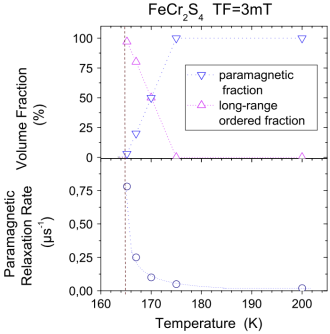

Figure 4.8: Temperature dependence of the volume fractions of paramagnetic and long range ordered states (top), and paramagnetic relaxation rate (bottom) (from Kalvius et al. [2010]).

The weak transverse field μSR measurements (TF) show that the transition between the ordered and the paramagnetic phases is broadened, extending about 10 K as illustrated in Fig. 4.7. The 175 K spectrum, i.e. above $T_c = 165$ K, is typical for a paramagnet whose spectral function is

$$G(t) = \exp(-\lambda_{par}t)\cos(2\pi\nu_\mu t) \tag{4.1}$$

λ_{par} and ν_μ are the relaxation rate and the Larmor precession frequency of the muon spin induced by the mean local field. The mean magnetic local field in paramagnetic phase is zero, and in *TF* measurement the muon spin process around the applied field (here 3 mT). At 170 K (i.e. above T$_c$) the spectra consist of two sub-spectra. In Fig. 4.8 the temperature dependence of the TF spectra above T$_c$ and their parameters are plotted. There is one oscillatory pattern related to the paramagnetic fraction and a second signal that is a rapidly relaxing reflecting the magnetically ordered fraction. The temperature dependence of the volume fraction shows the formation of an ordered fraction around 175 K and this fraction is growing up till 165 K where nearly all the sample volume has entered the ordered state. The sharply rising relaxation rate at approximately T$_c$ indicates a second-order phase transition.

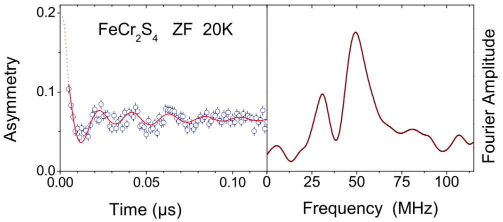

Figure 4.9: Zero-μSR spectrum of $FeCr_2S_4$ at 20 K (left). The solid line is the fit to a two-frequency Bessel oscillation pattern. Fast Fourier transform of this spectrum (right) (from Kalvius et al. [2013]).

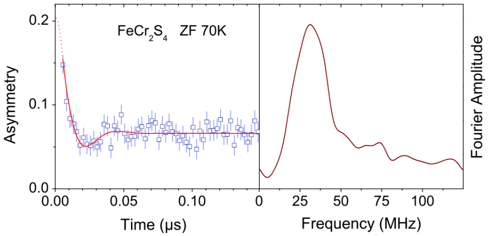

Figure 4.10: Zero-μSR spectrum of $FeCr_2S_4$ at 70 K (left). The solid line is the fit to a single-frequency cosine oscillation pattern. Fast Fourier transform of this spectrum (right) (from Kalvius et al. [2013]).

Kalvius et al. [2010] have carried out μSR between 5 and 200 K in zero applied field (ZF) together with Mössbauer measurements.

The ZF spectra show clear changes between spectra above 50 K and below. In case of a simple collinear ferrimagnetic spin structure, the usual ZF spectral function for a polycrystalline powder is eq. 4.2 which is compatible for spectra above 50 K;

$$G(t) = \frac{2}{3}\exp(-\lambda_{trans}t)\cos(2\pi\nu_\mu t) + \frac{1}{3}\exp(-\lambda_{long}t) \tag{4.2}$$

λ_{trans} and λ_{long} are the transverse and longitudinal relaxation rates, respectively. The spontaneous Larmor oscillations are damped with the rate λ_{trans} which gives information about static field distributions. λ_{long} has its source in a dynamics of the magnetic moments generated by the fluctuation rate of the interstitial field.

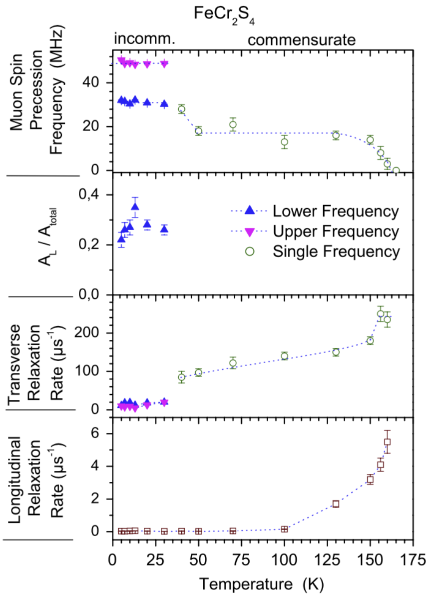

Figure 4.11: Temperature dependence of the spectral parameters of $FeCr_2S_4$ in the magnetically regime. The temperature dependence of muon spin precession frequency show single rotating signal from T_c down to about 50 K. Below ~ 50 *K* there are two frequencies indicating the change in spin structure. At 40 K the transverse relaxation rate increases suddenly and sharply which has been interpreted to a substantial spin disorder on a local scale in the magnetic structure above 40 K (from Kalvius et al. [2010]).

The ZF spectra above 50 K have been analyzed using eq. 4.2 with only one single-frequency cosine oscillation pattern (see fast Fourier transform (FFT) in Fig. 4.10), which is sign for the simple collinear ferrimagnet phases. The spectra below ~ 50 K have been fitted to a two-frequency Bessel oscillation pattern (see the FFT in Fig. 4.9). Bessel oscillations in a μSR spectrum appear in case of incommensurately modulated spin structure. The temperature dependence of the spectral parameters for $T < T_N$ have been shown in Fig. 4.11. In summary, their results give the essential news about the magnetic state below 50 K:

- the muon spin precession frequency splits into two frequencies at temperatures below ~ 50 K which is accompanied by a step-like decrease of the transverse relaxation rate;
- the ground state of $FeCr_2S_4$ cannot be a simple collinear ferrimagnet because in that case only one frequency would be expected;

- suggested is a probably incommensurately modulated helical spin structure as the magnetic ground state of $FeCr_2S_4$.

The initial asymmetry from ZF spectra is not the same as indicated in TF spectra. Apparently the very early part of the spectrum in the initial dead time of the spectrometer is lost due to the rapid initial decay of asymmetry caused by relatively high frequencies. This means part of the magnetic response can not be recorded. The massive increase of λ_{long} around the T_c is characteristic for dynamic short-range order . The coexistence of short-range order and paramagnetic phase around T_c over a range of few Kelvins is in contrast to results taken from Mössbauer spectra and magnetization data. The Mössbauer spectra and magnetization data show a quite well defined second-order transition at T_c. Kalvius et al. [2013] suggest that the special spin dynamics of the short-range order state in $FeCr_2S_4$ and the specific time window of the different used methods play a role.
Notably, there is not seen a clear signature in μSR for the transition to the orbital ordered state below about 10 K in contrast to the Mössbauer data.

4.4.2

$Fe_{0.8}Cu_{0.2}Cr_2S_4$

Kalvius et al. [2013] carried out ZF and TF μSR between 10 K and 245 K. The TF measurements confirm that there is only one muon stopping site in the crystal lattice. The ZF data in long range order can be least square fitted by a single cosine oscillation function which is given in eq. 4.2 indicating a well developed collinear ferrimagnetic state throughout the long range ordered regime presented for two selected temperatures in Fig. 4.12. Fig. 4.13 also shows the temperature dependence of the interstitial field and the relative field distribution $\Delta B_\mu / B_\mu^0$ derived from λ_{trans}. Where $\Delta B_\mu = \lambda_{trans}/\gamma_\mu$ is a width of field distribution and B_μ^0 is the saturation value of the interstitial field (T → 0).

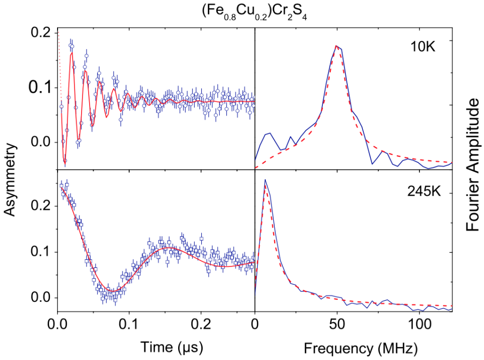

Figure 4.12: Zero field spectra of $Fe_{0.8}Cu_{0.2}Cr_2S_4$ at 10 K and 245 K in company with fast Fourier transformation of the spectral data (from Kalvius et al. [2013]).

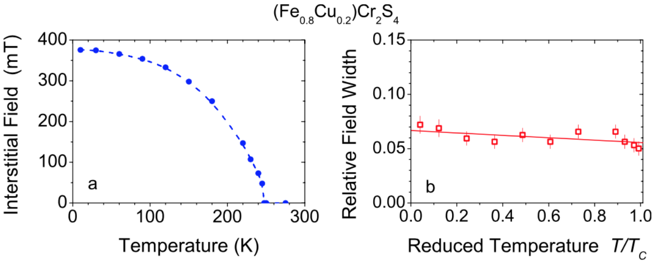

Figure 4.13: Temperature dependence of the interstitial field relative and field distribution of $Fe_{0.8}Cu_{0.2}Cr_2S_4$ on the reduced temperature with T_c = 247 K (from Kalvius et al. [2013]).

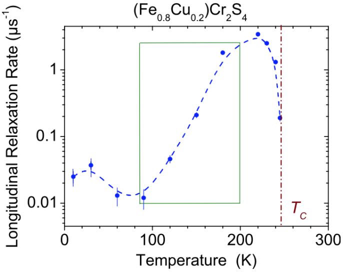

Figure 4.14: Temperature dependence of the longitudinal relaxation rate of $Fe_{0.8}Cu_{0.2}Cr_2S_4$. The green box indicated as a region with an unexpected increasing on the longitudinal relaxation rate (from Kalvius et al. [2013]).

Fig. 4.14 exhibits the temperature dependence of longitudinal relaxation rate λ_{long}, which has a peculiar behavior. There are marked two regions with a quite uncommon behavior; one is a fast increase of λ_{long} in the temperature range between 90 and 200 K and the other is the decrease of λ_{long} on approach of the Curie temperature. No explanation for this unexpected behavior could be given.

4.4.3

$Fe_{0.5}Cu_{0.5}Cr_2S_4$

ZF μSR on the $Fe_{0.5}Cu_{0.5}Cr_2S_4$ has been done by Kalvius et al. [2008] and the same fitting strategy as given for $Fe_{0.8}Cu_{0.2}Cr_2S_4$ was followed. Some selected spectra are depicted in Fig. 4.15 indicating changes in magnetic structure with changing temperature. They ascribed the single cosine oscillation pattern as a sign for collinear ferrimagnetism in agreement with the neutron diffraction data.

The interesting part of their analyses has been depicted in Fig. 4.16. The temperature dependence of the interstitial field displays a discontinuous behavior between 90 K and 200 K (Fig. 4.16) and is interpreted with an instability of the spin lattice leading to a collective canting of spins. The variation of the relative field distribution width as seen from λ_{trans} and the magnetic moment fluctuation rate derived from λ_{long} with the temperature also reveal an anomaly between 90 K and 200 K.

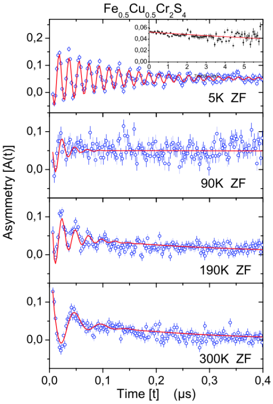

Figure 4.15: ZF spectra of $Fe_{0.5}Cu_{0.5}Cr_2S_4$ at some selected temperature. The solid line is fitted by a single cosine oscillation pattern given in eq. 4.2 (from Kalvius et al. [2008])

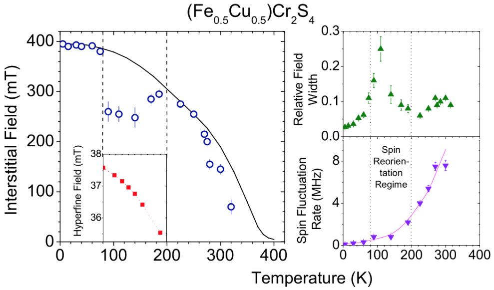

Figure 4.16: Interstitial filed B_μ (left), The relative field and the spin fluctuation rate (right) vs temperature for $Fe_{0.5}Cu_{0.5}Cr_2S_4$. The box inside is the hyperfine field derived from Mössbauer measurements on the same material (from Kalvius et al. [2013]).

4.4.4

$Fe_{0.2}Cu_{0.8}Cr_2S_4$

The literature data (e.g. Haacke and Beegle [1967], Lotgering et al. [1969]) had proposed from magnetization data that this compound is ferromagnetic. The studies on $Fe_{0.2}Cu_{0.8}Cr_2S_4$ have been performed to answer the fundamental question whether the high copper amount allows magnetic long range order.

Kalvius et al. [2013] studied $Fe_{0.2}Cu_{0.8}Cr_2S_4$ by Mössbauer spectroscopy and also μSR. Their research establishes that this compound is still ferrimagnetic. Some examples of the ZF spectra are presented in Fig. 4.17 for low- and high-time resolution.

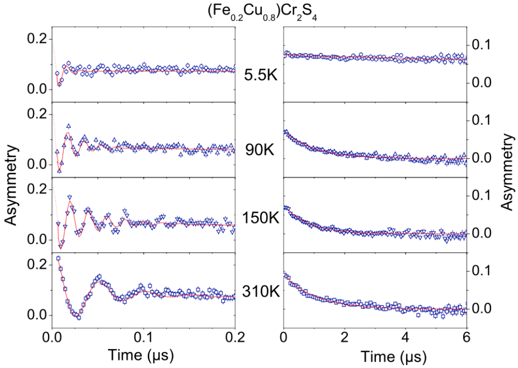

Figure 4.17: ZF spectra of the $Fe_{0.2}Cu_{0.8}Cr_2S_4$ at different temperatures in long range ordered regime. The left panels show the high time resolution of the initial part of spectra to show the oscillatory pattern. The low time resolution given in right panels are to show the longitudinal relaxation rate. The solid lines are least square fits to eq. 4.2 (from Kalvius et al. [2013]).

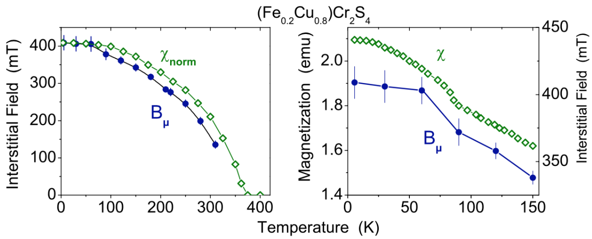

Figure 4.18: Temperature variations of the magnetization (χ_{norm}) in 1 T (open symbols) and the interstitial field B_μ in $Fe_{0.2}Cu_{0.8}Cr_2S_4$ (left). Zoomed of the temperature dependence of the interstitial field and magnetization around 100 K (right) (from Kalvius et al. [2013]).

They have been fitted with a single cosine oscillation pattern signifying a simple ferrimagnet order. Analyses show several unusual features according to the temperature dependence of the interstitial field, λ_{trans} and λ_{long} as illustrated in Fig. 4.18 and Fig. 4.19.
The temperature dependence of the interstitial field has an irregularity between 60 K and 90 K when looking in more detail (zoomed around 100 K in Fig. 4.18 right) which indicates some changes in magnetic properties.

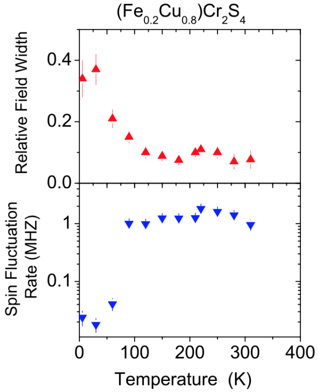

Figure 4.19: Temperature variations of the relative field width obtained from λ_{trans} (top). Magnetic spin fluctuation rate taken from λ_{long} in $Fe_{0.2}Cu_{0.8}Cr_2S_4$ (right) (adopted from Kalvius et al. [2013]).

The variation of the relative field width and spin fluctuation rate with temperature (Fig. 4.19) demonstrate an unusual behavior; at low temperature the magnetic relative field is high and spin fluctuation rate is small indicating that the magnetic moment fluctuations are static accompanied with a distribution of disorder on a short-range scale in long range order. But above 90 K the fluctuation of moments are dynamic indicating short-range order. In summary from earlier μSR studies; there are many puzzling and not yet understood details especially in the static field distribution and the temperature dependence of spin fluctuations that need further studies.

4.5

Further Investigations Using Various Methods

The study of the magnetic and electrical properties of the $FeCr_2S_4$ and $CuCr_2S_4$ compounds from a series of solid solutions has started since early 1970s. The bulk magnetic properties are summarized for all Cu concentration in references (Haacke and Beegle [1967], Lotgering et al. [1969], Tsurkan et al. [2005]).

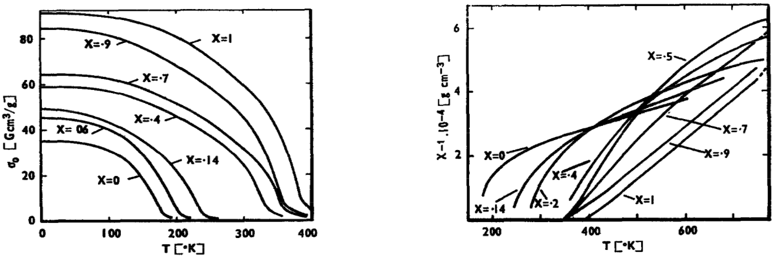

Figure 4.20: Temperature dependence of the reciprocal of the magnetic susceptibility χ (left). Saturation magnetization vs temperature for different concentration of the $Fe_{1-x}Cu_xCr_2S_4$; $x = 0.0, 0.06, 0.14$ single crystal samples (right) (taken from Haacke and Beegle [1967]).

One of the first studies has been done by Haacke and Beegle [1967] performing the magnetic measurements using the Faraday method for nine different compositions of the system $Fe_{1-x}Cu_xCr_2S_4$; $x = 0.0, 0.06, 0.14,\ 0.2, 0.4, 0.5, 0.7, 0.9, 1.0$. Fig. 4.20 shows the temperature dependence of the reciprocal of the specific susceptibility χ and the specific saturation magnetization for different concentration x in the $Fe_{1-x}Cu_xCr_2S_4$ system reporting the following results; the χ^{-1} curves show typical ferrimagnetic behavior at lower Cu concentrations. Only on approaching T_c they show a convex curvature in accordance with Néel's theory of ferrimagnetism. At high temperature they follow a Curie-Weiss low. For high copper concentrations the inverse susceptibility χ^{-1} curves show straight lines close to T_c indicate a ferromagnetic material. This is not the case in the intermediate range of concentration ($x \sim 0.5$). Saturation magnetization data were measured down to 77 K and then extrapolated to 0 K (they used the data from Lotgering et al. [1969] as a guide down to liquid helium temperatures).

The work of both Lotgering et al. [1969] and Haacke and Beegle [1967] give the same behavior for T_c for different concentrations. Upon substitution of Fe ions in tetrahedral sites by non-magnetic Cu ions in the ferrimagnetic compound $FeCr_2S_4$, T_c increases which can be attributed to the appearance of Fe^{3+} ions assuming the A-B superexchange interaction is stronger for A-B = $Fe^{3+}Cr^{3+}$ than for A-B = $Fe^{2+}Cr^{3+}$. T_c is not increasing linearly with concentration x and there is a kink around $x = 0.5$ which has been proposed to the disappearance of Fe^{2+}. They also suggested that the switch from ferrimagnetic to ferromagnetic can be traced from the shape of susceptibility curves to occur around $x \sim 0.3$-0.4.

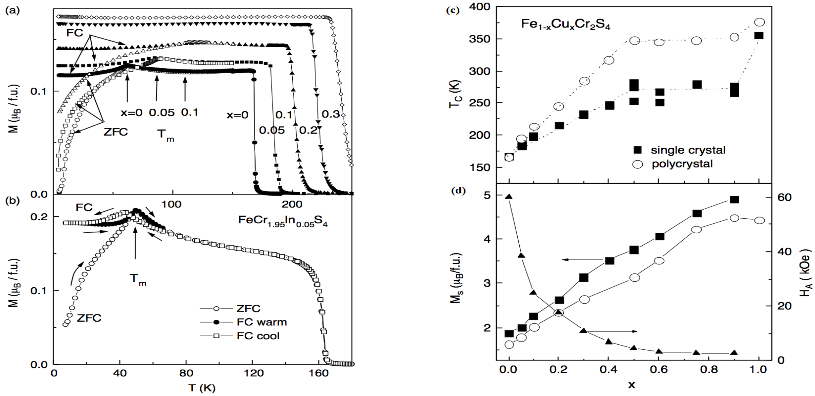

Figure 4.21: (a, b) ZFC and FC magnetization vs temperature measured in a field 100 Oe for the single crystal of the $Fe_{1-x}Cu_xCr_2S_4$; $0.0 \leq x \leq 0.3$. Variation with the Cu concentration x: (c) of the curie temperature T_c; (d) of the saturation magnetization M_s and the anisotropy field H_A for the poly- and single crystals in the $Fe_{1-x}Cu_xCr_2S_4$ compounds (adopted from Tsurkan et al. [2005]).

Magnetic studies by Tsurkan et al. [2005] on poly- and single crystals of $Fe_{1-x}Cu_xCr_2S_4$ were performed using Vibrating Sample and SQUID magnetometers in a temperature range of 2-400 K and magnetic fields up to 70 kOe. Fig. 4.21 presents the magnetic data taken from Tsurkan et al. [2005] where they explain the results as following:

The temperature dependence of magnetization in Fig. 4.21a shows the onset of the long-range order at the Curie temperature T_c determined by kink-point method, in addition they find a cusp at a temperature T_m upon decreasing temperature. The splitting of ZFC and FC magnetization and correspondent onset of coercivity and remanence has been explained with a spin-glass like behavior. The magnetization curve for $Fe_{0.9}Cu_{0.1}Cr_2S_4$ shows $T_m \sim 120\ K$ and $T_c \sim 220$ K. The cusp at T_m is smeared out for $x > 0.2$. It is associated with the onset of orbital ordering accompanied by a structural lattice transformation.

Fig. 4.21 (c and d) shows the variation of the basic magnetic parameters with Cu substitution. T_c in Fig. 4.21c has the same variation as shown in the data by Haacke and Beegle [1967] with the same interpretation attributed mainly to the variation of the superexchange interactions.

As mentioned before, there is no reliable information for which substitution x ferrimagnetism switches to the ferromagnetism. Neutron diffraction data which exist only for $Fe_{0.5}Cu_{0.5}Cr_2S_4$ indicate a ferrimagnetic structure with identical ordering temperatures of the two ferromagnetic sublattices. Also the temperature dependence of sublattice magnetization develop in parallel (Lang et al. [2000]).

High-resolution x-ray synchrotron powder- diffraction, magnetic-susceptibility, sound-velocity, thermal-expansion, and heat-capacity studies performed by Tsurkan et al. [2010] reported further interesting data on $FeCr_2S_4$.

High-resolution x-ray diffraction was used to examine the long-standing problem about the deviation from the cubic spinel structure below ~ 60 K. As illustrated in Fig. 4.22a, the temperature dependence of the diffraction lines reveals a broadening of all Bragg reflections at low temperature. This broadening starts at around 60 K and reaches a maximum at T_{oo} which they have interpreted with structural anomalies at these temperatures. These changes are rather small and one cannot conclusively determine a deviation from cubic. However, the temperature dependence of the mean square displacement for all ions show a clear peak close to the orbital order transition T_{oo} (shown as an inset of Fig. 4.22a). They conclude that this anomaly is related to a cooperative Jahn-Teller distortion. The displacement parameters are largest for Fe and smallest for Cr. The small displacement of Cr means that the chromium ions are also involved in the cooperative JT transition which is in agreement with the proposals of Feiner [1982] and Goodenough [1964].

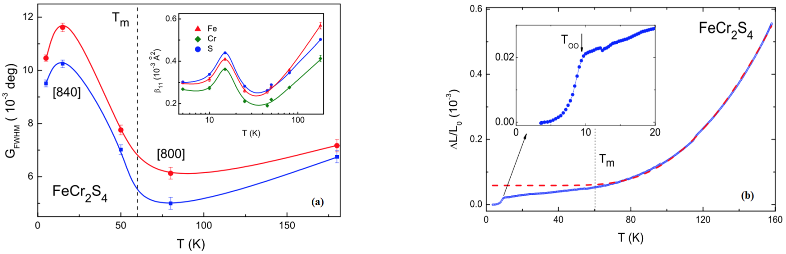

Figure 4.22: (a) Temperature dependence of diffraction linewidth; Inset: temperature dependence of displacement parameters for involved ions in $FeCr_2S_4$. (b) Normalized thermal expansion vs temperature in $FeCr_2S_4$ (from Tsurkan et al. [2010]).

The structural anomalies also can be seen in thermal expansion measurement in Fig. 4.22b. Below 60 K, the thermal expansion data starts to deviate from the extrapolated curve for a normal anharmonic solid coinciding with the broadening of the Bragg peaks. They have explained a enhanced shrinking of the lattice below 60 K as the onset of short-range orbital ordering. Also significant drop in the thermal expansion at T_{oo} indicates the lattice is strongly involved in the cooperative JT effect. Their results are well comparable with the Raman scattering data (Choi et al. [2007]).

The most interesting part of their work is the results taken from magnetic susceptibility and heat capacity measurements. Fig. 4.23a demonstrates the temperature dependence of ultrasound (right scale) and magnetization data (left scale). A clear signature of the ferrimagnetic transition at 165 K, a strong anomaly at 60 K and a small kink at approximately 9 K have been indicated by black arrows in Fig. 4.23a. Field-cooled (FC) and zero field-cooled (ZFC) susceptibility display a significant onset of spontaneous magnetization at T_c which is sharp at 165 K (without broadening seen in μSR studies). A strong continuous decrease close to 60 K is interpreted as a spin-reorientation anomaly signaling a significant change from ferrimagnet spin structure to a noncollinear helical structure (as proposed from μSR (Kalvius et al. [2010])). They interpret the small deviation at ~ 9 K to be related to

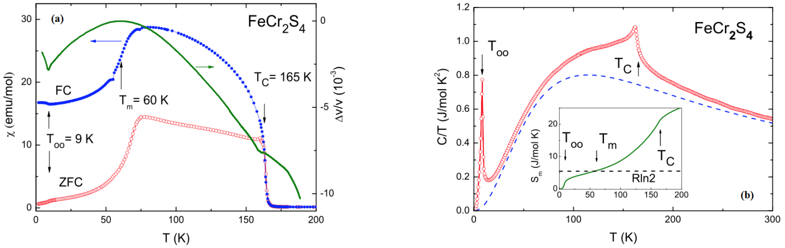

Figure 4.23: (a) Temperature dependence of ZFC and FC susceptibility in an external magnetic field H = 100 Oe (left scale) and the relative change in the longitudinal sound velocity (right scale, solid green line). (b) Temperature dependence of heat capacity C/T indicates T$_{oo}$, T$_c$. A blue dashed line shows the simulated lattice contribution. Magnetic entropy of the lattice contribution (inset) indicates also T$_m$ (taken from Tsurkan et al. [2010]).

the onset of long-range orbital order via the cooperative JT effect.

The right scale of Fig. 4.23a presents the temperature dependence of longitudinal sound velocity which is normalized to its maximum value. The small dip close 160 K indicating the onset of ferrimagnetic order, a maximum at 60 K and decreasing of the sound velocity toward lower temperature signifying the onset of short-range orbital ordering which is possibly induced by the magnetic transition at T$_m$, and at the last, increasing again at T$_{oo}$ results in the onset of long-range orbital ordering as concluded by Tsurkan et al. [2010].

Finally, they represent the temperature dependence of the specific heat divided by temperature C/T in FeCr$_2$S$_4$ in Fig. 4.23b. The simulated lattice contribution has been plotted with blue dashed line. Two anomalies are found in experimental data. One at T$_c$ = 165 K corresponds to the onset of ferrimagnet order. A second anomaly is close to 10 K and attributed to the cooperative Jahn-Teller transition with the onset of the long-range orbital order. These anomalies is confirmed by the temperature dependence of the magnetic entropy S_m which is shown in the inset of Fig. 4.23b indicating two pronounced steps at T$_c$ and T$_{oo}$. But no anomaly is found at Fe$_m$ in specific heat data.

They also have done further analysis of the low temperature specific heat to analyze the spin-orbit splitting (δ) of the electronic e$_g$ ground doublet of Fe^{2+}. The size of δ can be determined by fitting the low temperature data using an expression like $C(t) = C_0 \exp(-\delta/T)$. They calculate $\delta = 18.3$ K which is close to the estimation $\delta = 17$ K derived from a vibronic coupling approach to the phase transition by Feiner [1982] and also in agreement with Engelke [2010].

Recently Bertinshaw et al. [2014] proved the conclusion of these measurements and also all these anomalies have been reported by Mössbauer experiments performed by many authors. All these experiments describe the observation of significant nonzero quadrupole shifts obviously by orbital fluctuations and local dynamic deviations from cubic symmetry.

4.6

Colossal Magnetoresistance Effect in $Fe_{1-x}Cu_xCr_2S_4$

Changing of the electrical resistivity due to an applied external magnetic field is called Magnetoresistance (MR) which is usually given by

$$MR = (\rho(H) - \rho(0))/\rho(0) \tag{4.3}$$

$\rho(0)$ and $\rho(H)$ are the electrical resistivities measured without and with applied external field H, respectively. The Magnetoresistance effect has been known since long, but the technological application of MR effect started when the giant negative magnetoresistance (GMR) was found in magnetic multilayers even at room temperature using in the magnetic storage devices. Finding of a higher magnetoresistance in mixed-valence perovskite, such as $La_{1-x}A_xMnO_3$ (A = Ca, Sr, or Ba), which is called colossal magnetoresistance (CMR), opened a new interest to use the transition metals based on materials with peculiar magnetoresistance effect (Jonker and Van Santen [1950], Salamon and Jaime [2001]).
A transition from paramagnetic insulating phase to a ferromagnetic metal phase with a cooperative Jahn-Teller distortion in octahedral sites is observed in stoichiometric $LaMnO_3$. In the vicinity of this transition, a large change in the electrical resistance when applied magnetic field has been observed leading to the CMR effect. For the doping range $x \sim 0.2$-0.4, the double-exchange mechanism is responsible for the observed *CMR* effect explained by the electron hopping between Mn^{3+} and Mn^{4+} ions (Jonker and Van Santen [1950]). Millis et al. [1995] presented "*a solution of the double-exchange model*" revealing the double-exchange mechanism is not only responsible for the CMR effect, and a strong electron-phonon coupling due to Jahn-Teller effect is also supposed to play an important role. The formation of self-trapped small polarons (the polaron conductivity) coupled with Jahn-Teller distortion near T_c has been proposed, e.g., by Salamon and Jaime [2001]. On the other hand, CMR in some other systems, such as $Tl_2Mn_2O_7$, the spinel $CdCr_2Se_4$, and Eu chalcogenides, can not be explained by double-exchange mechanism or lattice polarons anymore. In these systems, the appearance of CMR is due to the strong scattering of charge carriers by spin fluctuations associated with the ferromagnetic ordering (Majumdar and B. Littlewood [1998], Seo et al. [1997], Shimakawa et al. [1997], Subramanian et al. [1996]).
$Fe_{1-x}Cu_xCr_2S_4$ also exhibit a very large negative magnetoresistance effect in the vicinity of the transition temperature T_c (Ramirez et al. [1997]). Although, $Fe_{1-x}Cu_xCr_2S_4$ is structurally and chemically similar to $CdCr_2Se_4$ and also its CMR is comparable to that observed in manganese perovskite, the origin of CMR in this system is still unclear. Fig. 4.24 shows the temperature dependence of the magnetization M, thermopower S, resistivity ρ, and the magnetoresistance MR for $x = 0.0$ and 0.5 measured by Ramirez et al. [1997]. The difference in saturation moment between $x = 0.0$ and 0.5 is attributed to the difference Fe concentration by Cu doping (Fig. 4.24). The temperature dependent thermopower S (Seebeck coefficient) shows an extrinsic p-type semiconductor for $x = 0.0$ and n-type semiconductor for $x = 0.5$.
Fig. 4.24 also shows the temperature dependence of resistivity ρ for both samples ($x = 0.0, 0.5$) at several different values of applied field. The resistivities ρ ($x = 0.0, 0.5$) reveal

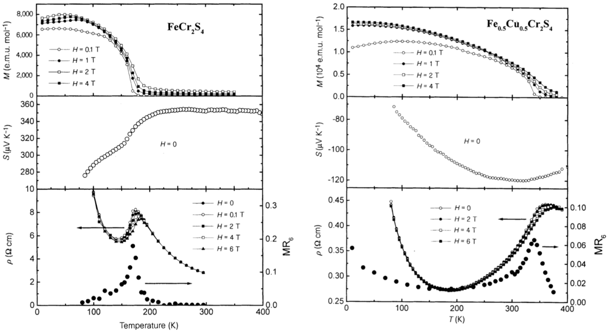

Figure 4.24: The temperature dependence of magnetization (M), thermopower (S), resistivity (ρ) and magnetoresistance (MR) for $FeCr_2S_4$ (left) and $Fe_{0.5}Cu_{0.5}Cr_2S_4$(right) (taken from Ramirez et al. [1997]).

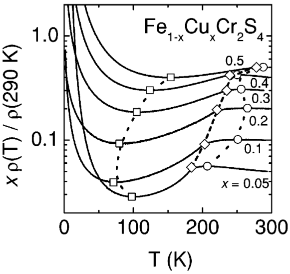

Figure 4.25: The electrical resistivity of $Fe_{1-x}Cu_xCr_2S_4$ normalized at T = 290 K and multiplied with *Cu* concentration x. Cu concentration x are indicated in the figure. The Curie temperature T_c (⋄, dashed line) and the positions of the local minima (□, dotted line) and maxima (○, dotted line) are given (adopted from Ramirez et al. [1997]).

semiconducting behavior for $T > T_c$ and $T \ll T_c$, while a metallic-like behavior is observed below T_c. The magnetoresistance MR for both $x = 0.0$ and 0.5 displays a peak at T_c.
Fritsch et al. [2003] also investigated the electronic transport and magnetic properties of $Fe_{1-x}Cu_xCr_2S_4$ (single crystal samples). The temperature dependence of resistivity ρ are plotted in Fig. 4.25, in which the magnetic transition T_c, position of the local minima below T_c and maxima above T_c are marked. To explain the CMR, Fritsch et al. [2003] proposed the triple-exchange model via hopping between Fe^{2+} and Fe^{3+} for the conduction mechanism. They also mentioned that the system cannot be described by an pure ionic model and introduced an ionic band picture which will be discussed in section 6.1.

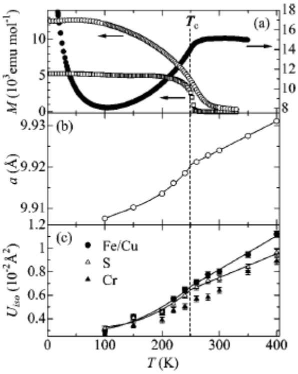

Figure 4.26: The temperature dependence of (a) magnetization M (H = 0.01 T and 2 T) and electric resistivity ρ (right scale), (b) the cubic lattice parameter a, and (c) the isotropic Debye-Waller factor U_{iso} for each atomic site in $Fe_{0.8}Cu_{0.2}Cr_2S_4$ (from Tachibana et al. [2005]).

Tachibana et al. [2005] suggested that the interrelation between the charge, spin, and lattice degree is strongly correlated to the observed CMR in $Fe_{1-x}Cu_xCr_2S_4$. A strong drop in resistivity ρ by onset of ferrimagnetic order is a sign of the CMR (Fig. 4.26a). Fig. 4.26b shows strong coupling between the lattice and magnetism where a significant lattice contraction occurs at T_c in the temperature dependence of the cubic lattice parameter a (similar to observed abrupt reduction of a in the CMR perovskites (e.g. Radaelli et al. [1996])). Fig. 4.26c presents the Debye-Waller factor U_{iso} for each atomic site, resembling the temperature dependence of the cubic lattice parameter a. A significant change in U_{iso} at T_c for Fe/Cu site is ascribed to the distortion of $Fe^{2+}S_4$ as expected for the Jahn-Teller active ion Fe^{2+} in tetrahedrally symmetry. Also Tachibana et al. [2005] concluded that the Jahn-Teller distortion stays dynamic at all temperature for $x \geqslant 0.2$.

Chapter 5

Results of Present Work

5.1

Experimental Details

All the powder samples of $Fe_{1-x}Cu_xCr_2S_4$ used in our studies have been provided by V. Tsurkan[1]. Notably all measurements, Mössbauer spectroscopy, μSR, and magnetization have been performed on the same specimen. Polycrystalline $Fe_{1-x}Cu_xCr_2S_4$ were prepared by solid state reaction from high purity elements (99.99% and 99.999%). Solid state mixtures of the respective mixture ratios were annealed in chalcogen atmosphere (Tsurkan et al. [2004, 2005, 2010]).

5.1.1

X-ray Diffraction

X-ray diffraction was used to check phase homogeneity and the composition of our samples and revealed all the samples to be single phase spinels. The lattice parameter data of $Fe_{1-x}Cu_xCr_2S_4$ for different concentration provided by V. Tsurkan, are presented in Fig. 5.1. The substitution of Fe by Cu gives a linear dependence of the lattice constant on the Cu concentration and follows Vegard's law. Note that the observed linear decrease of the lattice parameter with Cu concentration should be reflected in a variation of the magnetic superexchange that is sensitive to interatomic distance (Tsurkan et al. [2005]).

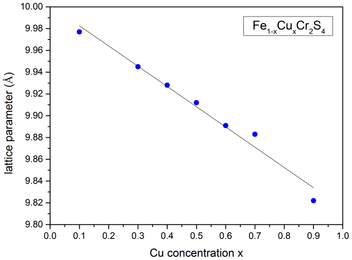

Figure 5.1: Variation of the lattice parameter with the Cu concentration x for polycrystalline $Fe_{1-x}Cu_xCr_2S_4$.

---

[1] Experimental Physics V, Center for Electronic Correlations and Magnetism, Augsburg University, *D*-86159 Augsburg, Germany & Institute of Applied Physics, Academy of Sciences, 2028 Chisinau, Republic of Moldova

5.1.2

Magnetization

Magnetization data of all samples have been investigated under field cooling (FC) and zero field cooling (ZFC) in a temperature range of 2 - 400 K under small and also high magnetic fields. The measurements have been repeated twice for some Cu concentrations, in order to look for corresponding anomalies seen in low temperature Mössbauer and also μSR data. The magnetic susceptibility of $Fe_{1-x}Cu_xCr_2S_4$ has been measured using Quantum Design MPMS, and SQUID magnetometers, by D. Menzel [2] and V.Tsurkan.

5.1.3

Mössbauer Spectroscopy

We have performed ^{57}Fe Mössbauer absorption experiments in a transmission geometry using a standard spectrometer with sinusoidal velocity sweep. As 14.4 keV γ-radiation source we used about 40 mCi of ^{57}Co in a Rh matrix kept at room temperature. Powder absorbers were mixed with some sugar powder and enclosed into nylon containers that is screwed to a Cu-clamp at the end of a sample stick (see Fig. 5.2). Using sugar powder helps to have a uniform and fixed distribution of material inside the sample holder.

The sample holder (Fig. 5.2) is positioned in the exchange gas (He) chamber of a He flow cryostat (Cryovac). The temperature at the absorber was measured via a Si diode sensor fixed to the Cu-clamp. Temperature regulation occurs via a Lakeshore controller operating a heater attached to the heat exchanger of the cryostat that is in direct contact with the exchange gas volume. Accuracy and stability of absorber temperature were better than 0.5 K. Instead of He it is possible to use liquid nitrogen as coolant above 80 K.

More than hundred fifty spectra on $Fe_{1-x}Cu_xCr_2S_4$ have been taken for the whole series of Cu concentrations and have been fitted with the complete hyperfine Hamiltonian introduced in section 3.2.4 using the "Full Static Hamiltonian Site Analysis" model within the Recoil software package appropriate for powder absorbers.

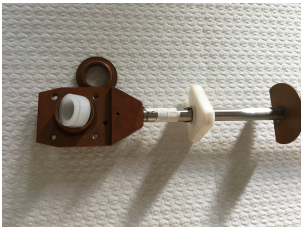

Figure 5.2: Sample holder and container used in Mössbauer measurements.

---

[2] Institute for Physics of Condensed Matter, Technical University Braunschweig, D−38106 Braunschweig, Germany

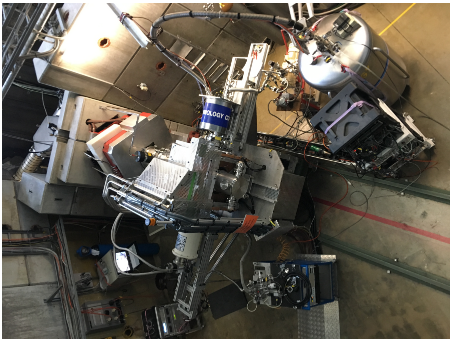

Figure 5.3: GPS spectrometer at PSI.

5.1.4
μSR

The μSR spectra were measured in zero and weak transverse applied field between 4 K and 300 K with the surface muons beam πM3 using the GPS spectrometer at the Swiss Muon Source (see Fig. 5.3) of Paul Scherrer Institute, Villigen (Switzerland).
The $Fe_{1-x}Cu_xCr_2S_4$ polycrystalline powders were mounted between thin aluminized Mylar foils and located in the center tube of a helium-flow cryostat which ensures proper and uniform temperatures. The temperature stability was better than 0.1 K. The VETO mode (PSI [2017] web page) was enabled to suppress the background signal from muons stopped outside the samples. The time resolution was 1.25 ns and the initial spectrometer dead time was ~ 5 ns. Indeed, as checked by TF data, no resolvable background signal existed in the present data except for the sample $x = 0.1$.
All μSR spectra were analyzed to determine the appropriate spectral function $P(t)$ introduced in section 3.3 using the program musrFit (Suter and Wojek [2011]). In order to obtain meaningful results, the α parameter of the detector set-up (introduced in eq. 3.17) had to be determined for each sample. This is done by TF measurements in the paramagnetic regime when the time dependent asymmetry function $A(t)$ for the two opposing detectors, oscillates around zero. Once α was found for a given sample set-up, it was fixed and used to fit the ZF asymmetry signal. Fitting the TF signals below the ordering temperature gives also an information about an eventual non-magnetic background fraction which should be kept for all fitted data for a given sample as a background asymmetry.

5.2
Magnetization Measurements

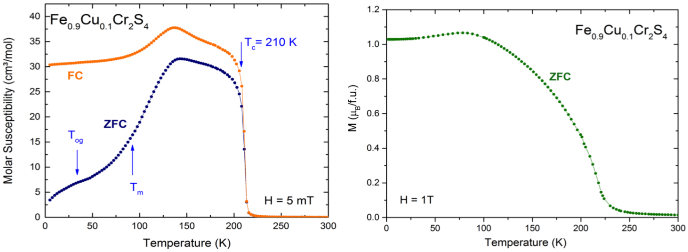

Figure 5.4: Magnetic measurements of the Thiospinel $Fe_{0.9}Cu_{0.1}Cr_2S_4$. Left: ZFC and FC temperature dependent magnetic susceptibility measured under an applied field 5 mT show several anomalies at different temperatures. Right: Temperature dependence of magnetization M under 1 T external field.

Fig. 5.4 shows the ZFC and FC magnetic susceptibilities χ of $Fe_{0.9}Cu_{0.1}Cr_2S_4$ collected under an applied field of 5 mT and the saturation magnetization curve under an applied field 1 T. The magnetic transitions are observed in the temperature dependence magnetic susceptibility of this compound. A high temperature transition around 210 K, where the magnetic susceptibility increases, represents the magnetic transition from paramagnetic to ferrimagnetic, where the spins of the Fe and Cr align in opposite direction. The susceptibility demonstrates the large irreversibility between the ZFC and FC curves that begin to separate below T_c. In both ZFC and FC susceptibility curves a cusp-like anomaly is observed near 130 K, which vanishes under 1 T applied fields. With increasing the applied field to 1 T, this anomaly moves to lower temperature and finally indicates a convex type maximum around 100 K. Another bump appears at approximately 40 K in ZFC curve.

In order to denote the similarities and differences between $Fe_{0.9}Cu_{0.1}Cr_2S_4$ and $FeCr_2S_4$, we mark T_c, T_m, and T_{og} on the ZFC and FC curves for $Fe_{0.9}Cu_{0.1}Cr_2S_4$ as indicated in Fig. 5.4. These anomalies have been introduced by Tsurkan et al. [2010] as already mentioned (see Fig. 4.23). Consequently, the substitution of the Fe ions by Cu increases strongly the value of T_c, T_m and T_{og} compared to the study of Tsurkan et al. [2010] on $FeCr_2S_4$[3].

Fig. 5.5 shows the molar susceptibilities χ of $Fe_{0.8}Cu_{0.2}Cr_2S_4$ vs. temperature for ZFC and FC. The curves show a characteristic divergence of χ at T_c upon cooling. They are only slightly different compared to $x = 0.1$. Actually this sample was prepared in a different preparation series and already used for μSR measurements published by Kalvius et al. [2013]. T_m can be estimated to be around 100 K, and T_{og} around 40 K.

Similar to other mentioned samples, three magnetic transitions are observed in the temperature dependent magnetic susceptibility of $Fe_{0.7}Cu_{0.3}Cr_2S_4$ (Fig. 5.6). A high temperature transition occurs at 288 K where the paramagnetic fraction is going to order ferrimagnetically. At about 120 K, another anomaly is observed in both ZFC and FC measurements of the temperature dependent magnetic susceptibility as well as in the field magnetization attributed to T_m. And T_{og} seems to be around 40 K where one can see a small kink.

---

[3] Note that the samples used for both studies (ours and Tsurkan et al. [2010]) were made by the same preparator using the same procedure.

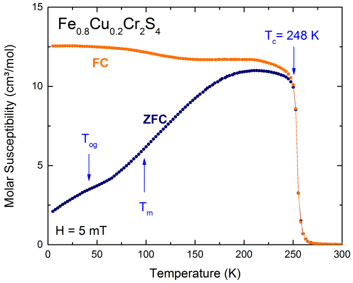

Figure 5.5: Magnetic measurements of the Thiospinel $Fe_{0.8}Cu_{0.2}Cr_2S_4$. The ZFC and FC temperature dependent magnetic susceptibility measured under an applied field 5 mT show several anomalies at different temperatures.

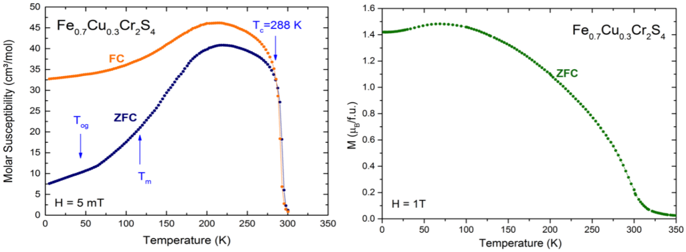

Figure 5.6: Magnetic measurements of the thiospinel $Fe_{0.7}Cu_{0.3}Cr_2S_4$. Left: ZFC and FC temperature dependent magnetic susceptibility measured under an applied field 5 mT show several anomalies at different temperatures. Right: Temperature dependence of magnetization *M* under 1 T external field.

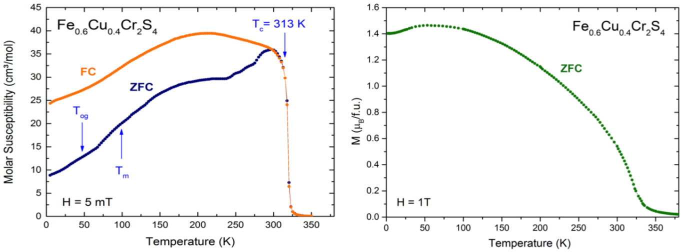

Figure 5.7: Magnetic measurements of the Thiospinel $Fe_{0.6}Cu_{0.4}Cr_2S_4$. Left: ZFC and FC temperature dependent magnetic susceptibility measured under an applied field 5 mT show several anomalies at different temperatures. Right: Temperature dependence of magnetization *M* under 1 T external field.

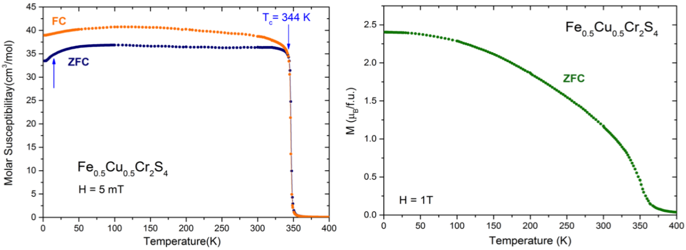

Figure 5.8: Magnetic measurements of the Thiospinel $Fe_{0.5}Cu_{0.5}Cr_2S_4$. Left: ZFC and FC temperature dependent magnetic susceptibility measured under an applied field 5 mT show several anomalies at different temperatures. Right: Temperature dependence of magnetization M under 1 T external field.

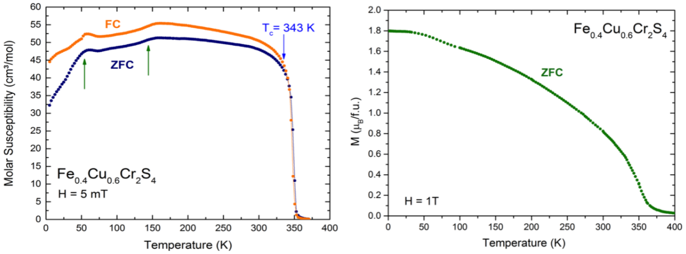

Figure 5.9: Magnetic measurements of the Thiospinel $Fe_{0.4}Cu_{0.6}Cr_2S_4$. Left: ZFC and FC temperature dependent magnetic susceptibility measured under an applied field 5 mT show several anomalies at different temperatures. Right: Temperature dependence of magnetization M under 1 T external field.

For $x = 0.4$, Fig. 5.7 illustrates the same behavior as observed for lower Cu concentration, with two anomalies at about 100 K and 40 K ascribed to T_m and T_{og}, respectively. The magnetic ordering transition is at 313 K. There is a significant kink around 250 K in ZFC measurement which has by now unknown origin.

Magnetization at low (5 mT) and high magnetic (1 T) fields for $Fe_{0.5}Cu_{0.5}Cr_2S_4$ are presented in Fig. 5.8. It is obvious from the magnetization data that the ordering temperature is at 344 K. Compared to the other by now mentioned compounds, the magnetization curves appear to be different. Also T_m and T_{og} are not visible in the magnetization data. ZFC susceptibility exhibits a reduced low temperature saturation value when compared to the FC susceptibility data illustrating domain behavior. These anomalies do not seem to related to orbital ordering and Jahn-Teller effect because of low Fe^{2+} quantity. Later in our μSR data this anomaly will interpreted with a spin glass state.

Temperature dependent magnetic susceptibility measurements of $Fe_{0.4}Cu_{0.6}Cr_2S_4$ performed in a 5 mT and 1 T applied magnetic fields show two peaks below the ordering temperature T_c = 343 K, close to 160 K and 60 K as well as a fast decrease toward lower temperatures below 60 K, as documented in Fig. 5.9. These two peaks have also been

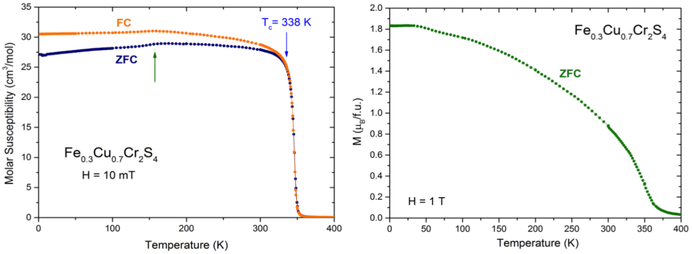

Figure 5.10: Magnetic measurements of the Thiospinel $Fe_{0.3}Cu_{0.7}Cr_2S_4$. Left: ZFC and FC temperature dependent magnetic susceptibility measured under an applied field 5 mT show several anomalies at different temperatures. Right: Temperature dependence of magnetization M under 1 T external field.

observed in μSR data (see later) and are supposed to be related to a change in magnetic structure. Fig. 5.9 shows the temperature dependent magnetization in high applied field which show a cusp-like anomaly around 60 K.
Fig. 5.10 shows the temperature dependence of magnetization for $Fe_{0.3}Cu_{0.7}Cr_2S_4$ at low and high fields. The Curie temperature is T_c = 338 K. A small cusp-like feature is present at about 160 K in the magnetization curve under low field.

5.3

Mössbauer Spectroscopy

In this section we consider separately the two regions of Cu concentration: $0 \leqslant x < 0.5$ and $0.5 \leqslant x < 0.9$. The spectra for low concentration $0 \leqslant x < 0.5$ have been fitted with a superposition of several hyperfine patterns showing strong changes of hyperfine parameters with temperature similar to $x = 0$. They follow very similar systematics as described in the following. Spectra for concentration $0.5 \leqslant x < 0.9$ are distinctly different, they are better defined with sharper lines and a more uniform behavior.

5.3.1

Mössbauer Results for the $0 \leqslant x < 0.5$ Concentration Region

For this concentration range we refer to the earlier data by Engelke [2010], Engelke et al. [2011]. We apply a general strategy for fitting using a superposition of non-magnetic (above T_c) or magnetic hyperfine patterns (below T_c). We first describe the approach for $x = 0.1$; then for the higher doped compounds we refer to the changes observed compared to the previously described concentration in the sequence.

5.3.1.1

$Fe_{0.9}Cu_{0.1}Cr_2S_4$

^{57}Fe Mössbauer spectra for the $Fe_{0.9}Cu_{0.1}Cr_2S_4$ have been taken at various temperatures between 4 K and room temperature (RT). Some representative spectra for different regimes are presented in Fig. 5.11 (for a complete compilation see Appendix A.1). Below T_c we see a wide distribution of magnetic hyperfine patterns that need to be approximated using several subspectra with different hyperfine parameters.

Paramagnetic Regime above 210 K

The spectra of $Fe_{0.9}Cu_{0.1}Cr_2S_4$, as seen in Fig. 5.11 at 215 K (also shown in Appendix A), exhibit two Fe^{2+} patterns (green (singlet) and blue (doublet) line), a singlet corresponding to Fe^{3+} in tetrahedral site (pink) and also a spectrum X (orange) caused by a low excess of iron occupying octahedral sites and thus lowering the symmetry at Fe^{2+} in A tetrahedral sites. This contribution has also been seen by Lotgering et al. [1975] and also Engelke [2010]. Spectra above the ordering temperature can be fitted in several ways and there is no unique solution. Therefore, in order to get systematic fitting for the spectra the relative area ratio for each site is kept as determined for the average area of each oxidation state below ordering temperature (see below). The obtained parameters at 215 K are given in table 5.1. Comparing to $x = 0$ (Engelke [2010]) the spectra cannot be fitted to only one single line with zero quadrupole splitting. The parameter needed for fitting are the center shift, the quadrupole splitting $QS = \frac{e^2qQ}{2}$, the line width (HWHM) and the area covered by the lines.

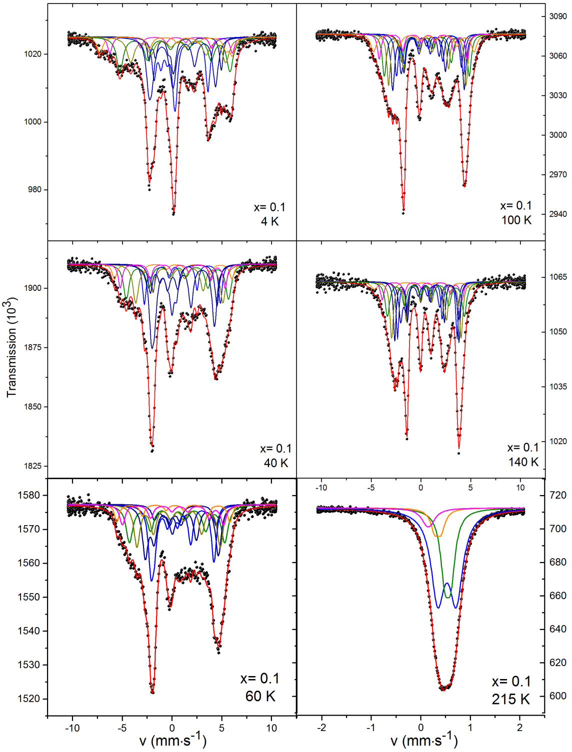

Figure 5.11: Mössbauer spectra of the $Fe_{0.9}Cu_{0.1}Cr_2S_4$ (x = 0.1) at various temperatures.

T (K)	Assignment	CS (mm · s^{-1})	*QS* (mm · s^{-1})	HWHM (mm · s^{-1})	Area (%)
215	Fe^{2+}	0.637(9)	0.37(1)	0.17(2)	59(2)
	Fe^{2+}	0.653(9)	0.12(1)	0.11(0)	27(1)
	Fe^{3+}	0.273(7)	0.04(1)	0.15(1)	6(1)
	spectrum X	0.441(2)	0.12(2)	0.12(1)	8(1)

Table 5.1: Adjusted parameters from Mössbauer spectra of $Fe_{0.9}Cu_{0.1}Cr_2S_4$ in paramagnetic regime.

Region between 215 K and 80 K

The spectra below 215 K reveal magnetic hyperfine splittings as seen from the measurement at 140 K in Fig. 5.11, and indicate magnetic order. The spectra in this region can be fitted with seven subspectra; spectrum X (8%), five subspectra corresponding to Fe^{2+} (86%), and one corresponding to Fe^{3+} (6%). The temperature variation of the center shift is plotted in Fig. 5.12. The center shift of Fe^{2+} is the area weighted average of center shifts of five subspectra.

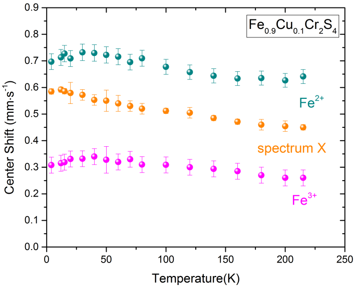

Figure 5.12: Temperature dependence of the center shift of $Fe_{0.9}Cu_{0.1}Cr_2S_4$ (x = 0.1) taken from Mössbauer evaluation.

Since the fit parameters of these patterns are highly correlated giving ambiguous possibilities for assignment of parameters, we decided to better present a qualitative development of parameters by taking area weighted averages of parameters for groups of subspectra. From the systematic variation of center shifts, quadrupole splittings and magnetic hyperfine fields we have grouped the subspectra to two group, named I and II, according to closely similar behavior of their hyperfine parameters. Group I refers to the area weighted averages of parameters of three sub-spectra having high values of polar angles, lower values of hyperfine field, and also high values of EFG (blue lines in the middle of spectrum). Group II refers to the area weighted averages of parameters of two sub-spectra having higher values of hyperfine field, and also nearly zero values of EFG (green lines). The temperature dependence of the magnetic hyperfine fields B_{hf} and quadrupole splittings QS are shown in Fig. 5.13 for the groups I and II in company with spectrum X.

At 200 K (see Fig. A.2 and 5.13a), the material starts to order magnetically, which is in agreement with the estimate from magnetization data of $T_c = 210\ K$ in Fig. 5.4. The following parameters can be extracted using the full static Hamiltonian: the center shift, the magnetic hyperfine field, the electric quadrupole splitting parameter $e^2qQ/2$, the line width, and the area. The asymmetry parameter η is zero in this temperature regime, i.e. no significant deviations from axial symmetry occur.

As already mentioned, for having a better visualization of the variation of hyperfine parameters, we took averages of the parameters of the subspectra. As presented in Fig. 5.13a and

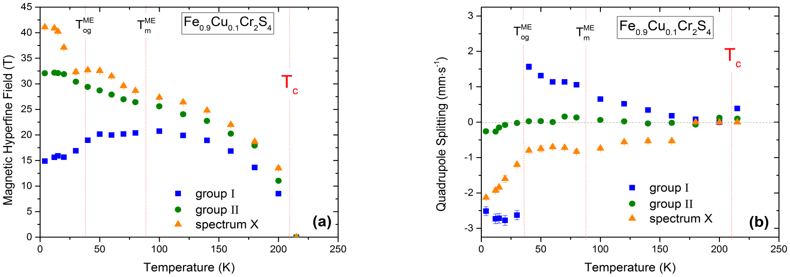

Figure 5.13: Temperature dependence of: (a) the magnetic hyperfine field; (b) the quadrupole splitting in $Fe_{0.9}Cu_{0.1}Cr_2S_4$. The group I are the area weighted averages of subspectra with lower magnetic hyperfine field and bigger quadrupole splitting. The group II are the area weighted averages of subspectra with high magnetic hyperfine field and small quadrupole splitting.

table 5.2, the magnetic hyperfine field grows from zero to values of 20.38 T and 26.40 T, for group I and II which is reached around T_m^{ME} = 80 K, respectively. The rise of magnetic hyperfine field for all spectral contributions in this region is continuous. Fig. 5.14a shows the magnetic hyperfine field of Fe^{3+} sites which is also increasing continuously to approximately 34 T at 80 K.

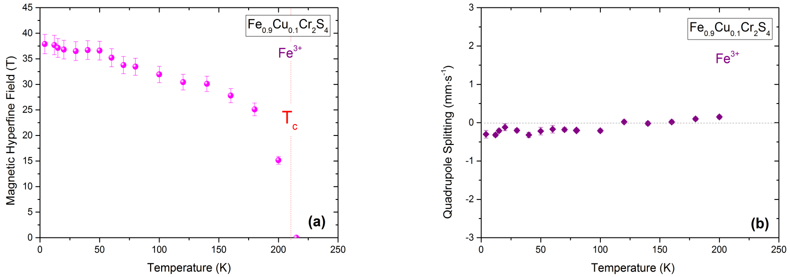

Figure 5.14: Temperature dependence of (a) the magnetic hyperfine field (b) the quadrupole splitting of Fe^{3+} spectrum in $Fe_{0.9}Cu_{0.1}Cr_2S_4$ (x = 0.1). Observed anomalies in low temperature have been not taken in serious due to low contribution of this site (around 6%).

The quadrupole splitting of group I (Fig. 5.13b) rises continuously to about 1 mm $\cdot$ s^{-1} at T_m^{ME} = 80 K, for group II (Fig. 5.13b) it is nearly zero. At the magnetic transition T_c also spectrum X splits into six lines and the magnetic hyperfine field goes up from zero to around 29 T at 80 K continuously. The quadrupole splitting of this site goes down to -0.83 mm $\cdot$ s^{-1} at 100 K.

The EFG detected for group I is interpreted with a magnetically induced EFG as seen already for $x = 0$ (section 4.3).

T (K)	group of spectra	CS ($\mathrm{mm \cdot s^{-1}}$)	QS ($\mathrm{mm \cdot s^{-1}}$)	B_{hf} (T)	Area (%)
200	group I	0.621(4)	-0.003(2)	8.51(2)	50(2)
	group II	0.635(4)	0.122(3)	11.03(3)	36(1)
	spectrum X	0.455(3)	-0.002(2)	13.51(4)	8(1)
	Fe^{3+}	0.26(3)	0.15(5)	15.16(3)	6(2)
180	group I	0.656(6)	0.080(3)	13.64(2)	52(2)
	group II	0.602(3)	-0.068(2)	17.93(3)	33(3)
	spectrum X	0.460(2)	-0.0030(3)	18.70(3)	8(1)
	Fe^{3+}	0.27(2)	0.11(3)	25.1(2)	6(1)
160	group I	0.635(3)	0.181(5)	16.85(1)	51(2)
	group II	0.632(1)	-0.019(2)	20.25(3)	36(3)
	spectrum X	0.471(1)	-0.531(2)	22.01(2)	8(1)
	Fe^{3+}	0.285(2)	0.02(1)	27.80(3)	6(1)
140	group I	0.642(1)	0.342(3)	18.92(3)	49(2)
	group II	0.645(6)	-0.037(3)	22.74(2)	39(3)
	spectrum X	0.485(3)	-0.530(3)	24.80(2)	8(1)
	Fe^{3+}	0.294(4)	-0.02(3)	30.10(4)	6(1)
120	group I	0.649(1)	0.521(3)	19.91(3)	43(2)
	group II	0.666(1)	0.021(1)	24.04(2)	43(3)
	spectrum X	0.505(4)	-0.560(5)	26.40(3)	8(1)
	Fe^{3+}	0.31(2)	0.02(1)	30.43(2)	6(1)
100	group I	0.675(1)	0.653(4)	20.74(1)	45(2)
	group II	0.681(3)	0.060(2)	25.60(4)	42(1)
	spectrum X	0.512(2)	-0.741(3)	27.34(3)	8(1)
	Fe^{3+}	0.301(2)	-0.210(4)	31.94(2)	6(1)
80	group I	0.756(2)	1.06(2)	20.38(2)	50(2)
	group II	0.646(3)	0.131(3)	26.40(3)	36(1)
	spectrum X	0.521(3)	-0.830(2)	28.65(2)	8(1)
	Fe^{3+}	0.31(3)	-0.20(3)	33.46(4)	6(2)

Table 5.2: Adjusted parameter from some selected Mössbauer spectra of $Fe_{0.9}Cu_{0.1}Cr_2S_4$ in the temperature region between the T_c and 80 K.

Region between 80 K and 40 K

Below T_m^{ME} = 80 K we find a significant rise in the quadrupole splitting of group I (see Fig. 5.13b). The magnetic hyperfine fields for group I and II start to show an anomalous behavior; one is decreasing, the other increasing below T_m^{ME} = 80 K. Table 5.3 presents some values from the adjusted spectra in this temperature region.

T (K)	group of spectra	CS $(\mathrm{mm \cdot s^{-1}})$	QS $(\mathrm{mm \cdot s^{-1}})$	B_{hf} (T)	Area (%)
70	group I	0.741(2)	1.135(4)	20.19(4)	48(2)
	group II	0.639(4)	0.157(2)	26.99(1)	39(1)
	spectrum X	0.530(1)	-0.720(4)	29.60(3)	8(1)
	Fe^{3+}	0.33(2)	-0.18(1)	33.77(2)	6(2)
60	group I	0.741(3)	1.137(2)	19.98(2)	50(2)
	group II	0.682(1)	0.023(3)	27.90(3)	36(1)
	spectrum X	0.540(3)	-0.710(2)	31.50(2)	8(1)
	Fe^{3+}	0.32(4)	-0.17(3)	35.20(3)	6(2)
50	group I	0.738(5)	1.32(3)	20.15(3)	55(2)
	group II	0.695(1)	0.026(3)	28.70(5)	32(1)
	spectrum X	0.550(5)	-0.750(4)	32.55(1)	8(1)
	Fe^{3+}	0.328(2)	-0.22(3)	36.60(1)	6(2)
40	group I	0.735(3)	1.566(2)	18.95(3)	52(2)
	group II	0.722(2)	0.024(2)	29.40(4)	34(1)
	spectrum X	0.553(3)	-0.80(3)	32.70(5)	8(1)
	Fe^{3+}	0.369(2)	-0.320(4)	36.70(2)	6(2)

Table 5.3: Adjusted parameter from some selected Mössbauer spectra of $Fe_{0.9}Cu_{0.1}Cr_2S_4$ in the temperature region between 80 K and 40 K.

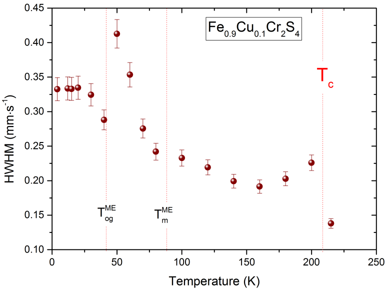

Figure 5.15: Temperature dependence of the average value of the line width of $Fe_{0.9}Cu_{0.1}Cr_2S_4$ ($x = 0.1$) taken from Mössbauer evaluation.

Also in this temperature region the asymmetry parameter η of the electric field gradient EFG is zero. V_{zz} of the induced EFG is positive and quadrupole splitting reaches 1.57 $\mathrm{mm} \cdot \mathrm{s}^{-1}$ at 40 K. The principle z axis of the EFG is collinear to the direction of B_{hf} (i.e. the polar and azimuthal angles in the hyperfine Hamiltonian are $\theta = \phi = 0$).
Furthermore, in this region there can be seen an enhanced distribution of fields and EFGs at Fe^{2+} indicated by an increase of line width when temperature is lowered (see Fig. 5.15). It becomes more apparent around 60 K and reaches a maximum around 50 K. Broad lines may be an indicator for the onset of dynamic or static fluctuations of the magnetic or electric hyperfine fields. Similar behavior was also seen in the Mössbauer study of $FeCr_2S_4$ by Engelke [2010]. It can be related to an anomaly in the atomic displacement parameter in the same temperature region as found by Tsurkan et al. [2010] (see Fig. 4.22). As for $x = 0$ we relate this to the onset of a dynamical Jahn-Teller distortion.
The site attributed to Fe^{3+} does not show any irregularities in this temperature range except of a small jump of quadrupole splitting which is negligible for such a small contribution. The magnetic hyperfine field from spectrum X (a low excess of iron in octahedral sites) shows step-like increasing while the EFG is nearly flat (around $-0.8\ \mathrm{mm} \cdot \mathrm{s}^{-1}$) in this temperature regime.

Temperatures below 40 K

One can clearly observe that below $T_{og}^{ME} = 40$ K significant changes occur in the shape of spectra. This can be directly seen when comparing the spectra taken at 40 K and 4 K in Fig. 5.11. These changes are mainly caused by the three subspectra of group I. In contrast to higher temperatures we now find a clear rotation of V_{zz} by $\theta \simeq 85 \pm 5°$ with respect to the direction of B_{hf} for this group. V_{zz} becomes negative, in additional the asymmetry parameter η is non-zero with an azimuthal angle $\phi \simeq 45 \pm 8°$. Also B_{hf} shows distinct changes in this temperature range (see Fig. 5.13a). Especially for spectral group I we find a decrease upon lowering temperature similar to that found for $x = 0$. The value of η is about 0.5 which is higher than the value seen for $x = 0$ by about ~ 0.2 (Engelke et al. [2011]).
Most significant is a jump of $e^2qQ/2$ of group I from a positive value of about 1.5 $\mathrm{mm} \cdot \mathrm{s}^{-1}$ at around 40 K to a negative value of approximately $-2.8\ \mathrm{mm} \cdot \mathrm{s}^{-1}$ (roughly double values).

T (K)	group of spectra	CS ($\mathrm{mm \cdot s^{-1}}$)	QS ($\mathrm{mm \cdot s^{-1}}$)	B_{hf} (T)	η	θ (°)	ϕ (°)	Area (%)
30	group I	0.732(8)	-2.625(6)	16.89(6)	0.38(4)	85.3(1)	39.3(1)	54(2)
	group II	0.730(6)	-0.024(5)	30.41(4)	-	-	-	31(1)
	spectrum X	0.572(3)	-1.20(2)	32.34(2)	-	-	-	8(1)
	Fe^{3+}	0.332(4)	-0.21(1)	36.50(2)	-	-	-	6(2)
20	group I	0.714(8)	-2.773(1)	15.65(3)	0.46(1)	86.6(2)	50.2(1)	52(2)
	group II	0.699(9)	-0.0798(9)	31.88(2)	-	-	-	34(1)
	spectrum X	0.579(1)	-1.60(5)	37.10(1)	-	-	-	8(1)
	Fe^{3+}	0.331(2)	-0.12(3)	36.80(3)	-	-	-	6(2)
15	group I	0.755(3)	-2.714(3)	15.91(3)	0.51(2)	85.4(2)	54.5(2)	54(2)
	group II	0.682(2)	-0.153(9)	32.08(2)	-	-	-	32(1)
	spectrum X	0.586(3)	-1.84(3)	40.24(2)	-	-	-	8(1)
	Fe^{3+}	0.319(3)	-0.21(2)	37.12(2)	-	-	-	6(2)
12	group I	0.737(0)	-2.730(6)	15.61(3)	0.45(3)	85.5(2)	45(1)	54(2)
	group II	0.673(8)	-0.267(8)	32.16(7)	-	-	-	33(1)
	spectrum X	0.592(3)	-1.93(5)	40.89(2)	-	-	-	8(1)
	Fe^{3+}	0.315(2)	-0.32(1)	37.70(1)	-	-	-	6(2)
4	group I	0.704(0)	-2.514(2)	14.88(7)	0.56(2)	84.4(2)	50.2(3)	52(2)
	group II	0.686(1)	-0.258(2)	32.07(7)	-	-	-	33(1)
	spectrum X	0.585(4)	-2.13(4)	41.10(2)	-	-	-	8(1)
	Fe^{3+}	0.308(2)	-0.30(1)	37.88(3)	-	-	-	6(2)

Table 5.4: Adjusted parameter from some selected Mössbauer spectra of $Fe_{0.9}Cu_{0.1}Cr_2S_4$ for temperatures below 40 K.

For a closer inspection we have plotted in table 5.4 the parameters taken from the hyperfine Hamiltonian analysis. The EFG for group II does not vary significantly. But the magnetic hyperfine field is increasing while it is decreasing for group I. The spectrum X shows notable changes in EFG similar to group I yet weaker. B_{hf} increases step-like below 30 K.

5.3.1.2

$Fe_{0.8}Cu_{0.2}Cr_2S_4$

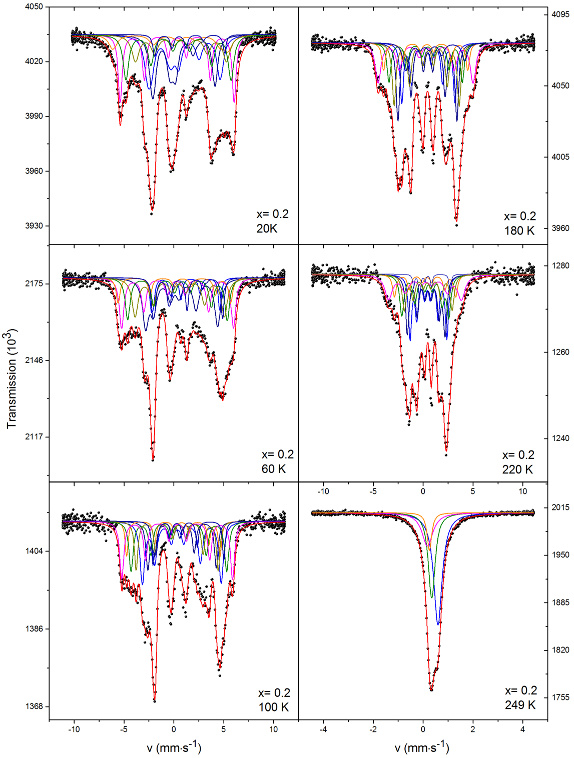

Figure 5.16: Mössbauer spectra of the $Fe_{0.8}Cu_{0.2}Cr_2S_4$ ($x = 0.2$) at various temperatures. The experimental points are shown as black dots, fitted by the red solid line (total signal). The total signal is decomposed into seven distinct contributions.

Fig. 5.16 (for a complete compilation, see appendix A.2) shows the spectra of $Fe_{0.8}Cu_{0.2}Cr_2S_4$ between 4 K and 249 K in different temperature regimes. The strategy for fitting is identical to that applied for $x = 0.1$ and the temperature dependence of hyperfine parameters is close to that of $x = 0.1$ (see Fig. 5.18 and table in A.2).

Obtained center shift values of evaluation of all spectra have been presented in Fig. 5.17 which indicate the different oxidation states of Fe^{2+} and Fe^{3+}.

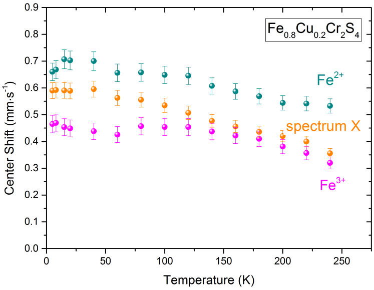

Figure 5.17: Temperature dependence of the center shift of $Fe_{0.8}Cu_{0.2}Cr_2S_4$ (x = 0.2) taken from Mössbauer evaluation.

Paramagnetic Regime above 248 K

The magnetic transition temperature T_c for x = 0.2 is now 248 K (see Fig. 5.18a). The paramagnetic Mössbauer spectrum at 249 K in Fig. 5.16 has been fitted with four sites: two for Fe^{2+}, one Fe^{3+}, and spectrum X. Comparing to concentration x = 0.1, the lines are sharper due to a higher contribution by Fe^{3+}. Table 5.5 gives the values of hyperfine parameters at 249 K.

T (K)	Assignment	CS (mm · s^{-1})	QS (mm · s^{-1})	HWHM (mm · s^{-1})	Area (%)
249	Fe^{2+}	0.701(3)	0.004	0.21(3)	46(2)
	Fe^{2+}	0.452(4)	0.062(1)	0.16(3)	28(3)
	Fe^{3+}	0.28(3)	0.01(3)	0.26(5)	18(3)
	spectrum X	0.36(3)	0.0001	0.11(1)	8(1)

Table 5.5: Adjusted parameter from Mössbauer spectra of $Fe_{0.8}Cu_{0.2}Cr_2S_4$ at 249 K in paramagnetic regime.

Region between 249 K and 100 K

At T_m^{ME} = 100 K $\leqslant$ T $<$ T_c, the magnetic hyperfine field starts increasing below the ordering temperature and appears to follow normal magnetization curve for all sites contributing to the fit as shown in Fig. 5.18a and Fig. 5.19a. As plotted in Fig. 5.18b and Fig. 5.19b, the quadrupole splitting for all sites are small yet gradually increasing upon lowering temperature for group I and spectrum X. This EFG is again induced by magnetic order. The line width of Fe^{2+} shows no anomaly in this temperature range, while Fe^{3+} line width is increasing up to T_c as seen also for x = 0.1 (Fig. 5.20).

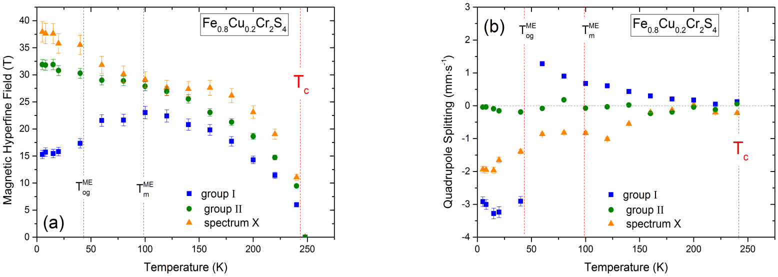

Figure 5.18: Temperature dependence of: (a) the magnetic hyperfine field; (b) the quadrupole splitting in $Fe_{0.8}Cu_{0.2}Cr_2S_4$.

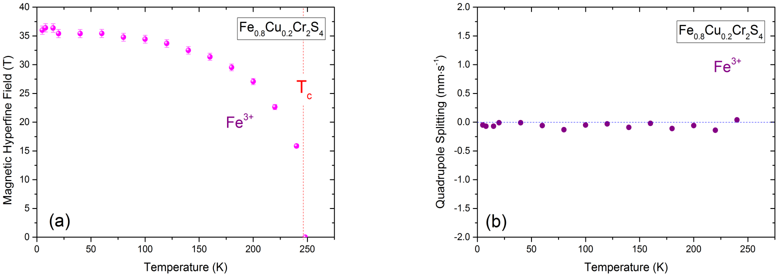

Figure 5.19: Variation of the magnetic hyperfine field and quadrupole splitting of Fe^{3+} with temperature in $Fe_{0.8}Cu_{0.2}Cr_2S_4$ ($x = 0.2$).

Region between 100 K and 60 K

Fig. 5.18 indicates significant changes in magnetic hyperfine fields and even more visible for quadrupole splitting. The induced quadrupole splitting is growing down to around $T^{ME}_{og} = 60$ K with positive V_{zz}. The magnetic hyperfine for group I starts decreasing below $T^{ME}_{m} = 100$ K (Fig. 5.18a). Fig. 5.20 shows an increase of the line width with decreasing temperature indicating an enhanced distribution of fields and EFGs at Fe^{2+} as seen also for $x = 0.1$. The site attributed to Fe^{3+} does not show any anomaly in this temperature range.

Temperatures below 60 K

The evaluation of spectra below 80 K establishes that the electronic state of the Fe^{2+} ions on the tetrahedral A sites undergoes a transition around $T^{ME}_{og} = 60$ K that results in an angle

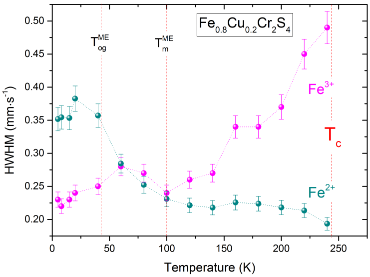

Figure 5.20: Temperature dependence of the average value of the line width for Fe^{2+} and Fe^{3+} sites of $Fe_{0.8}Cu_{0.2}Cr_2S_4$ ($x = 0.2$) taken from Mössbauer evaluation.

between the principle axis z of the electric field gradient and the magnetic hyperfine field changing from a higher temperature value of $\theta = 0°$ to a low temperature value of $\theta = 90°$. Also the asymmetry parameter η is no more zero and is increasing for lower temperature (see table A.3 in appendix A.2).

5.3.1.3

$Fe_{0.7}Cu_{0.3}Cr_2S_4$

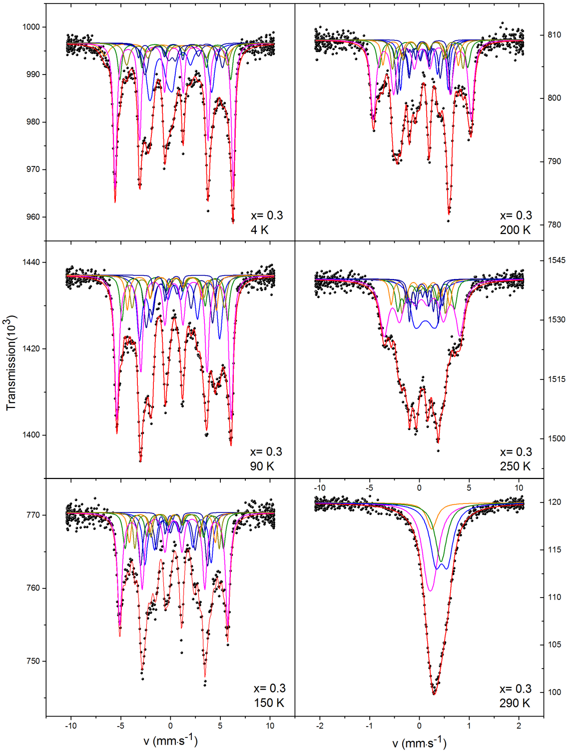

Figure 5.21: Mössbauer spectra of the $Fe_{0.7}Cu_{0.3}Cr_2S_4$ ($x = 0.3$) at various temperatures. The experimental points are shown as black dots, fitted by the red solid line (total signal).

Fig. 5.21 shows some selected spectra chosen between 4 K and room temperature (see Fig. A.6 in appendix). One can observe that lines are getting sharper with increasing Cu amount. The quantity of spectral area of Fe^{2+} is decreased upon adding more copper. Generally, the hyperfine parameters behave as seen for $x = 0.1$ and $x = 0.2$.

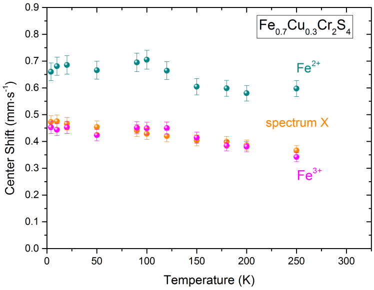

Figure 5.22: Temperature dependence of the center shift of $Fe_{0.7}Cu_{0.3}Cr_2S_4$ ($x = 0.3$) taken from Mössbauer evaluation.

Fitting strategy was again the same as for $x = 0.1$ and $x = 0.2$. Center shifts are plotted in Fig. 5.22, the magnetic hyperfine fields and quadrupole splitting in Figs. 5.23 and 5.24 (see also table in appendix A.3). The onset of magnetic hyperfine field is around $T_c = 289$ K.

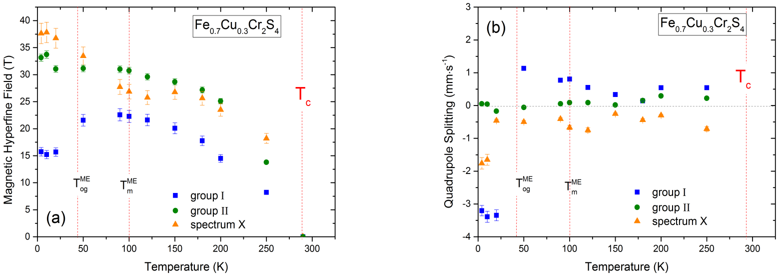

Figure 5.23: Temperature dependence of: (a) the magnetic hyperfine field; (b) the quadrupole splitting in $Fe_{0.7}Cu_{0.3}Cr_2S_4$.

Fe^{2+} subspectra which are attributed to group I and group II show analogous changes in magnetic hyperfine fields, quadrupole splitting and asymmetry parameter η as found for $x = 0.1$ and $x = 0.2$. The temperature regimes for these are indicated with red-dashed lines. The Fe^{3+} spectrum (Fig. 5.24) appears to have normal behavior with nearly zero quadrupole splitting.

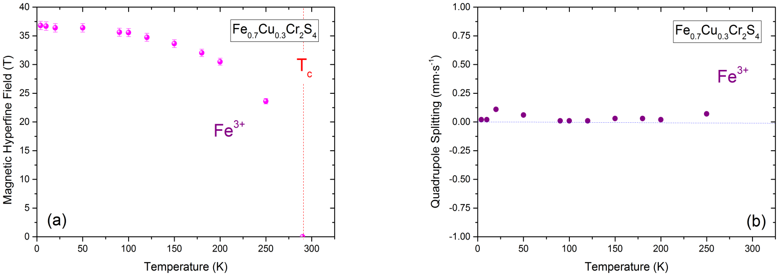

Figure 5.24: Variation of the magnetic hyperfine field and quadrupole splitting of Fe^{3+} with temperature in $\mathrm{Fe_{0.7}Cu_{0.3}Cr_2S_4}$ ($x = 0.3$).

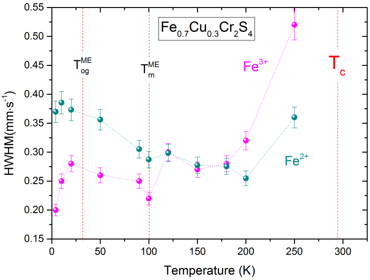

Figure 5.25: Temperature dependence of the average value of the line width of $\mathrm{Fe_{0.7}Cu_{0.3}Cr_2S_4}$ ($x = 0.3$) taken from Mössbauer evaluation.

Fig. 5.25 displays the average line width of all subspectra for $\mathrm{Fe^{2+}}$ and $\mathrm{Fe^{3+}}$. It is rising for $\mathrm{Fe^{3+}}$ an approaching T_c. Below 100 K when decreasing temperature the spectra of $\mathrm{Fe^{2+}}$ are getting broader.

5.3.1.4

$Fe_{0.6}Cu_{0.4}Cr_2S_4$

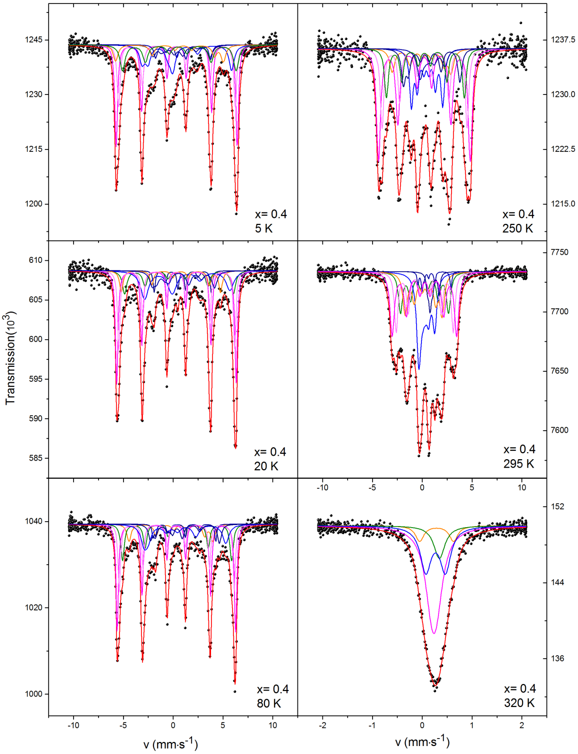

Figure 5.26: Mössbauer spectra of the $Fe_{0.6}Cu_{0.4}Cr_2S_4$ ($x = 0.4$) at various temperatures. The experimental points are shown as black dots, fitted by the red solid line (total signal).

Fig. 5.26 displays selected Mössbauer spectra at various temperatures of the compound with $x = 0.4$. Each of them consists of seven sextet components (also see appendix A.4). Above 313 K the compound is paramagnetic. The difference between this concentration with other ones is that the contribution of Fe^{3+} is much bigger and was fitted by two Fe^{3+} components (pink outer lines). The sextets belonging to Fe^{3+} sites and that belonging to Fe^{2+} sites can be clearly distinguished on the basis of the considerably different hyperfine magnetic fields (~ 37 T vs. ~ 15 K at 5 K), different center shift for those components having the same range of hyperfine field (ascribed to non-distorted sites by Cu doping (group II)) which they reflect.

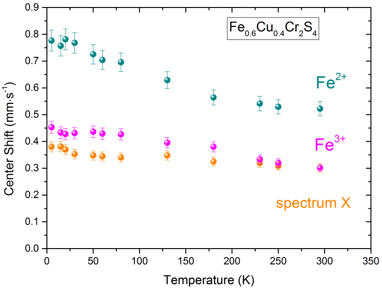

Figure 5.27: Temperature dependence of the center shift of $Fe_{0.6}Cu_{0.4}Cr_2S_4$ ($x = 0.4$) taken from Mössbauer evaluation.

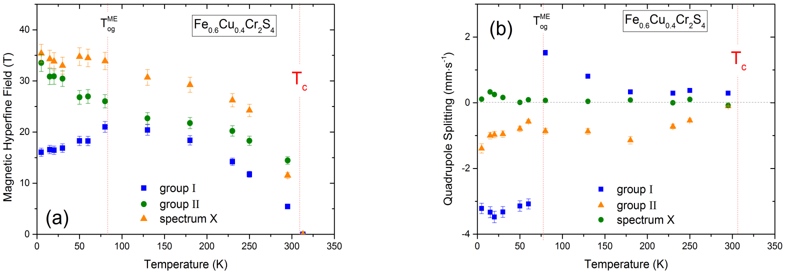

Figure 5.28: Temperature dependence of: (a) the magnetic hyperfine field; (b) the quadrupole splitting in $Fe_{0.6}Cu_{0.4}Cr_2S_4$.

Fig. 5.27 shows the temperature dependent center shift of the different oxidation states, the Fe^{2+} and Fe^{3+} center shift are average of four and two components, respectively. Interestingly, the center shift of spectrum X is getting smaller by adding more copper for $x = 0.4$ it is around 0.36 $mm \cdot s^{-1}$ for $x = 0.4$, while for $x = 0.1$ it is about 0.55 $mm \cdot s^{-1}$.

Figures shown in 5.28 and 5.29, present the temperature dependence of magnetic hyperfine fields and quadrupole splittings for all group of spectra. In Fig. 5.28, the magnetic hyperfine field and quadrupole splitting of group I show changes around $T_m^{ME} = 80$ K as seen for $x = 0.1, 0.2, 0.3$. The quadrupole splitting for group II is nearly zero for whole temperature range while its magnetic hyperfine field increases below 80 K. The appearance of positive quadrupole splitting in higher temperatures is again ascribed to magnetically induced EFG. Fig. 5.29 presents the typical temperature dependent B_{hf} for both Fe^{3+} subspectrum.

The average of line width of Fe^{2+} and Fe^{3+} illustrate two distinct areas below 100 K for

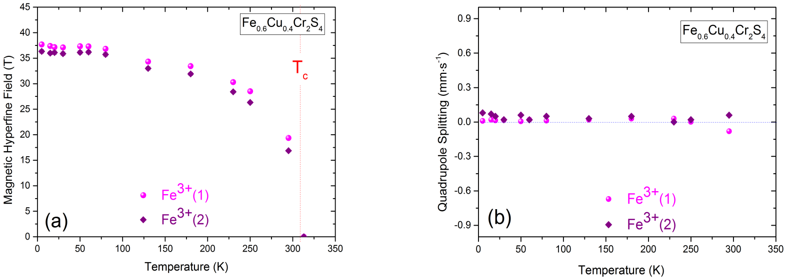

Figure 5.29: Variation of the magnetic hyperfine field and quadrupole splitting of Fe^{3+} with temperature in $Fe_{0.6}Cu_{0.4}Cr_2S_4$ (x = 0.4).

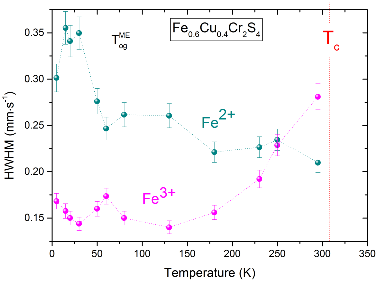

Figure 5.30: Temperature dependence of the average value of the line width of $Fe_{0.6}Cu_{0.4}Cr_2S_4$ (x = 0.4) taken from Mössbauer evaluation.

Fe^{2+} and above 180 K for Fe^{3+} (see Fig. 5.30). Below ~ 100 K, it gradually is increasing for Fe^{2+}, and above ~ 180 K rising sharply for Fe^{3+} to approach T_c.

5.3.2

Mössbauer Results for the $0.5 \leqslant x \leqslant 0.8$ Concentration Region

For all concentrations in this region, the dominant spectral contribution comes from Fe^{3+}. The small contribution ascribed to Fe^{2+} has smaller hyperfine magnetic field with big EFG and the typical large center shift.
This section starts with the interesting concentration x = 0.5. Fig. 5.31 shows the spectra of $Fe_{0.5}Cu_{0.5}Cr_2S_4$ at selected temperatures of interest (see also appendix A.5). In order to achieve a more stable fit of the main magnetic component, the area of the minor magnetic component in middle of spectra was kept fixed for all temperatures. This small area is

indicated by the blue line in the spectra and is attributed to Fe^{2+}. All spectra have been fitted with four components, two Fe^{3+}, and two Fe^{2+}.

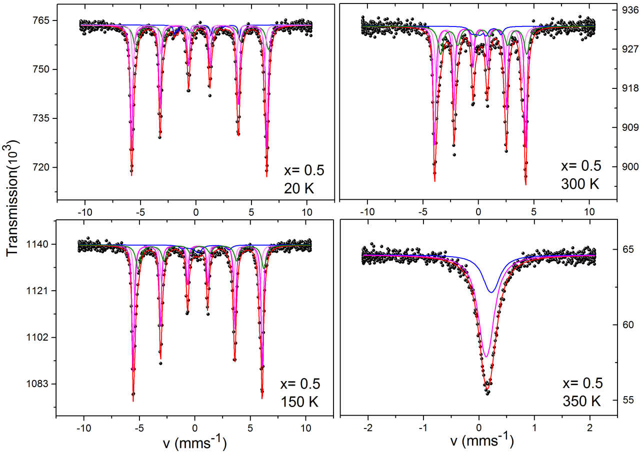

Figure 5.31: Mössbauer spectra of the $Fe_{0.5}Cu_{0.5}Cr_2S_4$ (x = 0.5) at various temperatures.

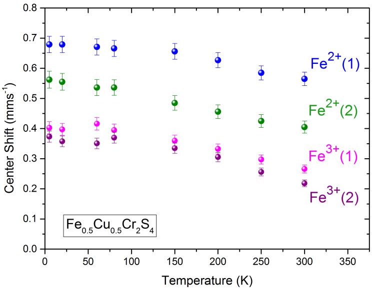

Figure 5.32: Temperature dependence of the center shift of $Fe_{0.5}Cu_{0.5}Cr_2S_4$ (x = 0.5) taken from Mössbauer evaluation.

Figures 5.32, 5.33, and 5.34 present the temperature dependence of center shifts, magnetic hyperfine fields, and quadrupole splittings. The blue points of Fe^{+2} have a center shift $CS = 0.68\ \mathrm{mm \cdot s^{-1}}$ at low temperature, small magnetic hyperfine field and large negative EFG (about 7% of area). These values are representative for iron in the Fe^{2+} oxidation state in the tetrahedral site of $FeCr_2S_4$. Also there is another Fe^{2+} site presented by green points, with high magnetic hyperfine field and smaller center shift (CS = 0.56 mm $\cdot$ s^{-1}) (about 22% of area). This contribution will show up more clearly for still higher copper doping which means the gradual transformation of Fe^{2+} to Fe^{3+}(see below).

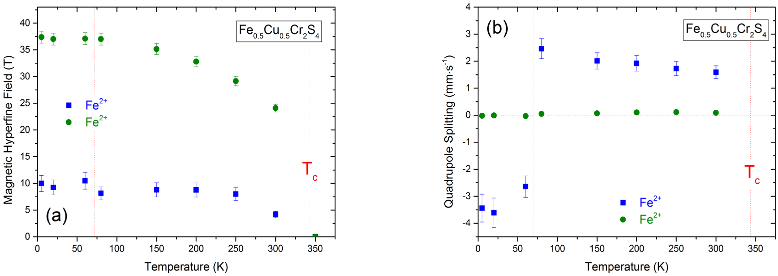

Figure 5.33: Temperature dependence of: (a) the magnetic hyperfine field ; (b) the quadrupole splitting in Fe$_{0.5}$Cu$_{0.5}$Cr$_2$S$_4$.

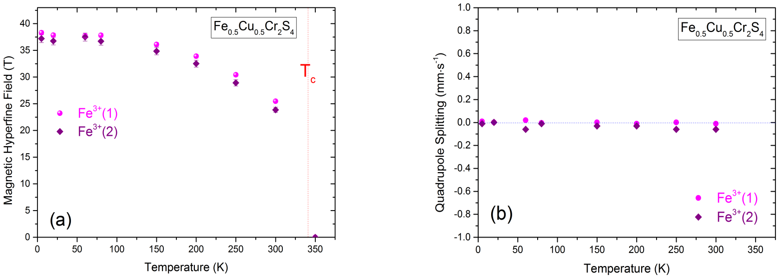

Figure 5.34: Temperature dependence of: (a) magnetic hyperfine field, (b) quadrupole splitting of Fe^{3+} for Fe$_{0.5}$Cu$_{0.5}$Cr$_2$S$_4$ ($x = 0.5$).

The temperature dependence of average linewidth is shown in Fig. 5.35. Lines are narrow and there is only a weak increase with temperature.
Fig. 5.36 demonstrates the Fe$_{0.4}$Cu$_{0.6}$Cr$_2$S$_4$ spectra at various temperatures (see also appendix A.6). The related spectra have been fitted with three subspectra indicating the same behavior of hyperfine parameters as found for Fe$_{0.5}$Cu$_{0.5}$Cr$_2$S$_4$. Only difference is the area contributed to Fe^{2+} sites which decreases upon adding more copper. Figures 5.37, 5.38, and 5.39 show the temperature dependent hyperfine parameters which behave similarly as for $x = 0.5$.

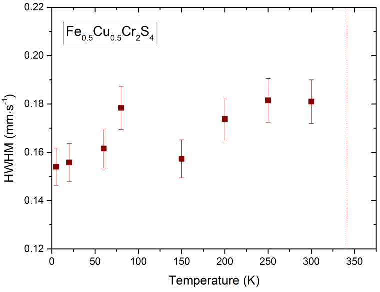

Figure 5.35: Temperature dependence of the average value of the line width of $Fe_{0.5}Cu_{0.5}Cr_2S_4$ (x = 0.5) taken from Mössbauer evaluation.

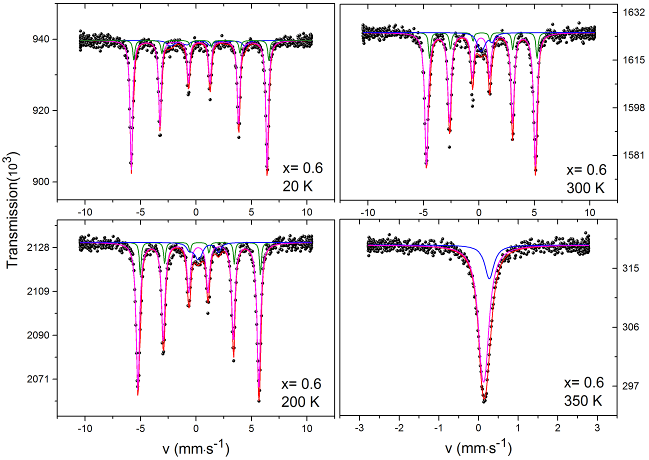

Figure 5.36: Mössbauer spectra of the $Fe_{0.4}Cu_{0.6}Cr_2S_4$ (x = 0.6) at various temperatures.

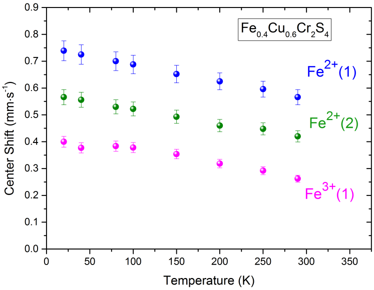

Figure 5.37: Temperature dependence of the center shift of $Fe_{0.4}Cu_{0.6}Cr_2S_4$ ($x = 0.6$) taken from Mössbauer evaluation.

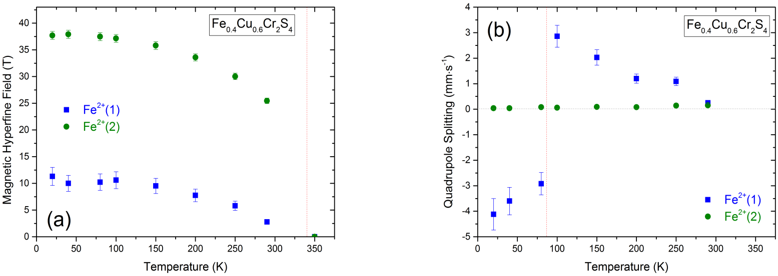

Figure 5.38: Temperature dependence of: (a) the magnetic hyperfine field ; (b) the quadrupole splitting in $Fe_{0.4}Cu_{0.6}Cr_2S_4$.

For higher concentrations $x = 0.7$ and $x = 0.8$, spectra are shown in Figs. 5.40 and 5.41. For fitting we needed three resolved magnetic patterns for Fe^{3+} and an additional weak contribution (about 10% of area) in the center of spectra. Its center shift can not be extracted with sufficient accuracy and is in the range of divalent. Its magnetic splitting is only small for all temperatures. We relate it to small superparamagnetic precipitates. Their contribution can well be traced in the center of the 300 K spectrum for $x = 0.8$ in Fig. 5.41.

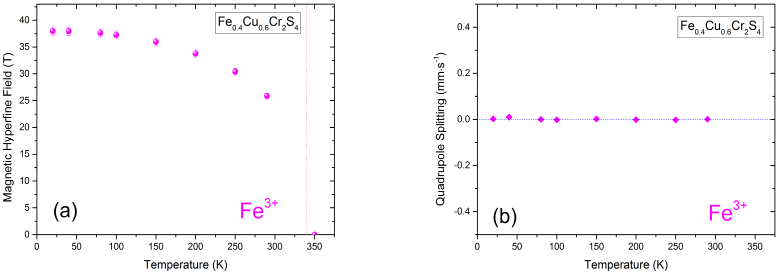

Figure 5.39: Temperature dependence of the: (a) magnetic hyperfine field, (b) quadrupole splitting of Fe^{3+} for $Fe_{0.4}Cu_{0.6}Cr_2S_4$ ($x = 0.6$).

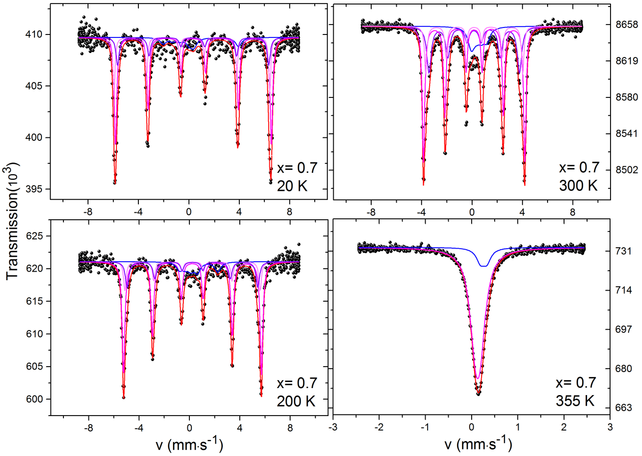

Figure 5.40: Mössbauer spectra of the $Fe_{0.3}Cu_{0.7}Cr_2S_4$ ($x = 0.7$) at various temperatures.

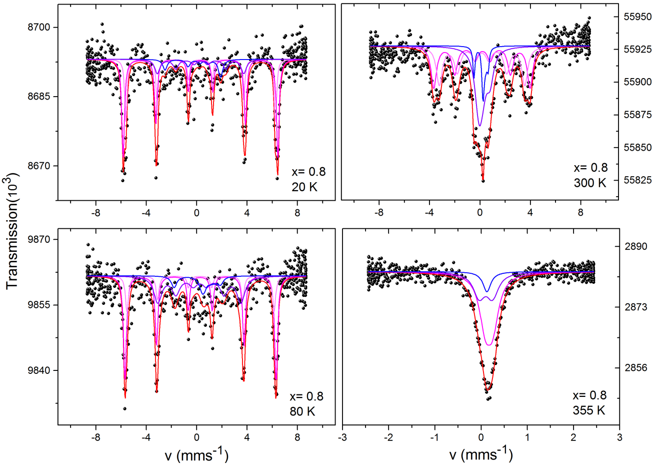

Figure 5.41: Mössbauer spectra of the $Fe_{0.2}Cu_{0.8}Cr_2S_4$ ($x = 0.8$) at various temperatures.

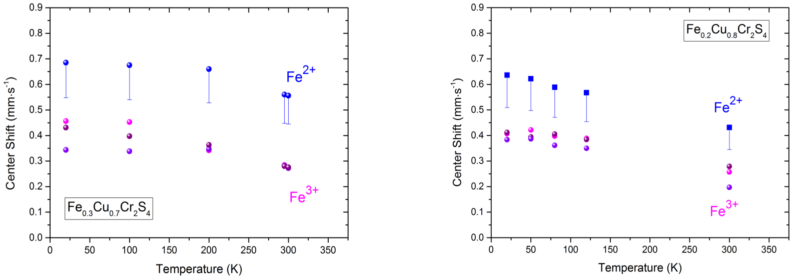

Figure 5.42: Temperature dependence of center shifts of $Fe_{0.3}Cu_{0.7}Cr_2S_4$ (left) and $Fe_{0.2}Cu_{0.8}Cr_2S_4$ (right).

5.4

μSR on $\mathbf{Fe_{1-x}Cu_xCr_2S_4}$

The μSR measurements presented here, were performed on six samples, $x = 0.1, 0.2, 0.3, 0.4, 0.5, 0.6, 0.8$ between 5 K and room temperature[4]. The *musrfit* program developed at PSI was used to fit the μSR data (Suter and Wojek [2011]). Here, we briefly discuss the functions $P(t)$ appearing in this work in order to ease the understanding of the result of μSR analyses.

Transverse field measurements

The TF μSR time spectra were measured in applied field of 3 mT for all concentrations which have the magnetic ordering temperature below room temperature. The goal is to find the α factor (see in equation 3.17), a possible background asymmetry, the initial asymmetry, and the onset of magnetic order. The asymmetry signal was fitted the paramagnetic regime using a cosinusoidal oscillation with damping:

$$P_x^{TF}(t) = \exp(-\lambda_{par} t)\cos(\omega_\mu t) \tag{5.1}$$

$\omega_\mu = \gamma_\mu B_\mu$ where B_μ is essentially the applied field. The relaxation rate $\lambda_{par} = \gamma_\mu^2 \langle B_\mu^2 \rangle \tau_S$ depends on the width of the distribution of B_μ characterized by its second moment (static distribution) and the spin fluctuation rate $1/\tau_s$. The oscillatory pattern has the intensity A_0 denoted as full asymmetry for temperature far above T$_c$. On approaching to T$_c$ from above, λ_{par} increases sharply indicating the magnetic transition point. Below T$_c$ the rotating asymmetry in a polycrystal is lost due to the randomly oriented superposition of strong local fields in the ordered state with the smaller applied field.

Zero field measurements

Below T$_c$, in long-range magnetic order, all samples with different Cu concentration exhibit a spin precession pattern in the initial part of the spectrum in high time resolution ZF data. The spectrum could be easily fitted to a relaxation function (as previous work done by Kalvius et al. [2013]):

$$P_z^{osc}(t) = \frac{1}{3}\exp(-\lambda_{long} t) + \frac{2}{3}\exp(-\lambda_{trans} t)\cos(\omega_\mu t) \tag{5.2}$$

where the first term does not exhibit a Larmor precession since for the 1/3 of all cases the field is oriented parallel to the muon spin initial polarization (longitudinal term). The longitudinal relaxation λ_{long} is caused exclusively by fluctuations of the electronic spin (dynamics of the magnetic moments). In the static limit λ_{long} is equal zero.

The oscillatory second term arises from the muon spin precession around the perpendicular oriented local field components. The transverse relaxation λ_{trans} is caused by a distribution of the local field around its mean value.

---

[4] data $x = 0.2, 0.5, 0.8$ were collected by Kalvius et al. [2013] and were re-analyzed here.

Although this relaxation function could properly cover the oscillating part of the spectra, firstly it could not catch the full asymmetry at early times and secondly it could not satisfactorily describe the damping extending to high times, i.e. the longitudinal relaxation appearing at higher temperatures. We therefore had to introduce two different relaxation functions for the lower and the higher temperature range. Below a certain T_p, a fast relaxing component is resolved with a sizable relaxation rate which is oscillating, resulting from the muon ensemble experiencing a broad distribution of large and slowly fluctuating magnetic fields. Its development coincides with a loss of asymmetry in the amplitude of a non-relaxing (or, more likely, very slowly relaxing) component. However, the total observed asymmetry is reduced compared to its value in the paramagnetic regime. Therefore, there is a combination of both static and dynamic contributions.

The dynamic part can well be described by a dynamical Lorentzian Kubo-Toyabe function throughout the covered temperature range below T_p and the static part can be fitted by the simple oscillatory pattern when λ_{long} is zero and presented in eq. 5.2.

Thus, the ZF asymmetry spectra below T_p could be fitted to a relaxation function;

$$P_z^L(t) = A_{osc}P_z^{osc}(t) + A_{KT}P_{DKTF}(t) \tag{5.3}$$

The $musrfit$ program of dynamic Kubo-Toyabe function (DLKT) developed at PSI and also introduced in equation 3.33 has 4 parameters; ν represents a "*hop rate*" (corresponds to a field fluctuation rate) of muons in the sample, a is the width of a Gaussian damping of the signal, v is a frequency which is proportional to an applied longitudinal field that is zero in our measurements. The last parameter is the asymmetry.

Above T_p, The ZF data could be fitted to a relaxation function

$$P_z^H(t) = A_{osc}P_{osc}(t) + A_{rlx}P_{rlx}(t) \tag{5.4}$$

where

$$P_{osc}(t) = A_{osc}\exp(-\lambda_{osc}t)\cos(\omega_\mu t) \tag{5.5}$$

and

$$P_{rlx}(t) = A_f\exp(-\lambda_f t) + A_s\exp(-\lambda_s t) \tag{5.6}$$

corresponding to oscillating and relaxing terms. $A_{f,s}$ and $\lambda_{f,s}$ are the asymmetry and relaxation rates of a fast and a slow exponentially damped components. Note that λ_f represents relaxation due to fast dynamics and hence slow fluctuation of local field (caused by near by ionic moments). This relaxation function was used by Heffner et al. [2000] to analyze ZF data of CMR material $La_{0.67}Ca_{0.33}MnO_3$. There the fluctuations were caused by Mn ion moments.

In the following section, the experimental results of the μSR investigation of the mentioned copper concentration are presented. In total, the samples $x = 0.1, 0.2, 0.3, 0.4$ behave very similar.

5.4.1

$Fe_{0.9}Cu_{0.1}Cr_2S_4$

Typical transverse field μ^+SR spectra measured above and below the magnetic transition temperature T_c for concentration $x = 0.1$ are shown in Fig. 5.43. The 220 K spectrum is typical for a paramagnet, whose spectral function follows the equation 5.1. The increase in damping upon entering a magnetically ordered phase is evident from spectra at 212 K and 213 K. The initial asymmetry is about 0.245.

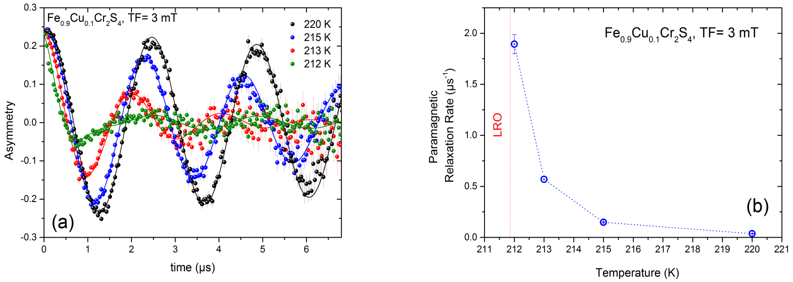

Figure 5.43: (a) TF = 3 mT spectra of $Fe_{0.9}Cu_{0.1}Cr_2S_4$ in paramagnetic phase. (b) The temperature dependence of the paramagnetic relaxation rate (the lines are guides to the eye).

The ZF μSR measurements carried out between 5 K and 200 K show a clear oscillation in the early times part of the spectra that proves a magnetically ordered state (Fig. 5.44). There are two distinct temperature regions: $T \lesssim T_p = 100\ K$ can be well described by the formalism of eq. 5.3. In the second temperature region (above 100 K), the amplitude of the oscillatory component decreases and a relaxation component appears with a slow and a fast decay rate that can be well fitted by eq. 5.4.

In order to follow this change, the development of the asymmetry parameters for the oscillation and the relaxation parts are shown in Fig. 5.45. The fact that the asymmetry amplitude is shared between two signals ($osc + DLKT$) below T_p and three signals ($osc + rlx$) above T_p is evidence that the muons are stopping in different kinds of magnetic environment. The asymmetry of the oscillating part below T_p grows steadily in amplitude with increasing temperature, while the dynamic part, corresponding to the asymmetry of dynamical Kubo-Toyabe, is nearly constant at the lowest temperatures, but decreases as temperature is raised further and vanishes below T_p. Above T_p, the oscillating asymmetry is constant and fixed. A_f decreases while A_s increases, when approaching T_c.

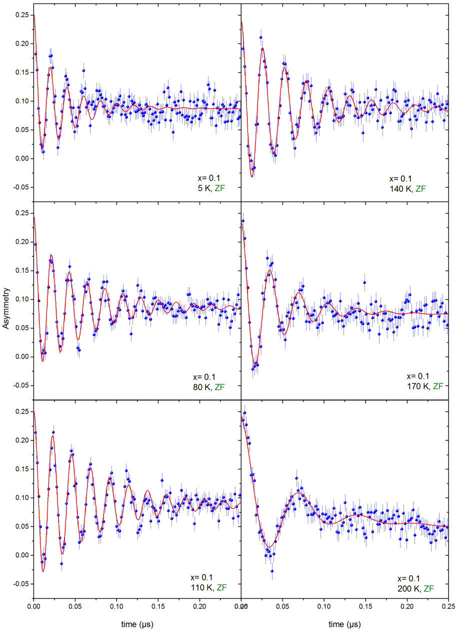

Figure 5.44: Zero field μSR spectra of the $Fe_{0.9}Cu_{0.1}Cr_2S_4$ ($x = 0.1$) at selected temperatures. Shown is the initial part of the spectra. The solid lines are the least square fit to the relaxation function described in equations 5.3 and 5.4.

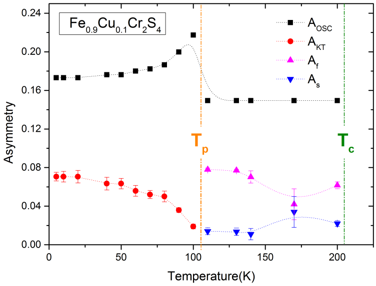

Figure 5.45: Temperature dependence of the asymmetry parameters for each of the four components used in the fits for $Fe_{0.9}Cu_{0.1}Cr_2S_4$. The dashed lines are guides for the eye. The vertical dashed lines indicate the position of T_p and T_c.

In Fig. 5.46b, the Fourier power plots of the high temperature spectra show relatively sharp and high peaks. As the temperature decreases, below 100 K the peak height gradually decreases. The muon precession frequencies from the fit of time spectra increases from 14 MHz at 200 K to 49.7 MHz at 5 K. Its temperature dependence is plotted in Fig. 5.46a. The oscillations develop below T_c = 210 ± 1 K and saturate around 50 MHz at low temperature. Only one muon precession frequency is observed at all measured temperatures, strongly suggesting that there is a single set of the equivalent muon sites in the structure. Note that both the A tetrahedral and the B octahedral sublattices order at the same temperature.

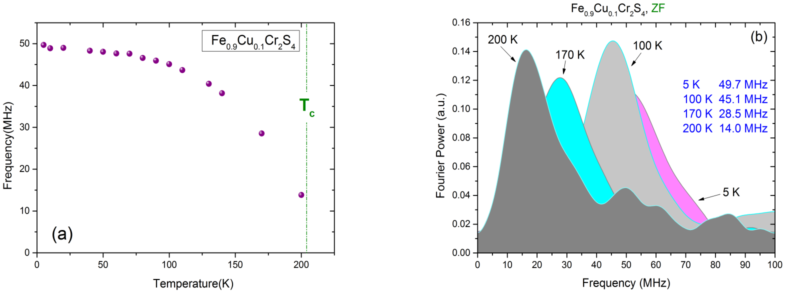

Figure 5.46: (a) Temperature dependence of the muon precession frequency. (b) Fast Fourier transform of the selected spectra at various temperatures for $Fe_{0.9}Cu_{0.1}Cr_2S_4$.

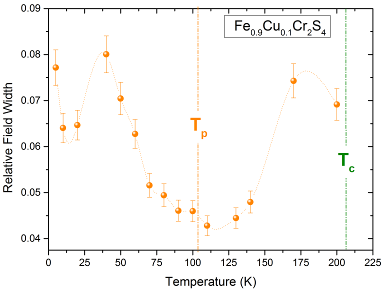

Figure 5.47: Dependence on the temperature of the relative field distribution width $\Delta B_\mu / B_\mu^0$ for $Fe_{0.9}Cu_{0.1}Cr_2S_4$.

Fig. 5.47 demonstrates the unusual variations with temperature of the relative field width $\Delta B_\mu / B_\mu^0$ derived from λ_{trans}. One notices immediately just by looking at the spectra shown in Fig. 5.44, that the damping of the spin precession pattern (oscillating part) is high at low temperatures, but decreases substantially, if the temperature is raised up to $T_p \sim 100$ K. There is a clear peak in the relative field width $(\Delta B_\mu/B_\mu^0)$ around 40 K. Both the peak and the following decrease of $\Delta B_\mu/B_\mu^0$ resemble clearly the temperature dependence of the Mössbauer line width shown in Fig. 5.15 and therefore should be related to a static field distribution varying with temperature.

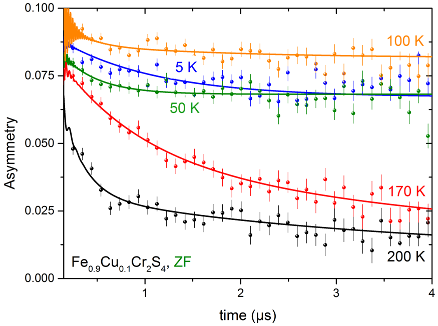

Figure 5.48: ZF spectra of $Fe_{0.9}Cu_{0.1}Cr_2S_4$ at selected temperatures within the long range magnetically ordered regime in low time resolution where only the longitudinal relaxation appears.

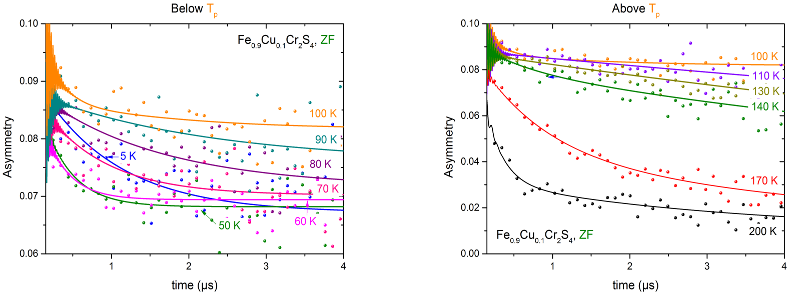

Figure 5.49: Early times of ZF spectra of $Fe_{0.9}Cu_{0.1}Cr_2S_4$ at various temperatures within the long range magnetically ordered regime below and above T_p (left and right panel, respectively).

As mentioned already, the role of dynamic Kubo-Toyabe function can be seen in the full spectral time range plotted in low time resolution. Figs. 5.48 and 5.49 display the ZF muon depolarization at representative temperatures. Fig. 5.49 shows two temperature regions below $T_p \sim 100$ K and above.

Below $T_p \sim 100$ K where the spectra are fitted with DLKT, Fig. 5.49 exhibits a continuous change of the relaxation rate. The relaxation rate rises continuously down to around 80 K. Below this temperature the very early part of the DLKT relaxation cannot be resolved. To get the proper parameters in the fits of the low temperature data, the initial asymmetry was kept fixed to the value obtained in free fits at high temperature.

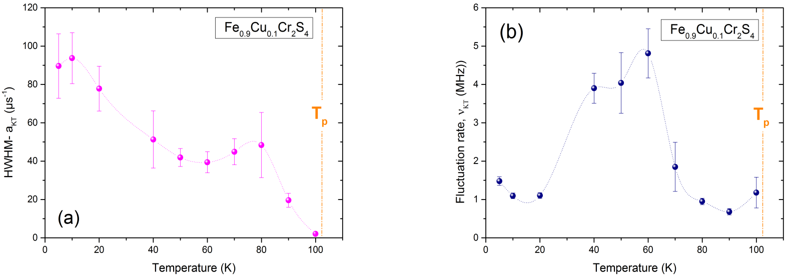

Figure 5.50: Temperature dependence of: (a) width a_{KT}; (b) fluctuation rate ν_{KT} derived from dynamical Kubo-Toyabe function DLKT fits to ZF data for $Fe_{0.9}Cu_{0.1}Cr_2S_4$. The lines are guides for the eye.

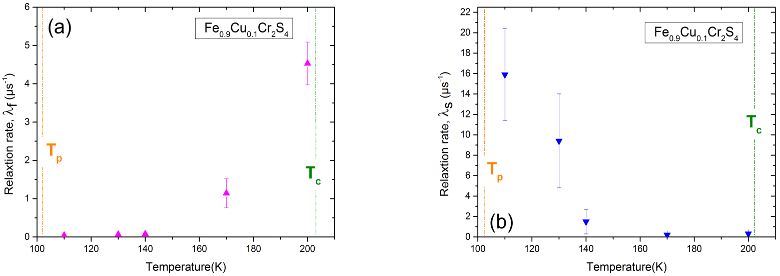

Figure 5.51: Temperature dependence of: (a) the fast relaxation rate λ_f, and (b) the slow relaxation rate λ_s for a two exponential fit above T_p for $Fe_{0.9}Cu_{0.1}Cr_2S_4$.

The fitted values for the fluctuation rate ν_{KT} and static width a_{KT} are shown in Fig. 5.50. The static width decreases with increasing temperature showing no special features below 100 K. In contrast, the fluctuation rate presents a clear irregularity between 20 K and 80 K. The large value of the static width together with fluctuation rate is sign of a strong disorder. This confirms the coexistence of long range magnetically ordered with a disordered spin state that has spin glassy behavior.

Above T_p, the relative field width in Fig. 5.47 rises again an order of magnitude indicating that the spin system becomes substantially locally disordered and the loses its strict long-range ordered feature. The temperature dependence of the fast and slow relaxation rates are presented in Fig. 5.51. The value of the fast relaxation rate λ_f rises approaching to T_c, while the temperature dependence of slow relaxation rate shows no significant maximum near the magnetic transition temperature but increases below T_c.

5.4.2

$Fe_{0.8}Cu_{0.2}Cr_2S_4$

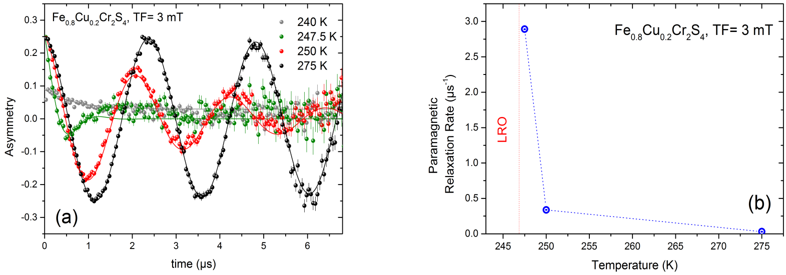

Figure 5.52: (a) TF = 3 mT spectra of $Fe_{0.8}Cu_{0.2}Cr_2S_4$ in paramagnetic phase. (b) Temperature dependence of the paramagnetic relaxation rate (the lines are guides to the eye).

Transverse field measurements were carried out in a small magnetic field of 3 mT in the temperature range 10 - 245 K. Typical spectra are shown in Fig. 5.52a. Upon approaching the Curie point the damping increases considerably, as shown in the Fig. 5.52b at T = 247.5 K. Good fits to the transverse field spectra of this concentration are also obtained with the function introduced in eq. 5.1 with only one muon frequency precession. The initial asymmetry is about 0.27(1) which has been used to ZF data, specially for the low temperature measurements, where the initial asymmetry is not resolved for early times of the spectrum.

Zero field μSR time spectra were taken in the temperature interval 10 - 245 K. The data at a few selected temperatures are shown in Fig. 5.53. The solid lines are fits using equations 5.3 and 5.4 for below T_p and above, respectively. The $T_p = 100 \pm 10\ K$, here for the $x = 0.2$ concentration, is similar comparing to $x = 0.1$. As mentioned already, T_p is a boundary to divide two temperature regimes observed in low concentrations of Cu, $x < 0.5$.

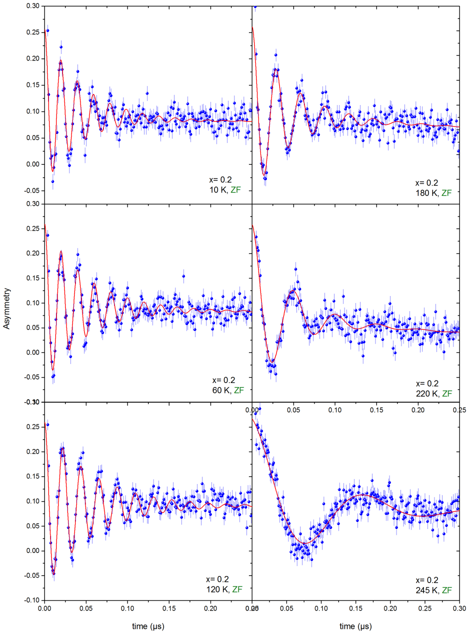

Figure 5.53: Initial part of zero field μSR spectra of $Fe_{0.8}Cu_{0.2}Cr_2S_4$ ($x = 0.2$) at selected temperatures. The solid lines are the least square fit to the relaxation function described in equations 5.3 and 5.4.

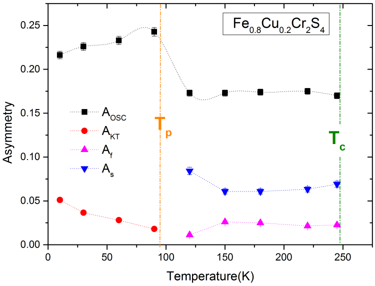

Figure 5.54: $Fe_{0.8}Cu_{0.2}Cr_2S_4$, The temperature dependence of the asymmetry described in the text. The dashed lines are guides for the eye. The vertical dashed lines indicate the positions of T_p and T_c.

Fig. 5.54 shows the contribution of each relaxation function to total asymmetry. As for $x = 0.1$, the spectra below $T_p \approx 100$ K could be well fitted with the relaxation function described in equation 5.3, i.e. a combination of a single- frequency cosine oscillation and a dynamic Kubo-Toyabe relaxation function (DLKT). The muon relaxation functions described in eq. 5.4 are used to fit the spectra above T_p. As depicted in this figure, the tendency of the asymmetry is the same as for $x = 0.1$ but the contribution in total asymmetry is changed. The temperature dependence of the muon precession frequency and the Fourier power are depicted in Fig. 5.55.

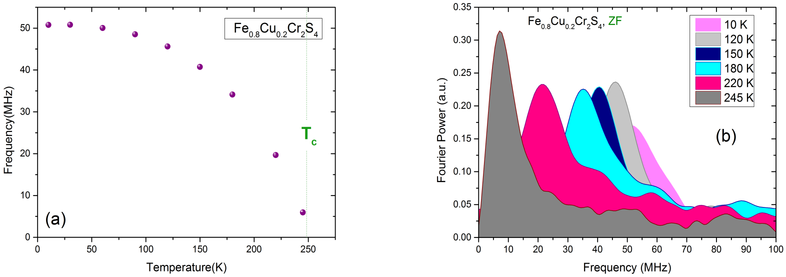

Figure 5.55: (a) Temperature dependence of the muon precession frequency . (b) Fourier power of the selected spectra at various temperatures for $Fe_{0.8}Cu_{0.2}Cr_2S_4$.

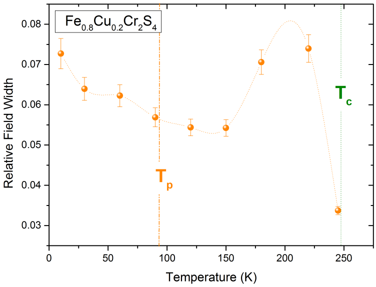

Figure 5.56: Dependence on the temperature of the relative field distribution width $\Delta B_\mu / B_\mu^0$ for $Fe_{0.8}Cu_{0.2}Cr_2S_4$.

As shown in Fig. 5.56, below T_p the relative field width is slightly increasing when temperature decreases. The temperature dependence of the static width a_{KT} and fluctuation rate ν_{KT} are also demonstrated in Fig. 5.57. The a_{KT} rises gradually upon cooling and suddenly

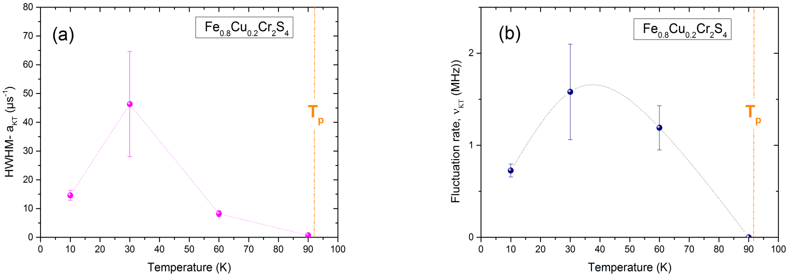

Figure 5.57: (a) Temperature dependence of static width a_{KT} and (b) Fluctuation rate v_{kt} derived from dynamical Kubo-Toyabe function fits to ZF data for $Fe_{0.8}Cu_{0.2}Cr_2S_4$. The lines are guides for the eye.

gets a small value at lowest measured temperature 10 K. The fluctuation rate v_{KT} seems also to have the same tendency as for $x = 0.1$.

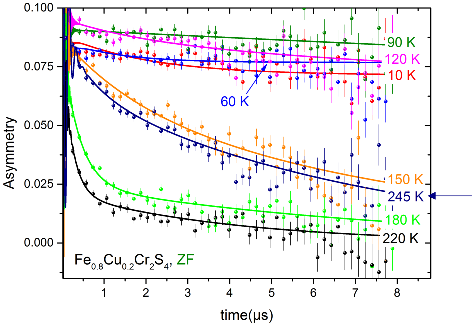

Figure 5.58: ZF spectra of $Fe_{0.8}Cu_{0.2}Cr_2S_4$ at selected temperatures within the long range magnetically ordered regime in low time resolution.

Above T_p, the relative field distribution has a peak around 200 K (see Fig. 5.56). Also the behavior of the relaxation rate above $T_p \approx 100$ K is different to the $x = 0.1$ as one can see by following the spectra at long-times for various temperatures especially for 245 K shown in Fig. 5.58.

In Fig. 5.59, the slow and fast relaxation rates are depicted; λ_s increases continuously and suddenly drops down to nearly zero near T_c, λ_f has a jump approaching to T_c.

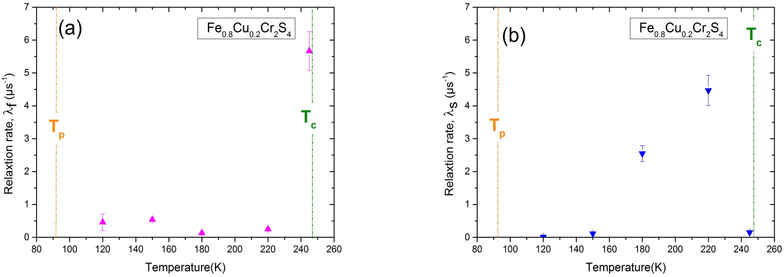

Figure 5.59: Temperature dependence of (a) the fast relaxation rate λ_f, and (b) the slow relaxation rate λ_s for a two exponential fit above T_p for $Fe_{0.8}Cu_{0.2}Cr_2S_4$.

5.4.3

$Fe_{0.7}Cu_{0.3}Cr_2S_4$

The μSR results of $Fe_{0.7}Cu_{0.3}Cr_2S_4$ follow the same systematic as seen for x = 0.2. Fig. 5.60 shows the typical transverse field μSR spectra measured in an external field of 3 mT. Increasing of the paramagnetic relaxation rate is sign of entering to a magnetically ordered phase (T_c = 288 K).

Typical ZF μSR spectra of $Fe_{0.7}Cu_{0.3}Cr_2S_4$ at selected temperatures are presented in Fig. 5.61. The spectra have been fitted to the same muon relaxation functions used for x = 0.1 and 0.2.

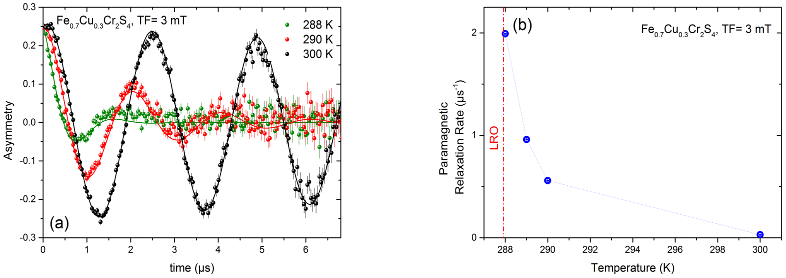

Figure 5.60: (a) TF = 3 mT spectra of $Fe_{0.7}Cu_{0.3}Cr_2S_4$ in paramagnetic phase. (b) Temperature dependence of the paramagnetic relaxation rate (the lines are guides to the eye).

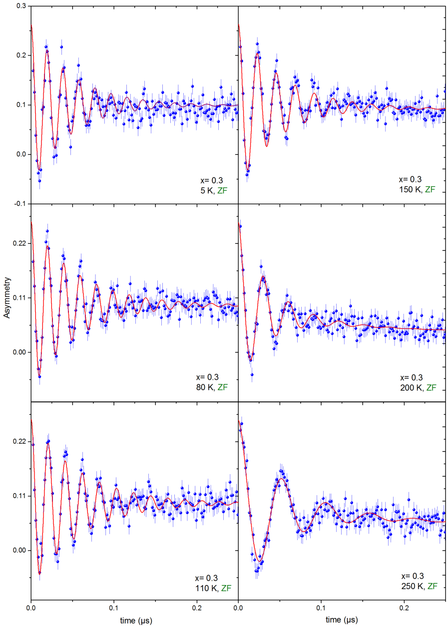

Figure 5.61: Initial part of zero field μSR spectra of the $Fe_{0.7}Cu_{0.3}Cr_2S_4$ $(x = 0.3)$ at selected temperatures.The solid lines are the least square fit to the relaxation function described in equation 5.3 and 5.4.

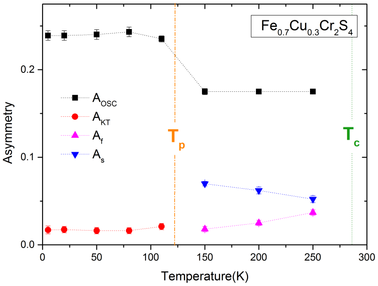

Figure 5.62: Temperature dependence of the asymmetries described in the text for $Fe_{0.7}Cu_{0.3}Cr_2S_4$. The dashed lines are guides for the eye. The vertical dashed lines indicate the position of T_p and T_c.

The temperature dependence of asymmetries displays a similar tendency observed for the $x = 0.1$ and $x = 0.2$ (see Fig. 5.62). The only difference is the value of each asymmetry (A_{KT}, A_{osc}, A_f and A_s). T_p is about 120 K.

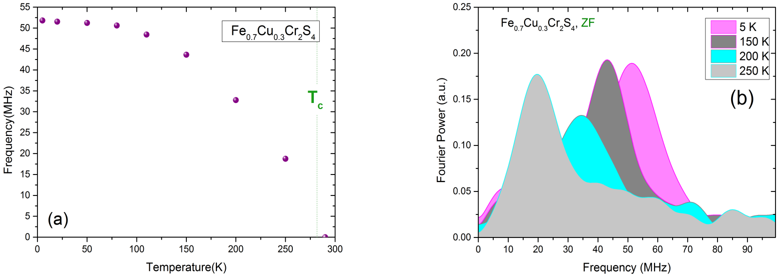

Figure 5.63: (a) Temperature dependence of the muon precession frequency. (b) Fourier power of the selected spectra at various temperatures for $Fe_{0.7}Cu_{0.3}Cr_2S_4$.

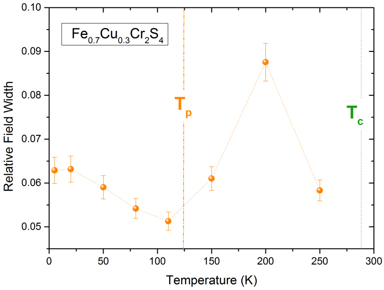

Figure 5.64: Dependence on the temperature of the relative field distribution width $\Delta B_\mu / B_\mu^0$ for $Fe_{0.7}Cu_{0.3}Cr_2S_4$.

The temperature dependence of local magnetic field does not show any distinct anomaly (Fig. 5.63a), but the local field distribution has a peak at 200 K as seen in both plots of the Fourier power and temperature dependence of relative field (see Figs. 5.63a and 5.64).

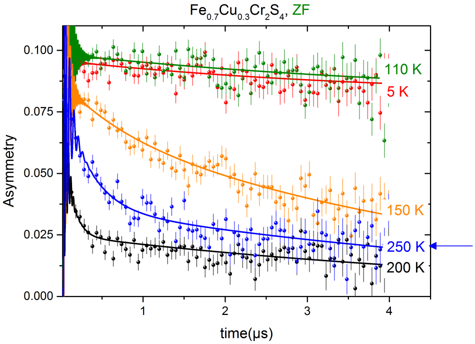

Figure 5.65: ZF spectra of $Fe_{0.7}Cu_{0.3}Cr_2S_4$ at selected temperatures within the long range magnetically ordered regime in low time resolution.

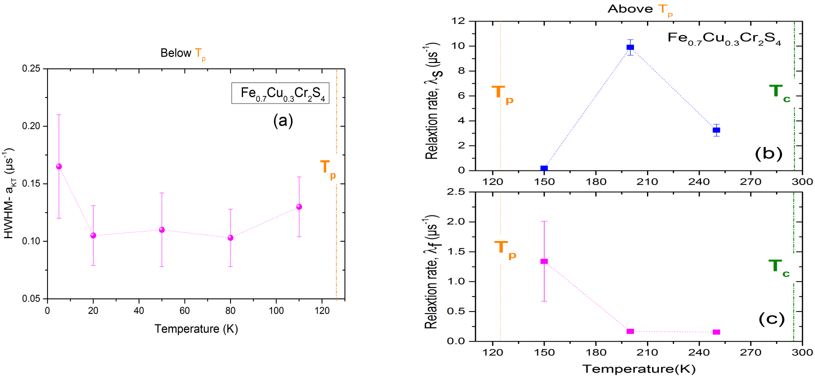

Figure 5.66: (a) Temperature dependence of static width a_{KT} derived from dynamical Kubo-Toyabe function below T_p. (b) Relaxation rate λ_f, and (c) λ_s for a two exponential fit above T_p for $Fe_{0.7}Cu_{0.3}Cr_2S_4$.The lines are guides for the eye.

As observed in Fig. 5.65, the spectra below T_p and above prove two different temperature regimes fitted by different muon spin relaxation functions. Below $T_p \approx 120$ K, where the spectra have been fitted by DLKT relaxation function and one single oscillatory pattern, the contribution of DLKT is small and the oscillation part is dominant. The hopping rate ν_{KT} can be fixed to zero due to its small value. The static width a_{KT} in Fig.5.66a increases slightly with decreasing temperature indicating no distinct anomaly below T_p. Above 130 K, the fast relaxation rate is smoothly decreasing, while the slow relaxation rate has a peak at 200 K. This anomaly can be seen directly from spectra shown in Fig. 5.65 indicated by arrow.

5.4.4

$Fe_{0.6}Cu_{0.4}Cr_2S_4$

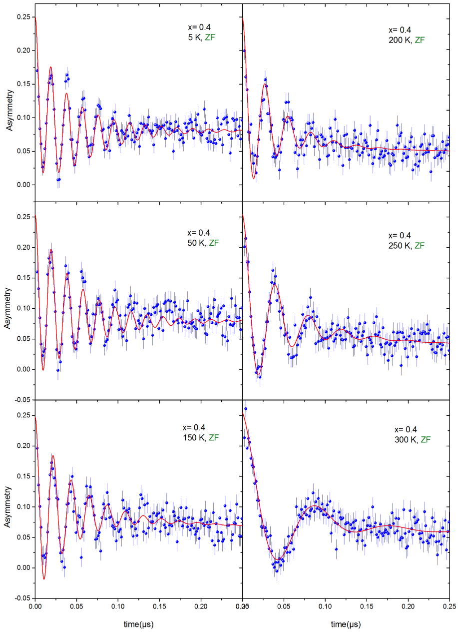

Figure 5.67: Initial part of zero field μSR spectra of the $Fe_{0.6}Cu_{0.4}Cr_2S_4$ ($x = 0.4$) at selected temperatures. The solid lines are the least square fit to the relaxation function described in equation 5.3 and 5.4.

ZF μSR spectra of $Fe_{0.6}Cu_{0.4}Cr_2S_4$ at some selected temperatures are depicted in Fig. 5.67. The solid lines are the fits using those function described in equation 5.3 and 5.4 as used for the other concentrations.

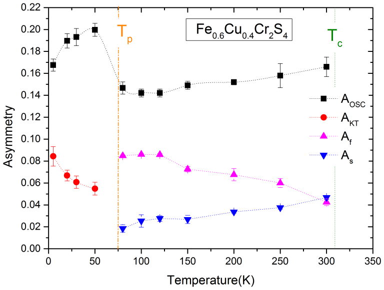

Figure 5.68: Temperature dependence of the asymmetry parameters described in text for Fe$_{0.6}$Cu$_{0.4}$Cr$_2$S$_4$. The dashed lines are guides for the eye.

The temperature dependence of asymmetries included in fit function reveal obvious differences compared to smaller x. As observed in Fig. 5.68, the weight of the DLKT asymmetry is much higher and T$_p \approx 70$ K is smaller compared to $x = 0.1$, 0.2, and 0.3). Note that A_f and A_s are approximately constant at temperatures between 80 K and 150 K, but above 150 K, A_f decreases while A_s increases. This anomaly between 150 - 200 K can be seen from other parameters as well.

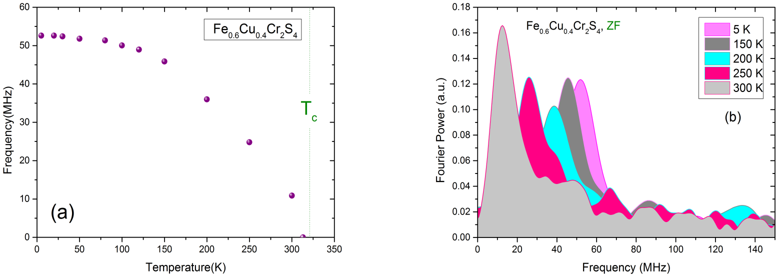

Figure 5.69: (a) Temperature dependence of the muon precession frequency. (b) Fourier powers of the selected spectra at various temperatures for Fe$_{0.6}$Cu$_{0.4}$Cr$_2$S$_4$.

As depicted in Fig. 5.69, the temperature dependence of the muon precession frequency does not show any marked feature but the shape of its development is smoothly changed from Brillouin-like behavior comparing to smaller x. As seen in Fig. 5.69, the Fourier powers of the all spectra show rather sharp peaks except for 200 K. This anomaly can also observed in the temperature dependence of the relative field width presented in Fig. 5.70. In the low time resolution ZF spectra shown in Fig. 5.71, one can see the two different

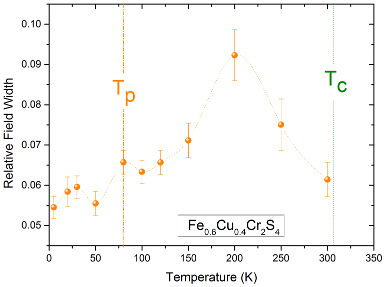

Figure 5.70: Dependence on the temperature of the relative field distribution width $\Delta B_\mu/B^0_\mu$ for $Fe_{0.6}Cu_{0.4}Cr_2S_4$.

temperature regions by following the behavior of relaxation rate. The changed damping character is marked with a dashed circle for four lowest temperatures below $T_p \approx 70$ K. The parameters of the DLKT relaxation function are plotted in Fig. 5.72. The static width a_{KT} has higher value at lowest temperature and decreases with increasing temperature. The fluctuation rate ν_{KT} has a peak at 20 K which is also can be observed from the spectra in Fig. 5.71

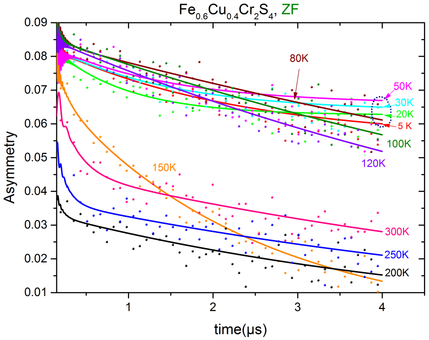

Figure 5.71: High times ZF spectra of $Fe_{0.6}Cu_{0.4}Cr_2S_4$ at selected temperatures within the long range magnetically ordered regime.

Above 70 K, one can see directly the changes of relaxation rate at various temperatures in figures 5.71 and 5.73. Temperature dependence of λ_s shows a decreases, above 150 K while λ_f increases above this temperature. The increasing of λ_f is directly visible from the spectra above 150 K (see Fig. 5.71).

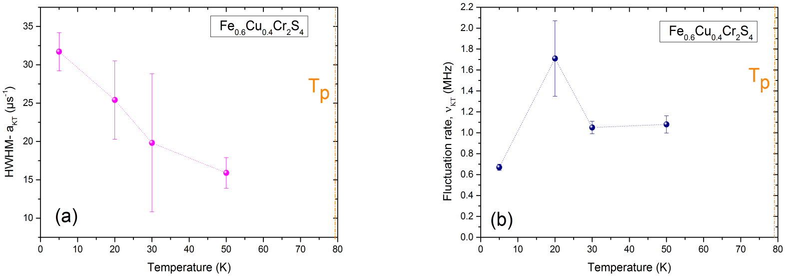

Figure 5.72: (a) Temperature dependence of static width a_{KT}, and (b) fluctuation rate ν_{KT} derived from dynamical Kubo-Toyabe function fits to ZF data of $Fe_{0.6}Cu_{0.4}Cr_2S_4$. The lines are guides for the eye.

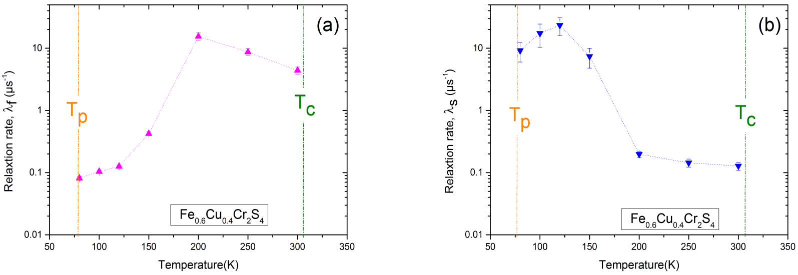

Figure 5.73: Temperature dependence of (a) the fast relaxation rate λ_f, and (b) the slow relaxation rate λ_s for a two exponential fit above T_p for $Fe_{0.6}Cu_{0.4}Cr_2S_4$.

5.4.5

$Fe_{0.5}Cu_{0.5}Cr_2S_4$

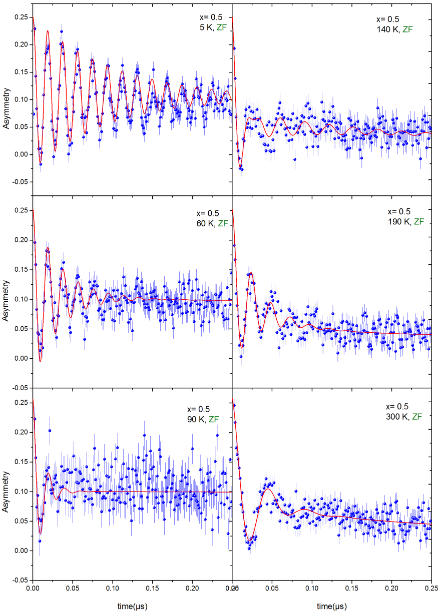

Figure 5.74: Initial part of the zero field μSR spectra of the $Fe_{0.5}Cu_{0.5}Cr_2S_4$ ($x = 0.5$) at selected temperatures.

ZF μSR spectra of $Fe_{0.5}Cu_{0.5}Cr_2S_4$ at selected temperatures are presented in Fig. 5.74. It can be easily seen, that the damping of oscillation is rather strong especially for spectra at 90 K and 140 K. The spectra have been fitted to the same muon spin relaxation functions as described already except for 90 K and 140 K, where the oscillation pattern is not only single cosine any more and it should be fitted with two muon precession frequencies. Lowest temperatures below $T_p \approx 80$ K can be well described by the relaxation function described in eq. 5.3. The temperature range 80 - 150 K (the region between dashed lines $T_p < T < T_k$) could be fitted to eq. 5.4, but P_{osc} is

$$P_{osc}(t) = A_{osc1}\exp(-\lambda_{osc1}t)\cos(\omega_{osc1}t) + A_{osc2}\exp(-\lambda_{osc2}t)\cos(\omega_{osc2}t) \tag{5.7}$$

This division can be better observed from the temperature dependence of the asymmetries (Fig. 5.75). A_f and A_s are relatively constant in the temperature range 80 - 150 K and above on. A_{osc2} has small value compared to A_{osc1}.
The frequencies ($\nu_{osc1,2} = \omega_{osc1,2}/2\pi$) are plotted in Fig. 5.76, both have broad distributions. Fourier powers at selected temperatures are given in Figs. 5.76b and 5.77a. Temperature

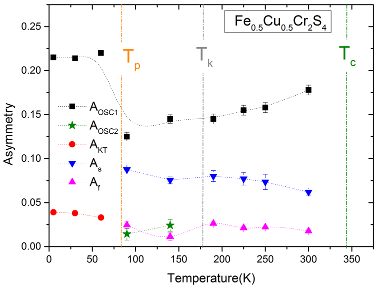

Figure 5.75: Temperature dependence of the asymmetry parameters extracted from the muon relaxation function for $Fe_{0.5}Cu_{0.5}Cr_2S_4$. The dashed lines are guides for the eye.

dependence of the relative line width derived from λ_{osc1} and λ_{osc2} tell, that the main frequency ν_{osc1} is damped out very fast by strong increase of λ_{osc1}. At lower temperatures and higher temperatures (T < T_p and T > T_k), the damping gets smaller and the oscillations become more visible.

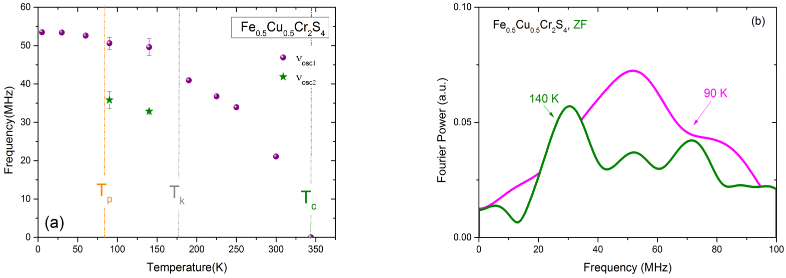

Figure 5.76: (a) Temperature dependence of the muon precession frequency $\nu_{osc} = \omega_{osc}/2\pi$. (b) Fourier powers of two spectra at 90 K and 140 K for $Fe_{0.5}Cu_{0.5}Cr_2S_4$.

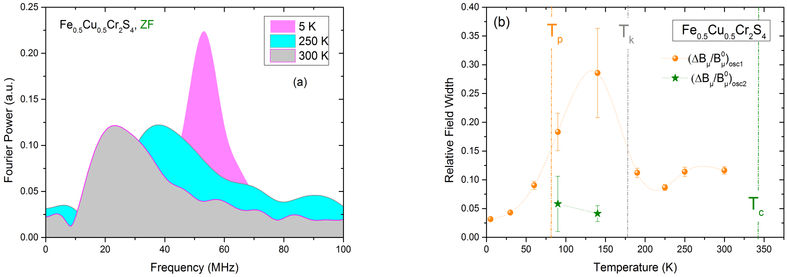

Figure 5.77: (a) Fourier powers of selected temperatures, 5 K, 250 K and 300 K. (b) Dependence on the temperature of the relative field distribution width $\Delta B_\mu/B_\mu^0$ for $Fe_{0.5}Cu_{0.5}Cr_2S_4$.

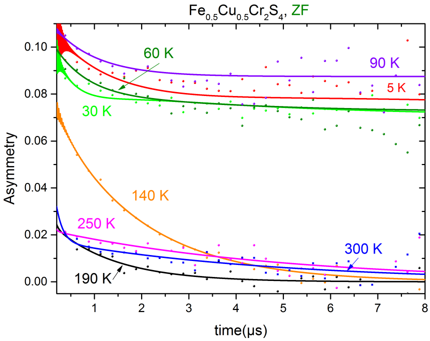

Figure 5.78: ZF spectra of $Fe_{0.5}Cu_{0.5}Cr_2S_4$ at selected temperatures within the long range magnetically ordered regime in low time resolution.

The strong effect of changing relaxation rates can be seen in the spectra plotted in Fig. 5.78 and is similar to the other concentrations.

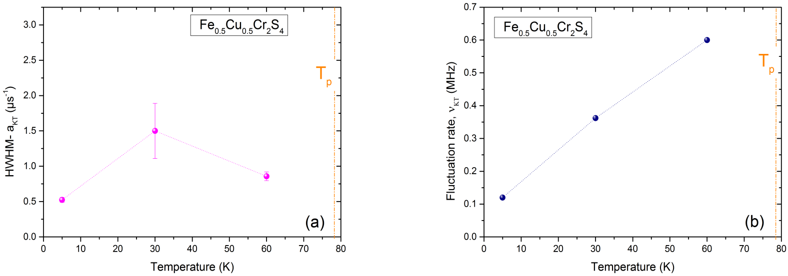

Figure 5.79: (a) Temperature dependence of static width a_{KT}, and (b) fluctuation rate ν_{KT} derived from dynamic Kubo-Toyabe function fits to ZF data of $\mathrm{Fe_{0.5}Cu_{0.5}Cr_2S_4}$. The lines are guides for the eye.

Below T$_p$ = 80 K, the fluctuation rate ν_{KT} is linearly increasing while a_{KT} is approximately constant shown in Fig. 5.79a.

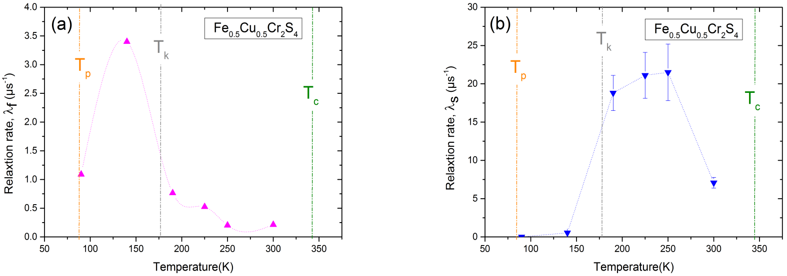

Figure 5.80: Temperature dependence of (a) the fast relaxation rate λ_f, and (b) the slow relaxation rate λ_s for a two exponential fit above T$_p$ for $\mathrm{Fe_{0.5}Cu_{0.5}Cr_2S_4}$.

Above 80 K, the fast relaxation rate λ_f has a peak at 140 K (T$_p$ < T < T$_k$) and gradually decrease approaching to T$_c$. λ_s is nearly zero in the temperature range between T$_p$ < T < T$_k$ and suddenly increases to high values above 140 K. Both relaxation rates decrease near room temperature.

5.4.6

$Fe_{0.4}Cu_{0.6}Cr_2S_4$

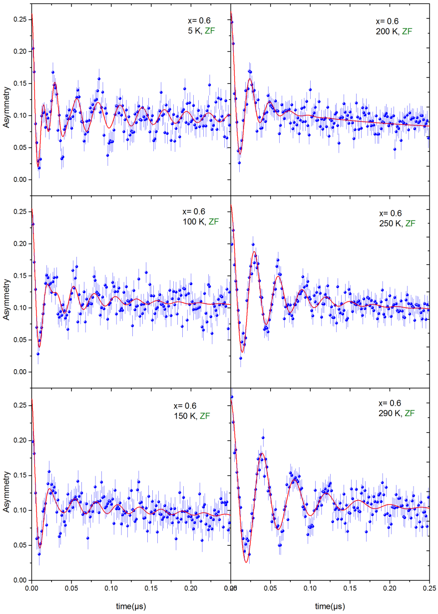

Figure 5.81: Initial part of zero field μSR spectra of the $Fe_{0.4}Cu_{0.6}Cr_2S_4$ ($x = 0.6$) at selected temperatures.

The early times of ZF spectra of $Fe_{0.4}Cu_{0.6}Cr_2S_4$ are demonstrated in Fig. 5.81. All spectra have been fitted by the muon relaxation function described for $x = 0.5$. It can be seen from the temperature dependent asymmetries depicted in Fig. 5.82 that the second oscillating contribution stays in the whole temperature range below 170 K. Both oscillating fractions show dramatic changes in the temperature range between $T_p \approx 80$ K and $T_k \approx 170$ K where we have an onset of A_s and A_f.

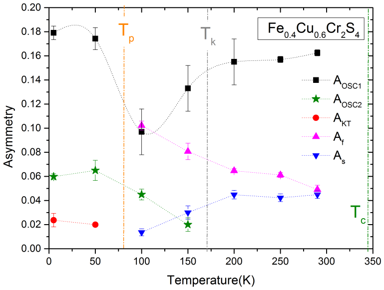

Figure 5.82: Temperature dependence of the asymmetry parameters for each components extracted from fit function for Fe$_{0.4}$Cu$_{0.6}$Cr$_2$S$_4$. The dashed lines are guides for the eye.

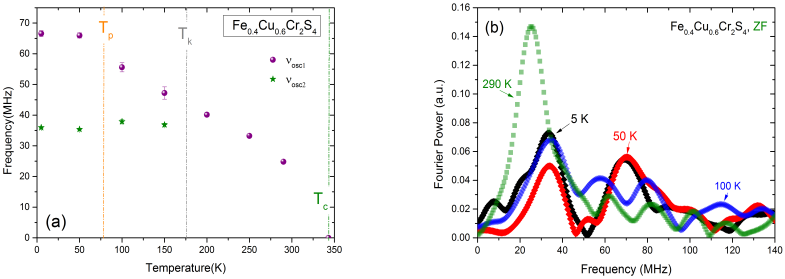

Figure 5.83: (a) Temperature dependence of the muon precession frequency. (b) Fourier powers of the selected spectra at various temperatures for Fe$_{0.4}$Cu$_{0.6}$Cr$_2$S$_4$.

The temperature dependencies of muon precession frequencies and Fourier power are shown in Fig. 5.83 and indicate that below 170 K there are two frequencies. Temperature dependence of the relative field width of main frequency signal λ_{osc1} has a peak at 150 K and decreases with increasing temperature while λ_{osc2} is nearly constant.

The low resolution ZF spectra shown in Fig. 5.85 display the same tendency as observed for other studied concentrations. Below T$_p$ $\approx$ 80 K the fluctuation rate ν_{KT} has small values (ν_{KT} = 0.76 and 0.01 μs^{-1} for 5 K and 50 K, respectively). Also the static field widths a_{KT} are nearly constant for these two temperatures (a_{KT} = 0.9(1) and 0.6(1) μs^{-1} for 5 K and 50 K, respectively).

The temperature variation of relaxation rates above T$_p$ = 80 K is plotted in Fig. 5.86. Both relaxation rates λ_f and λ_s exhibit a peak around 200 K (see Fig. 5.86).

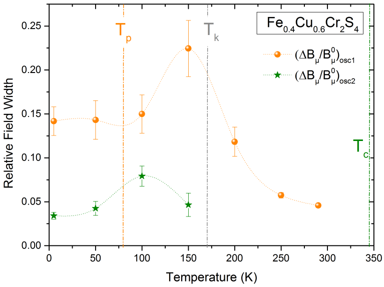

Figure 5.84: Dependence on the temperature of the relative field distribution width $\Delta B_\mu/B_\mu^0$ for $Fe_{0.4}Cu_{0.6}Cr_2S_4$.

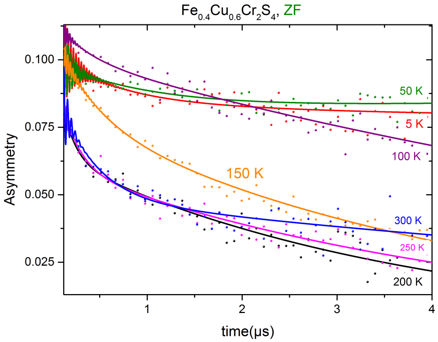

Figure 5.85: ZF spectra of $Fe_{0.4}Cu_{0.6}Cr_2S_4$ at selected temperatures within the long range magnetically ordered regime in low time resolution.

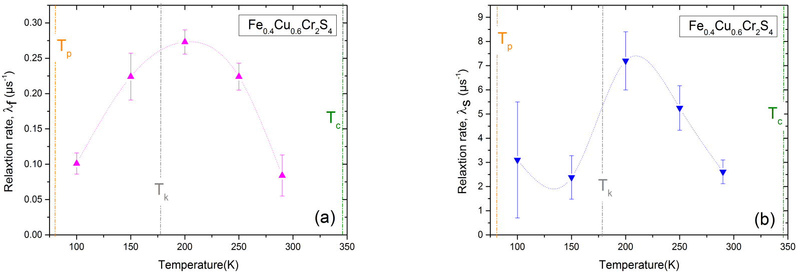

Figure 5.86: Temperature dependence of (a) the fast relaxation rate λ_f, and (b) the slow relaxation rate λ_s for a two exponential fit above T_p for $Fe_{0.4}Cu_{0.6}Cr_2S_4$.

5.4.7

$Fe_{0.2}Cu_{0.8}Cr_2S_4$

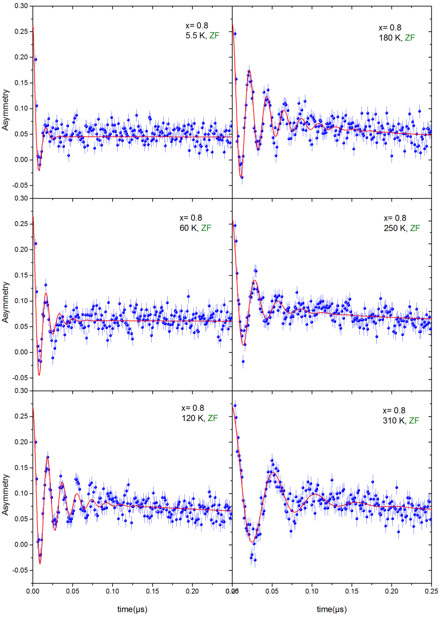

Figure 5.87: Initial part of zero field μSR spectra of the $Fe_{0.2}Cu_{0.8}Cr_2S_4$ ($x = 0.8$) at selected temperatures. The solid lines are the least square fit to the relaxation function described in equation 5.4.

High times and low times resolution ZF μSR spectra are illustrated in Figs. 5.87 and 5.88. As seen in the initial part of the spectrum (Fig. 5.87), the oscillations are strongly damped due to a sizable λ_{osc} at lowest temperatures. Also the low resolution of the lowest temperatures are not similar to other concentrations. All the spectra could be well fitted using the relaxation function of eq. 5.4 with only one precession signal. There was no indication for a Kubo-Toyabe contribution even for low temperature.

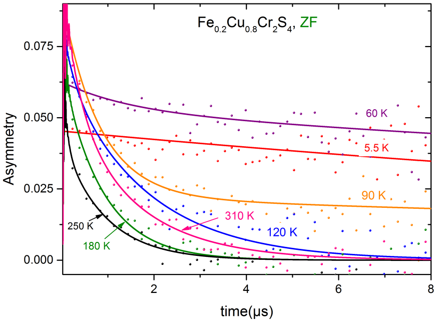

Figure 5.88: ZF spectra of $Fe_{0.2}Cu_{0.8}Cr_2S_4$ at selected temperatures within the long range magnetically ordered regime in low time resolution.

Temperature dependencies of asymmetries are depicted in Fig. 5.89 revealing three asymmetries, A_{osc}, A_f and A_s. The temperature variation of them shows that the A_s increases leading to the decrease of A_{osc} and A_f.

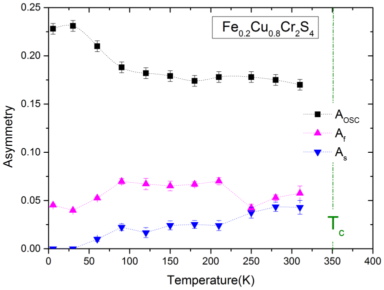

Figure 5.89: Temperature dependence of the asymmetries described by equation 5.4 for $Fe_{0.2}Cu_{0.8}Cr_2S_4$. The dashed lines are guides for the eye.

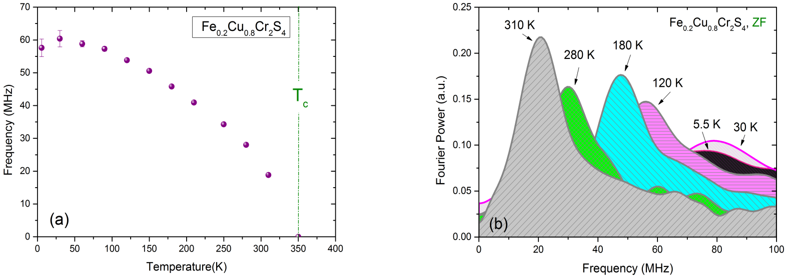

Figure 5.90: Temperature dependence of the muon precession frequency (left). Fourier powers of the selected spectra at various temperatures (right) for $Fe_{0.2}Cu_{0.8}Cr_2S_4$.

Also Fourier powers shown in Fig. 5.90b prove that the spectra can be satisfactorily described by only one single cosine oscillatory pattern having dramatic damping at lower temperatures. The temperature dependence of the frequency indicates a reduction at lowest temperature, which, however, is in the range of error due to strong damping. λ_{osc} and thus relative field width (Fig. 5.91) increases with decreasing temperature and have highest values at lowest temperatures.

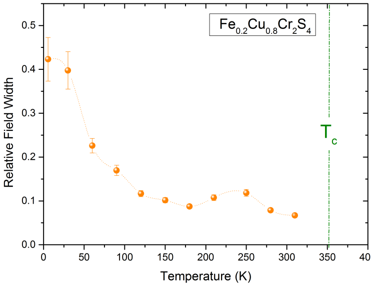

Figure 5.91: Dependence on the temperature of the relative field distribution width $\Delta B_\mu / B_\mu^0$ for $Fe_{0.2}Cu_{0.8}Cr_2S_4$.

Turning now to the relaxation part of the fit function of spectra shown in Fig. 5.88. As mentioned already, asymmetries A_{osc} and A_f are changed upon appearance of the slow relaxation contribution. This can be seen in Fig. 5.88 from the strong change in spectral shape between 60 K and 90 K. Fast and slow relaxation rates $\lambda_{f,s}$ have considerable values in the temperature range 180 K - 280 K. At 300 K, λ_s and λ_f are gradually decreasing.

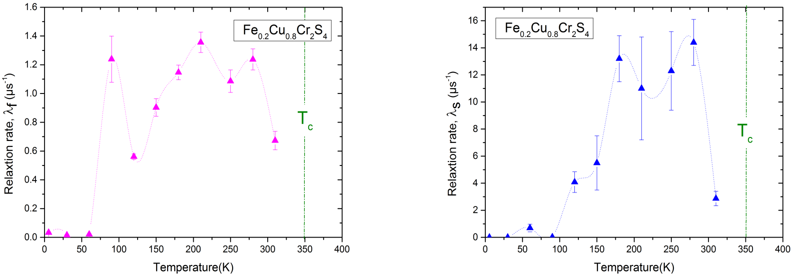

Figure 5.92: Temperature dependence of (a) the fast relaxation rate λ_f, and (b) the slow relaxation rate λ_s for a two exponential fit above T_p for $Fe_{0.2}Cu_{0.8}Cr_2S_4$.

Chapter 6

Discussion

Whereas many properties of semiconducting pure $FeCr_2S_4$ can be reasonably understood in an ionic picture for Fe^{2+} and Cr^{3+} in tetrahedral and octahedral S coordination, respectively, see chapter 4, we have to extend this approach to a more detailed band picture for the Cu doped compounds that display more metallic behavior.

In this discussion we start with the considerations for the electronic structure put forward by Fritsch et al. [2003] and try to apply it to our data for Mössbauer spectroscopy and μSR. These two methods in company with magnetization measurements give different views of magnetism: Mössbauer spectroscopy is performed at iron and μ^+ is supposed to be positioned near the sulfur.

6.1

Development of Fe^{2+} to Fe^{3+}

By evaluation of the center shift from Mössbauer results one can determine the ion valence state in the series $Fe_{1-x}Cu_xCr_2S_4$. Fig. 6.1 shows the Mössbauer spectra of $Fe_{1-x}Cu_xCr_2S_4$ for $0 \leqslant x \leqslant 0.8$ at T = 20 K. Cu doping of $x = 0.1$ firstly causes severe line broadening. By further increasing x, the spectra are getting sharper with a clear sign for increasing of Fe^{3+} compared to pure $FeCr_2S_4$ having only oxidation states Fe^{2+}. From the different center shifts for Fe^{2+} and Fe^{3+}, we can separate their spectral contributions. The area weighted average of the center shifts of spectra at 20 K for different concentrations are shown in Fig. 6.2.

Fig. 6.3 illustrates the area fractions of Fe^{3+} and Fe^{2+} depending on Cu concentration indicating the gradual transformation of Fe^{2+} to Fe^{3+}. This transformation is continuous and we will try to interpret it using a binomial distribution for a random cation distribution over the spinel lattice. The probability $P(k)$ for the tetrahedral Fe^{2+} (A-sites) ion to have among the nearest tetrahedral A neighbors k ions of Cu is

$$P(k) = \frac{4!}{K!(4-k)!} (1-z)^{4-k} (z)^k \tag{6.1}$$

where z is the fraction of iron and copper in tetrahedral A-sites, which are the nearest neighbors of Fe^{2+}. Each Cu in tetrahedral sites interacts with six nearest Cr^{3+} (B-sites) ions and four A ions (Fe^{2+}, Fe^{3+} and Cu).

Assuming that the $P(0)$ and $P(1)$ components belong to the Fe^{2+} in the Mössbauer spectra and the $P(2)$, $P(3)$, $P(4)$ components are responsible for the Fe^{3+}, the area ratio from the calculated binomial distribution is in good agreement with our experimental data shown in Fig. 6.3a. Therefore, we can conclude, that Fe^{2+} is present as long as there is no or only one Cu neighbor, Fe^{3+} for more than two Cu neighbors. For $x \geqslant 0.5$ there appears to be

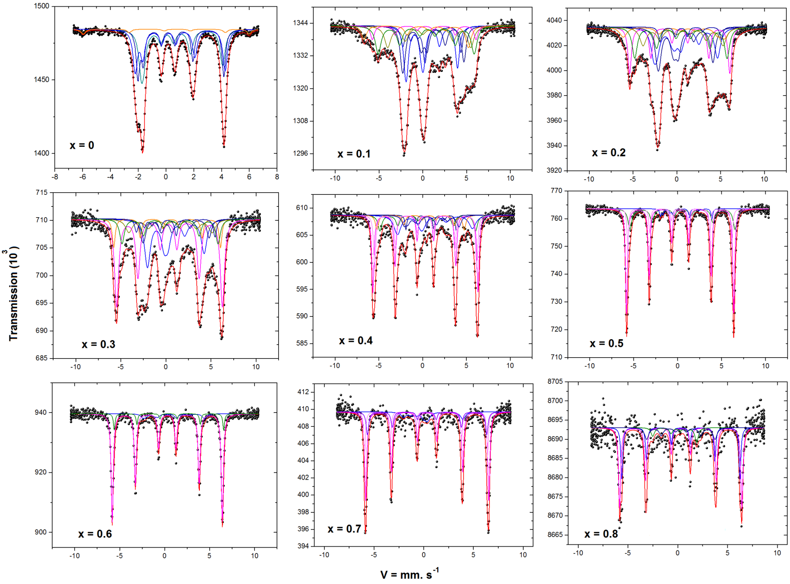

Figure 6.1: Development of Fe^{3+} in the tetrahedral A-sites.

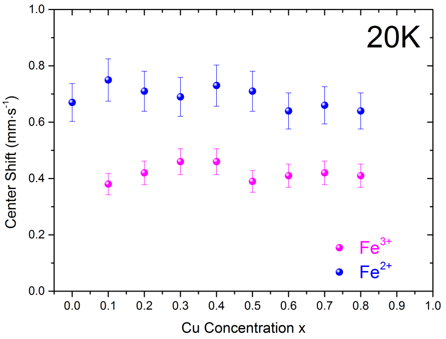

Figure 6.2: Concentration dependence of center shift at 20 K in $Fe_{1-x}Cu_xCr_2S_4$.

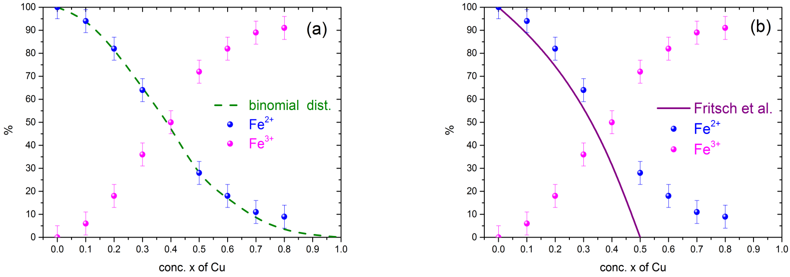

Figure 6.3: Cu concentration dependence of spectral area ratio Fe^{2+}/Fe^{3+} from fits to our Mössbauer spectra. (a) the binomial distribution (green dashed line); (b) Fitting with the model introduced by Fritsch et al. [2003], Lotgering et al. [1969] (see the text).

no complete vanishing of Fe^{2+}, supposedly caused by presence of Cu^{2+} (what would be in agreement with the model of Goodenough [1967]).

For comparison, Fig. 6.3b also shows the fitted experimental data with the valence distribution, using the formula $Fe^{2+}_{1-2x}Fe^{3+}_{x}Cu^{+}_{x}Cr^{3+}_{2}S^{2-}_{4}$ for $x \leqslant 0.5$, proposed by Lotgering et al. [1969] and Fritsch et al. [2003]. Our experimental data disagree with this model and the fraction of Fe^{2+} and Fe^{3+} differ from the values expected from this model. The mentioned model introduced the triple exchange model as a conduction mechanism, which is established via transferring an electron from Fe^{2+} to Fe^{3+} via S^{2-} ions leading to an intermediate Cr^{2+}. They supposed this hopping is fast enough to explain the metallic behavior of the system.

For an increased metallicity one may expect the formation of an intermediate valency with an iron state of roughly $Fe^{2.5+}$ that should be detected from the center shift. This has not been observed in our data, which means the electron transfer is not fast enough to average the center shifts of Fe^{2+} and Fe^{3+} (means slower than about 100 MHz), i.e. the system is rather localized (in contradiction with the model assumption of Fritsch et al. [2003]). The small change seen in the center shift at around 100 K for $x \leqslant 0.5$ (figures 5.12, 5.17, 5.22, and 5.27) can be related to the Jahn-Teller distortion (see below) causing a change in the space-charge distribution (Kugel and Khomskii [1982]).

6.2

Magnetic Behavior in the Concentration Range 0 ⩽ x < 0.5

Comparison of T_c as detected from the temperature dependencies of magnetization (ZFC and FC curves), Mössbauer magnetic hyperfine fields $B_{hf}(T)$, and muon precession frequencies $\nu_\mu(T)$) shows, that the magnetic transition temperatures T_c derived from different methods follow the same concentration dependence. The variation of T_c with composition taken from magnetization data is plotted in Fig. 6.4. The Curie temperature T_c increases

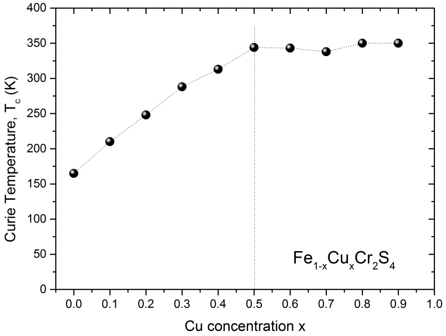

Figure 6.4: Influence of x on T_c in $\mathrm{Fe}_{1-x}\mathrm{Cu}_x\mathrm{Cr}_2\mathrm{S}_4$ taken from susceptibility measurements. The lines are guides to the eye.

with the substitution of the Fe ions by Cu for the range $0 \leqslant x \leqslant 0.5$. For $x < 0.5$, T_c follows a flatter concentration dependence. As mentioned already in section 4.5, the increase of T_c (up to $x = 0.5$) can be understood by the change of superexchange interaction with decreasing amount of Fe^{2+} in the A-sites (appearance of Fe^{3+}). Beyond $x = 0.5$, A-sites are mainly occupied by Fe^{3+}, therefore T_c is nearly constant (e.g. Haacke and Beegle [1967], Lotgering et al. [1969], Tsurkan et al. [2005]).

Below T_c, both Mössbauer and μSR analyses show a distribution of the magnetic hyperfine fields and spontaneous rotation frequencies (i.e. the interstitial magnetic field $B_\mu = \omega_\mu/\gamma_\mu$) indicated in the temperature dependence of line width ($HWHM$ in Mössbauer results) and relative field distribution width ($\Delta B_\mu/B_\mu^0$ in μSR).

Below T_c, $B_{hf}(T)$ of Fe^{2+} first follows the normal T-dependence of a sublattice magnetization curve expected for a ferrimagnet. Then, below a certain temperature T_m^{ME} we can distinguish two groups of subspectra with different behavior of B_{hf}, that we called group I and II (see section 5.3). At low temperatures, group I has lower values of B_{hf}, high values of EFG and also nonzero polar angles between V_{zz} and B_{hf} ($\theta \approx 90°$ and $\phi \approx 45°$) with an asymmetry parameter of EFG $\eta \approx 0.55$. This is comparable to the main spectral components found in pure $\mathrm{FeCr}_2\mathrm{S}_4$ (see section 4.3). Group II reveals a broadened distribution of higher magnetic hyperfine fields and with a small EFG. While with increase of Cu doping x the relative ratio of $\mathrm{Fe}^{3+}/\mathrm{Fe}^{2+}$ is increasing (see above), the ratio between divalent group I/group II stays around 1.6(4).

We now turn to a closer interpretation of the temperature dependence of the nuclear electric quadrupole interaction derived from the Mössbauer data. While for group II the quadrupole splitting has nearly zero values, group I reveals information on the crystal field at Fe^{2+}. Group I shows three temperature regions for temperature dependence of QS, a small quadrupole splitting and normal behavior for B_{hf} between T_c and T_m^{ME}, an increasing

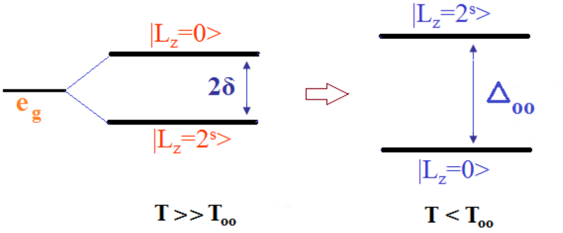

Figure 6.5: Interchange of the two lowest orbital levels of Fe^{2+} in tetrahedral site. Below T_c and above T_{oo}, The lower orbital level is predominantly $|L_z = 2^s\rangle$, corresponding to a positive electric field gradient parameter $e^2qQ/2$. The major axis of the EFG is along the magnetization direction (ϕ and θ are zero) and the asymmetry parameter is also zero. Below T_{oo}, the lowest level change to $|L_z = 0\rangle$.

of QS in parallel to decrease of B_{hf} starting below T_m^{ME}, and finally a remarkable anomaly of QS around T_{og}^{ME}. T_{og}^{ME} labels the temperature where the sign of EFG changes from positive to negative.

In the following we interpret the observed quadrupole splitting below T_c for $FeCr_2S_4$ related to the orbital ground state as proposed by Engelke [2010], and after that we generalize it to doped $Fe_{1-x}Cu_xCr_2S_4$ for group I.

As mentioned before, the tetrahedral crystal field splits the ^5D orbitals of Fe^{2+} into the lower doublet e_g and the triplet t_{2g} (see Fig. 4.3 in section 4.3). Below T_c, the ten-fold spin degeneracy of the e_g ground state is lifted by the exchange field in the magnetically ordered state, leading five orbital doublets spaced by Δ_{ex} ($\Delta_{ex} = kT_c$) even under cubic symmetry (our case). The e_g doublet will be further split by second-order spin-orbit and spin-spin interaction. The orbital doublets may also be further split by low-symmetry distortion (e.g. by Jahn-Teller effect).

According to Eibschütz et al. [1967] and Hoy and Singh [1968], the positive electric field gradient (EFG) observed below T_c in pure $FeCr_2S_4$ is induced by the magnetic ordering. Upon lowering temperature the unequal population of two lowest orbital levels leads to an electric field gradient EFG with an axial symmetry around easy axis direction of magnetization $\langle 100\rangle$. From the temperature dependence of the quadrupole interaction it is possible to derive the splitting 2δ of the two orbital levels. Engelke [2010] determined $2\delta \simeq 28$ K using eq. 6.2 (van Diepen and van Stapele [1972]) with a ground state of $|L_z = 2^s\rangle$ and $|L_z = 0\rangle$ being the energetically higher state.

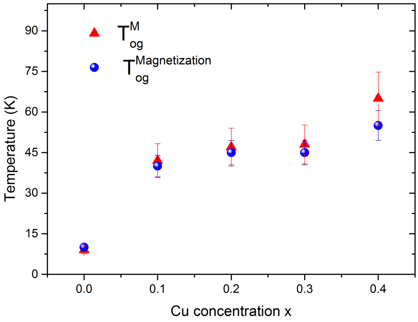

Figure 6.6: Comparison of the temperature of orbital glassy state derived from analyses of Mössbauer and magnetization data in concentration range $0 \leqslant x < 0.5$. The data for $x = 0.0$ (T_{oo}) taken from Tsurkan et al. [2010], Engelke et al. [2011], and Kalvius et al. [2013].

$$QS(T) = QS(0)\frac{\sum_{m=-2}^{2}\exp(\frac{m\Delta_{ex}}{k\mathrm{T}})\sinh(\frac{\delta(2-m^2)}{2k\mathrm{T}})}{\sum_{m=-2}^{2}\exp(\frac{m\Delta_{ex}}{k\mathrm{T}})\cosh(\frac{\delta(2-m^2)}{2k\mathrm{T}})} \tag{6.2}$$

where $QS(0)$ is the quadrupole splitting for the $|L_z = 2^s\rangle$ state (around $+2.6\ \mathrm{mm \cdot s^{-1}}$) and $\Delta_{ex} = 250$ K. For temperatures below $\mathrm{T}_{oo} = 9$ K a doubling of the value of EFG is found combined with a change of sign of V_{zz} (and an asymmetry parameter $\eta \approx 0.2$ and $\theta \approx 90°$). Engelke [2010] derives the splitting of the ground state $\Delta_{oo} \simeq 32$ K comparable with value of the spin-orbit coupling above T_{oo}. The negative value of the EFG, however, indicates that the lowest energy levels have changed their positions. This change is supposed to be connected with orbital ordering below T_{oo}. The ground state now is $|L_z = 0\rangle$ having a planar magnetic anisotropy. This is seen as the reason for the deviation from the collinear spin structure met at high temperature.

A schematic view of orbital positions below T_c is shown in Fig. 6.5. Notably, the ground state below T_{oo} found for $\mathrm{FeCr_2S_4}$ is the same as for $\mathrm{FeCr_2O_4}$ proposed by Hartmann-Boutron and Imbert [1968].

Also for $\mathrm{Fe_{1-x}Cu_xCr_2S_4}$ we find a change of sign of EFG for $\mathrm{Fe^{2+}}$ group I (e.g. see Figs. 5.13 and 5.18). This occurs around temperature T_{oo}^{ME} that we again relate to orbital ordering, this time, however, to short-range orbital ordering (see later). Fig. 6.6 shows the $\mathrm{T}_{og}^{magnetization}$ taken from magnetization measurements (small bump at low temperature) and T_{og}^{ME} taken from Mössbauer measurements (the change in sign of EFG) for this concentration range. For higher concentrations $x \geqslant 0.5$ this transition is hardly distinguishable due to low amount of $\mathrm{Fe^{2+}}$.

The similarity in behavior of B_{hf} and QS seen for doped $\mathrm{Fe_{1-x}Cu_xCr_2S_4}$ for $x \leqslant 0.5$ and pure $\mathrm{FeCr_2S_4}$ made us to generalize the mentioned discussion to our results for the *Cu* doped

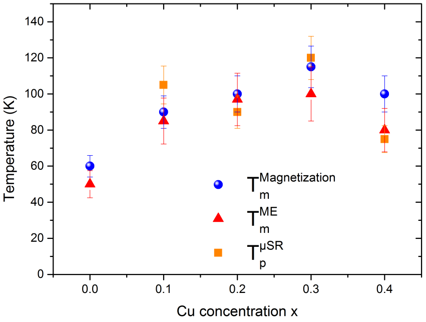

Figure 6.7: Comparison of the temperature of re-entrant spin glass state derived from analyses of Mössbauer, μSR, and magnetization data in concentration range $0 \leqslant x < 0.5$. The data for $x = 0.0$ taken from Tsurkan et al. [2010], Engelke et al. [2011], and Kalvius et al. [2013].

compounds.

From the sign and magnitude of the quadrupole splitting for $x \leqslant 0.5$ at higher temperature $T_m^{ME} \leq T \leq T_c$, we conclude that the positive EFG is induced by the magnetic order as already proposed by e.g. Eibschütz et al. [1967] and Engelke [2010] for pure $FeCr_2S_4$. We assume in this temperature range, that the lower e_g level is $|L_z = 2^s\rangle$ which is separated from the upper level $|L_z = 0\rangle$ by second-order spin-orbit splitting. While the temperature dependence of induced quadrupole splitting could be well fitted for $T > T_m^{ME}$ (Engelke [2010]), the quadrupole splitting is lower than calculated from the change of orbital populations below T_m^{ME}. From this we conclude that below T_m^{ME}, the spin-orbit splitting is reduced and suppresses a further increase of the quadrupole splitting to still higher values as expected from calculation. In the same temperature range we also find reduced values of B_{hf}.

For an explanation we have to consider the action of an additional effect opposing the action of the magnetically induced spin-orbit splitting. As discussed already for pure $FeCr_2S_4$ (Feiner [1981]) the e_g ground state can be split by Jahn-Teller effect. In the present case we have to deal with a so-called ***dynamic pseudo Jahn-Teller effect*** since the degeneracy of the orbital ground state is already lifted by the induced second-order spin-orbit splitting (see Feiner [1981] and Ham [1965]).

The dynamic Jahn-Teller effect involves coupling of vibrational modes to the electronic states leading to so-called ***vibronic states***. In our case this vibronic coupling gives rise to a reduction of a spin-orbit splitting and finally (upon still lower temperature) to a dominance of the Jahn-Teller structural distortion with an orbital ground state that now is $|L_z = 0\rangle$, i.e., the orbital ground states at low temperature become inverted against the situation at high temperature where the ground state was $|L_z = 2^s\rangle$. This gradual change of the energies of orbital levels upon lowering temperature firstly leads to a weaker increase of the positive induced quadrupole splitting than expected for a fixed distance between the two e_g levels.

Then upon inversion of level sequence there will follow a change of sign of the quadrupole splitting (as observed). It should be noted that the local structural distortions due to the Jahn-Teller effect apparently are not of axial symmetry as seen from the appearance of an asymmetry parameter η for the quadrupole interaction. The magnitude of asymmetry parameter η is about 0.55 attributed to the hybridization of Fe-band with Cr as can be later seen from band structure model. Also the distortions appear to be inhomogeneous as seen from the apparent increase of number of subspectra below T_m^{ME} (also seen in pure compound Engelke et al. [2011]).

Peculiar variations in the temperature dependence of parameters of Mössbauer experiments, μSR, and magnetization have been found around very similar temperatures T_m^{ME}, $T_p^{\mu SR}$, and T_m (see Fig. 6.7); we relate these to the onset of Jahn-Teller distortions. While in pure $FeCr_2S_4$ the change of sign of quadrupole interaction occurs very abruptly at $T_{oo} \simeq 10$ K, this change is more continuous in the Cu doped compounds. We infer that in case of pure $FeCr_2S_4$ there occurs a coherent ordering of orbital moments (as traced also from the anomaly in specific heat data (Fig. 4.23)), Whereas this is impeded in the doped compounds by the random disorder in the neighborhood of Fe^{2+} introduced by Cu (see binomial distribution of Cu as discussed in section 6.1).

The onset of Jahn-Teller distortions around the T_m^{ME}, $T_p^{\mu \mathrm{SR}}$, and T_m in the doped and as well in the pure compound therefore should be related to **short-range orbital correlations**, eventually leading to an **orbital glassy ground state** in the doped compounds. In the pure compound the onset of Jahn-Teller effect also affects spin structure with an eventual helical arrangement as proposed by from μSR (see section 4.4). Apparently, this helical spin structure does not change upon orbital ordering below $T_{oo} \simeq 10\ K$ (Kalvius et al. [2008, 2010, 2013]).

Also in the doped compounds we find indications for spin reorientation from magnetization data. In the Mössbauer patterns this becomes, however, only distinctly apparent below T_{og}^{ME} where we find angles between magnetic hyperfine field B_{hf} and principle axes of the electric field gradient ($\theta \simeq \frac{\pi}{2}$ and $\phi \simeq \frac{\pi}{4}$).

At intermediate temperatures between T_m^{ME} and T_{og}^{ME}, there is a gradual change of spin orientation from parallel to c-axis at high temperature to a canted structure turning off from c-axis as traced from magnetization and also from B_{hf}.

As already shown, B_{hf} is reduced below T_m^{ME} from values found at higher temperature. This reduction has its main origin in an increased orbital contribution (opposite to the dominant contact field proportional to $\langle S_z \rangle$). In principle the orbital singlets of e_g have quenched orbital momentum, yet there are admixtures from higher t_{2g} levels via spin-orbit coupling inducing some orbital moment especially when the spins are turning towards the easy a, b plane due to the $|L_z = 0\rangle$ ground state.

By now we have considered the spin and orbital behavior related to Fe^{2+} as derived from the Mössbauer spectral part (comprised in group I) revealing anomalous temperature behavior in quadrupole interaction. We now turn to the group II that shows an increase of the magnetic hyperfine fields below T_m^{ME}. Its broad hyperfine field distribution below T_m^{ME} we attribute to a re-entrant spin glass phase with a wide distribution of the magnetic hyperfine fields B_{hf} and angles of EFG vs B_{hf} as can be seen from the temperature dependence of the line width of Mössbauer spectra and also the relative field width from μSR, e.g. Fig. 5.15 and 5.47.

μSR analyses reveal the coexistence of ferrimagnetic and spin glass states below a certain temperature T$_p$, where rotating signals and dynamical Kubo-Toyabe relaxation (DLKT) are present. The damping rate of DLKT increases continuously down to low temperature and is typical for an insulator spin glass (Uemura [1981]). For describing this situation as probed by Mössbauer spectroscopy and μSR we use a model for the low temperature magnetic structure of $Fe_{1-x}Cu_xCr_2S_4$, which has been proposed for $PbFe_{\frac{1}{2}}Nb_{\frac{1}{2}}O_3$ a complex perovskite (Chillal et al. [2013]) having similarity with the mixed spinel $Mg_{1+t}Fe_{2-2t}Ti_tO_4$ reported by Brand et al. [1985]. The coexistence of the ferrimagnetic and spin glass states occurs in a single homogeneous phase (Gabay and Toulouse [1981]) and is not related to phase separation. The spin arrangement is similar to a '*speromagnetic*' arrangement which means an irregular tilting of ionic moments from the z direction set by ferrimagnetic long range order. Above the re-entrant spin glass temperature T$_p$, the transverse spin components are freely rotating and do not contribute to the thermally average spin. Below this temperature, the transverse spin components start gradually freezing and simultaneously increasing the magnetic moment, i.e., B_{hf} is increasing as observed. The large values of fluctuation rate ν_{KT} and the increase of the DLKT static width a_{KT} on cooling below T$_p$ represent a gradual freezing of spin and finally this process ends up in a complete freezing, i.e., a spin glass state, at low temperature.

Note, that T$_p$ lies close to the T$_m^{ME}$ derived from Mössbauer results, and T$_m$ from magnetization data (see Fig. 6.7): as already discussed this demonstrates that the Jahn-Teller effect, short-range orbital order and spin glass state are competing leading to spin reorientation.

While the temperature dependencies of the μSR precession frequencies show a "Brillouin" behavior in this concentration range, there are different relaxation patterns below and above T$_p$. The DLKT relaxation function below T$_p$ and two damped relaxation functions (slow and fast relaxation rate, λ_s and λ_f) above T$_p$ indicate different spin dynamics.

Above T$_p$, resistivity data show an onset of more metallic behavior (Fritsch et al. [2003]), i.e. it is obvious that T$_p$ (and T$_m$) should be associated with the insulator to metal transition. The slow and fast relaxation components above T$_p$ can be attributed to spatially separated insulating and conducting regions up to T$_c$, respectively (Heffner et al. [2004]). The fast relaxation rate λ_f (conducting regions) for all samples in this concentration range increases sharply up to T$_c$ because of the slowing down of spins near their T$_c$. The decreasing of the slow relaxation rate λ_s near T$_c$ may be attributed to a slowing down of the diffusion of magnetic polarons in the more insulating regions close to T$_c$ (Allodi et al. [2001], Heffner et al. [2004]). The reduction of the relative field width ($\Delta B_\mu/B_\mu^0$) close to T$_c$ found for $x < 0.5$ (e.g. Figs. 5.47 and 5.56) may also be related to a polaron hopping.

6.3

The Concentration Range x $\geqslant$ 0.5

As already discussed, for $x \geqslant 0.5$, the A-tetrahedral sites are occupied with more than 70% by Fe^{3+}. Thus, the short-range orbital ordering becomes suppressed due to the low amount of Fe^{2+}. The temperature dependence of the magnetic hyperfine field of Fe^{3+} has a normal behavior. Only for $x = 0.7$ and $x = 0.8$, we can trace a small contribution from a superparamagnetic fraction. For this concentration range there is no specific information from Mössbauer results. μSR and magnetization data, however, show some peculiar changes. As mentioned already, the Mössbauer spectroscopy is a probe at iron which is not the case for μSR and bulk magnetic measurements. Therefore these changes are supposed to be related to the Cr and eventual Cu sublattices.

The magnetization data, FC and ZFC curves for this concentration range are significantly different from $x < 0.5$. The reduction of ZF curves at low temperature ($T_p \simeq 50$ K - 80 K are attributed to the insulator spin glass phase, which is also seen in μSR data from the dynamical Kubo-Toyabe (DLKT) signal.

The higher temperature transition, denoted as T_k in sections 5.4.5 and 5.4.6, is attributed to a spin reorientation (Kalvius et al. [2013]) supposedly from a collinear to a non-collinear spin structure. This transition around T_k is supported by the observation of a sharp rise in the relative field width and two spontaneous rotation frequencies.

From the ratio of fast and slow relaxation components that for this concentration range are observed over an extended temperature range down to lower temperatures, we can see that samples get more metallic with fast spin fluctuations in the now ferromagnetic regime.

6.4

Conduction Mechanism and CMR Effect

Park et al. [1999] and Fritsch et al. [2003] have described the electronic structure of $Fe_{1-x}Cu_xCr_2S_4$ as half-metallic. In a half-metal, the fully polarized charge carriers form one metallic band and one insulating band.

For $x \leq 0.5$, Fritsch et al. [2003] (and also Palmer and Greaves [1999]) described the electrical conduction of $Fe_{1-x}Cu_xCr_2S_4$ with a triple exchange model. In this model, the Fermi-edge is located between the Fe spin-up e_g-band where spin-up and spin-down e_g-band are split by Jahn-Teller effect and Coulomb correlation effects (supported by band-calculations of Park et al. [1999]). A single electron from Fe^{2+} spin-up e_g band is transferred via a p-orbital of S^{2-} to an empty Cr^{3+} spin-up e_g band. This electron proceeds from the temporary Cr^{2+} to Fe^{3+} spin-up e_g band via a second S^{2-} p-orbital. To explain this model, the formula $Fe^{2+}_{1-2x}Fe^{3+}_xCu^+_xCr^{3+}_2S^{2-}_4$ is introduced (supposed already by Lotgering et al. [1969]), in which the copper is monovalent with a closed d-shell in $3d^{10}$-state (no contribution to the conductivity and band structure picture). Especially, led by our Mössbauer results for Cu doping $x < 0.5$ and discussed in section 6.2, we can adopt the metallic band picture proposed by Fritsch et al. [2003] and also the experimental results from Han et al. [2006][1]. Han et al. [2006] have observed a large hybridization between S 3p state and all 3d orbital of ,Fe, Cr, and Cu, in particular to the Fe 3d-band. Fig. 6.8 shows a schematic view of band picture of $Fe_{1-x}Cu_xCr_2S_4$ for $x \leqslant 0.5$ indicating the large hybridization of S 3p to the broad Fe 3d states and a weak hybridization to the narrow Cu 3d states (Fig. 6.8).

---

[1] by performing photoemission spectroscopy (PES), soft x-ray absorption spectroscopy (XAS), and soft x-ray magnetic circular dichroism (XMCD) measurements using synchrotron radiation.

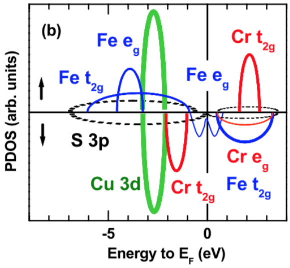

Figure 6.8: A schematic view of band structure of $Fe_{1-x}Cu_xCr_2S_4$ $x \leqslant 0.5$ (adopted from Han et al. [2006]).

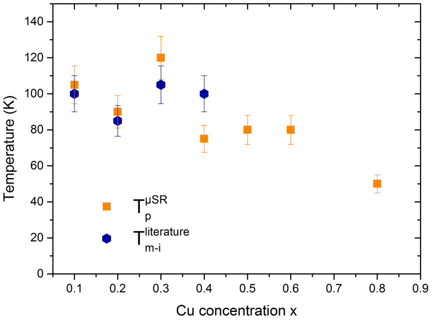

Figure 6.9: Comparison of the temperature related to the insulator to metal transition of μSR results and other literature.

For $x \leqslant 0.5$, the Fe^{2+} spin-down e_g band near E_F splits into two bands due to the Jahn-Teller effect and E_F is located between these two bands. These narrow hybridized e_g bands near the Fermi-edge are responsible for the charge transfer in $Fe_{1-x}Cu_xCr_2S_4$.
μSR results reveal an insulating spin glass at low temperatures below ~ T_p and metallic behavior above that which is in agreement with the previous investigations on electrical resistivity and conduction mechanism reported in section 4.6. The metallic behavior of higher temperature can be understand in the mentioned metallic band structure due to the large hybridization of the e_g band and S^{2-} band. The insulating ground state seen at low temperature appears to be related to the orbital glass by the static cooperative Jahn-Teller effect, which is in agreement with the theories reported in section 4.6. With increasing temperature the system becomes more and more metallic, we can trace the thermal hopping of polarons. As can be seen from Fig. 6.9, the metal-insulator transition temperatures for various x (as taken from literature resistivity data) are in good agreement with the temperature T_p from our μSR data.

As discussed above in section 6.2, the fast and slow relaxing μSR signals can be associated with metallic and insulating regions in the samples. Especially the decreasing of λ_s close to T$_c$ indicates a slowing of magnetic polaron motion near T$_c$ where the samples turn again semiconducting. This is the temperature range where CMR is found. It suggests that the coexistence of the fast and slow relaxation components (conducting and insulating fraction) plays a role for CMR.

Chapter 7

Conclusion

From the discussion of our data we are now able to propose a phase diagram demonstrating the complex interplay of magnetic exchange and orbital effects. In Fig. 7.1, we have plotted the temperatures, for which characteristic changes are observed from Mössbauer, μSR, and magnetization data. We also included those for the undoped compound (Engelke et al. [2011], Kalvius et al. [2013], Tsurkan et al. [2010]).

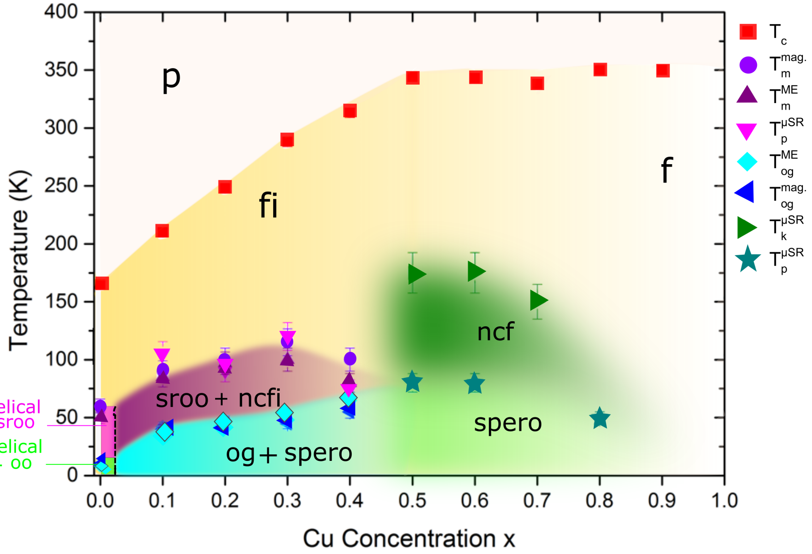

Figure 7.1: Magnetic phase diagram of $Fe_{1-x}Cu_xCr_2S_4$. p= paramagnetic, fi= ferrimagnetic, f= ferromagnetic, sroo= short-range orbital order, ncfi= non-collinear ferrimagnetic, og= orbital glass, spero= speromagnet, oo= coherent orbital order, ncf= non-collinear ferromagnetic.

The magnetic ordering temperatures T_c of our samples are in good agreement with those reported earlier (e.g. Haacke and Beegle [1967] and Tsurkan et al. [2005]). The rise of magnetic hyperfine fields $B_{hf}(T)$, spontaneous muon rotation frequencies $\nu_\mu(T)$, and magnetization $M(T)$ below T_c follow typical magnetization curves for ferrimagnetic compounds (for high Cu doping x, there is a change to ferromagnetic order when the amount of Fe^{2+} becomes negligible).

For $x < 0.5$, where iron is dominantly divalent, we have clear indications for the onset of a dynamic pseudo Jahn-Teller effect acting on the orbital doublet e_g of Fe^{2+}. We can trace this onset from T_m^{ME}, T_m^{mag}, $\mathrm{T}_p^{\mu SR}$ around 70 - 80 K. The Jahn-Teller effect firstly diminishes the magnetically induced spin-orbit splitting of e_g and finally leads to an orbital ground state of $|L_z = 0\rangle$ as also found for $\mathrm{FeCr_2O_4}$ (Hartmann-Boutron and Imbert [1968]). The spin order is no more collinear and we have an onset of short-range orbital correlations.

Also for the undoped compound $\mathrm{FeCr_2S_4}$, there occurs a transition around 50 - 60 K to helical spin order together with short-range orbital order. Upon further lowering temperature there occurs coherent orbital ordering in the pure compound around 10 K. The spin order stays helical (e.g. Kalvius et al. [2010]).

For the Cu-doped compound we find spin-glassy behavior that is similar to a speromagnet below about 40 K. The orbital ground state is not a coherent one, but rather should be an orbital glass.

Both from Mössbauer spectroscopy and μSR we observe clear changes when going to Cu concentrations $x \geqslant 0.5$. Contrary to previous assumptions, that Fe^{2+} vanishes completely for $x \geqslant 0.5$, we can give a better description of our Mössbauer spectra assuming a binomial distribution among nearest tetrahedral neighbor sites with iron staying divalent as long as no, one or two Cu^{+} neighbors are present, and Fe^{3+} for three or four Cu^{+} neighbors.

From μSR we trace a transition around 140-150 K with the appearance of an additional spontaneous frequency and rising static field width. This cannot be detected from Mössbauer spectroscopy. This transition can be related to a spin-reorientation connected with Cr^{3+} and/or Cu^{2+} moments. In this temperature range we also find contributions from gradually freezing, spin-glassy regions. Below about 70 K, we find again static spin-glassy/speromagnetic behavior similar to the lower Cu doping $x < 0.5$ where we could trace the Jahn-Teller distortions at Fe^{2+} from their Mössbauer spectra.

Now for $x \geqslant 0.5$ the origin for the transition in magnetic behavior must be different. In case (as already proposed by Goodenough [1967]), there is present Cu^{2+}, one may speculate that Jahn-Teller effect in the t_{2g} orbitals of Cu^{2+} in tetrahedral coordination can lead to similar effects in the spin system as found for $x < 0.5$ and caused by Fe^{2+}.

From μSR we find for all Cu concentration above $\mathrm{T}_p^{\mu SR}$ up to T_c, contributions with fast and slow longitudinal relaxation, i.e. spin dynamics is present down to low temperatures. The fast and slow signals are related to conducting and insulating parts of the samples. This coexistence of insulating and metallic regions is similar to that found in $\mathrm{(La, Ca)MnO_3}$ (Allodi et al. [2001], Heffner et al. [2004]), a material exhibiting CMR. The CMR detected in $\mathrm{Fe}_{1-x}\mathrm{Cu}_x\mathrm{Cr_2S_4}$ therefore may also be related to regions with different charge and spin dynamics.

In summary, we could show that the complex magnetic behavior of $\mathrm{Fe}_{1-x}\mathrm{Cu}_x\mathrm{Cr_2S_4}$ is related to its intrinsic inhomogeneity caused by random substitution of Cu on Fe tetrahedral spinel sites. Only a negligible quantity of iron is occupying octahedral sites. The interplay between spin and orbital order is related to a dynamic pseudo Jahn-Teller effect acting on the orbital doublet ground state of Fe^{2+}. For $x \geqslant 0.5$ eventually a similar Jahn-Teller effect occurs at Cu^{2+} having an orbital triplet ground state.

For the clarification of the various spin structures and their transitions as derived from our data neutron scattering studies would be desirable.

Appendix A

Mössbauer Spectra

A.1

$Fe_{0.9}Cu_{0.1}Cr_2S_4$

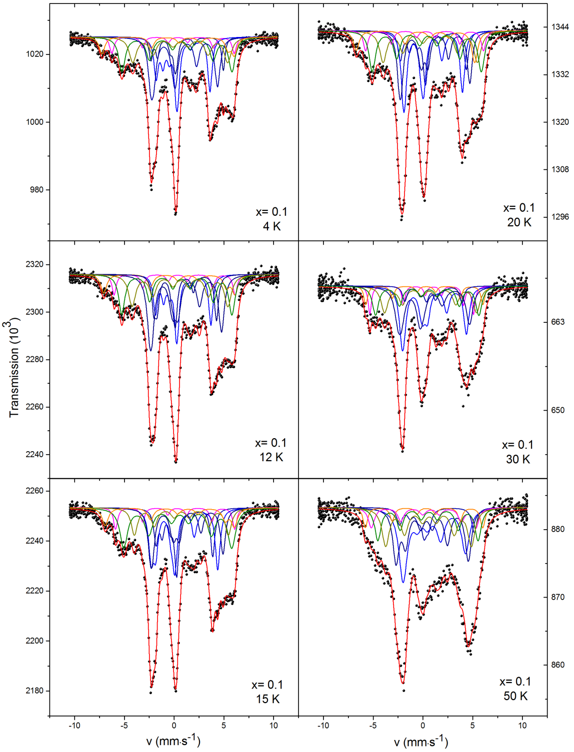

Figure A.1: Mössbauer spectra of the $Fe_{0.9}Cu_{0.1}Cr_2S_4$ ($x = 0.1$) at various temperatures.

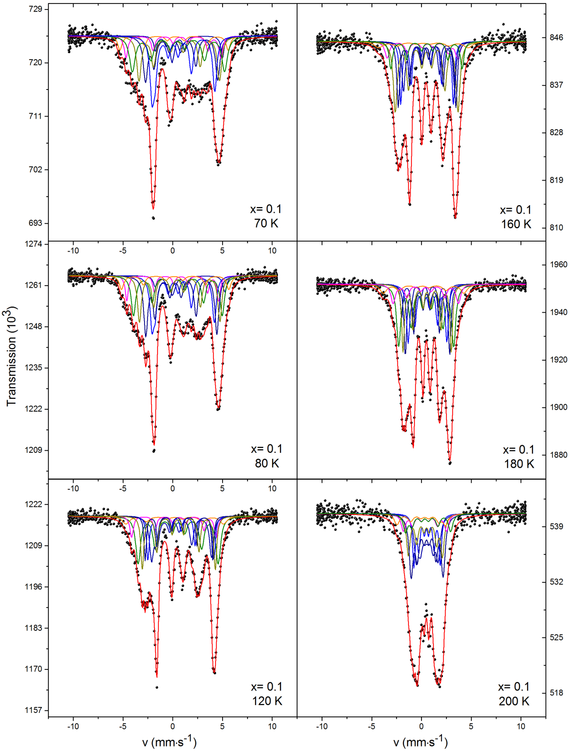

Figure A.2: Mössbauer spectra of the $Fe_{0.9}Cu_{0.1}Cr_2S_4$ (x = 0.1) at various temperatures.

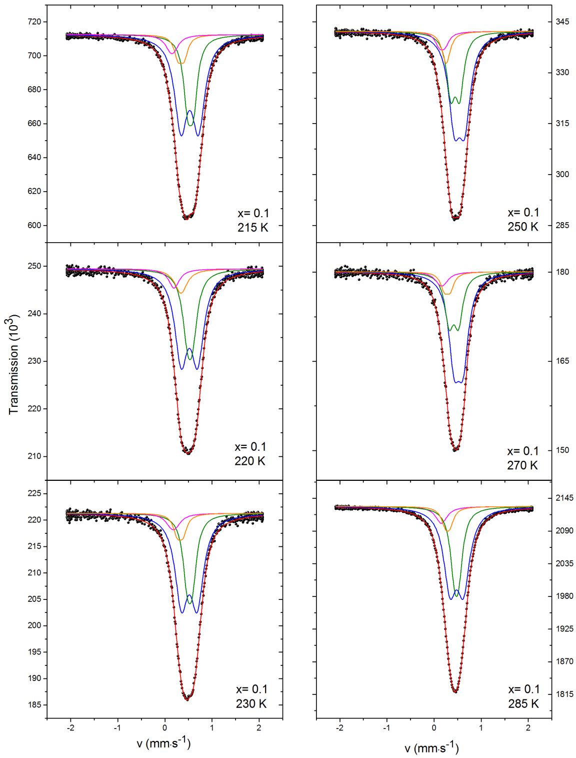

Figure A.3: Mössbauer spectra of the $Fe_{0.9}Cu_{0.1}Cr_2S_4$ (x = 0.1) at various temperatures in paramagnetic phase.

A.2

$Fe_{0.8}Cu_{0.2}Cr_2S_4$

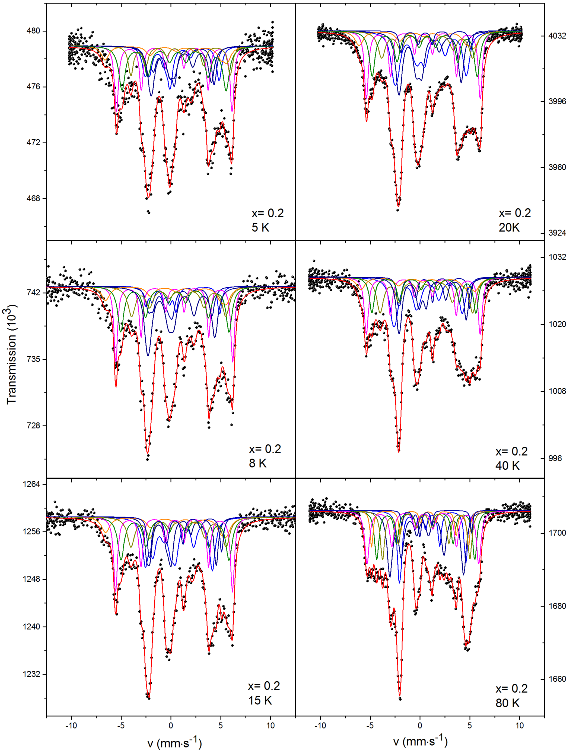

Figure A.4: Mössbauer spectra of the $Fe_{0.8}Cu_{0.2}Cr_2S_4$ ($x = 0.2$) at various temperatures.

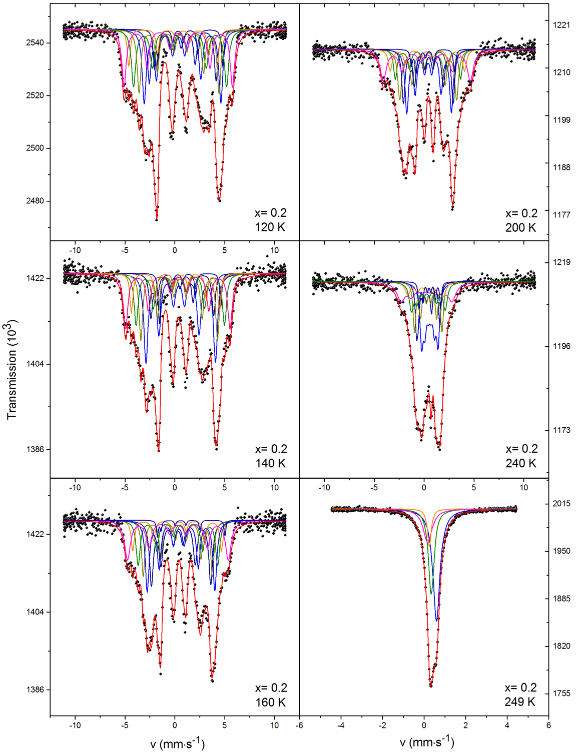

Figure A.5: Mössbauer spectra of the $Fe_{0.8}Cu_{0.2}Cr_2S_4$ ($x = 0.2$) at various temperatures.

T (K)	group of spectra	CS $(\mathrm{mm \cdot s^{-1}})$	QS $(\mathrm{mm \cdot s^{-1}})$	B_{hf} (T)	Area (%)
240	group I	0.562(1)	0.12(1)	6.01(1)	42(2)
	group II	0.494(2)	0.05(1)	9.47(2)	32(1)
	spectrum X	0.356(2)	-0.22(1)	11.05(1)	8(1)
	Fe^{3+}	0.32(3)	0.04(3)	15.86(2)	18(2)
220	group I	0.558(2)	0.05(3)	11.45(4)	43(2)
	group II	0.519(3)	-0.12(3)	14.72(1)	31(1)
	spectrum X	0.40(1)	-0.20(2)	19.01(3)	8(1)
	Fe^{3+}	0.357(1)	-0.14(1)	22.64(4)	18(2)
200	group I	0.558(4)	0.17(1)	14.28(2)	44(5)
	group II	0.523(5)	-0.04(4)	18.64(3)	30(3)
	spectrum X	0.42(4)	-0.03(4)	23.1(1)	8(1)
	Fe^{3+}	0.381(3)	-0.06(1)	27.07(3)	18(2)
180	group I	0.605(1)	0.20(3)	17.73(1)	45(4)
	group II	0.515(4)	-0.19(3)	21.27(2)	30(3)
	spectrum X	0.436(1)	-0.13(5)	26.17(1)	8(1)
	Fe^{3+}	0.41(4)	-0.11(3)	29.52(1)	18(2)
160	group I	0.629(3)	0.30(3)	19.83(3)	43(2)
	group II	0.527(1)	-0.23(1)	23.07(3)	30(1)
	spectrum X	0.456(5)	-0.20(1)	27.61(3)	8(1)
	Fe^{3+}	0.422(5)	-0.02(1)	31.37(2)	18(2)
140	group I	0.627(2)	0.43(1)	20.81(2)	42(2)
	group II	0.583(2)	0.024(3)	25.56(2)	32(1)
	spectrum X	0.477(2)	-0.55(2)	27.40(1)	8(1)
	Fe^{3+}	0.437(3)	-0.09(2)	32.5(4)	18(2)
120	group I	0.689(5)	0.61(4)	22.40(1)	40(2)
	group II	0.596(3)	-0.03(1)	26.96(1)	35(1)
	spectrum X	0.507(1)	-1.01(1)	27.60(3)	8(1)
	Fe^{3+}	0.454(1)	-0.03(3)	33.7(1)	18(2)
100	group I	0.698(1)	0.68(1)	23.03(2)	44(2)
	group II	0.577(4)	-0.07(4)	27.89(3)	30(1)
	spectrum X	0.535(3)	-0.83(2)	29.12(2)	8(1)
	Fe^{3+}	0.454(3)	-0.05(1)	34.44(5)	18(2)
80	group I	0.688(2)	0.90(1)	21.65(2)	43(2)
	group II	0.616(1)	0.18(3)	28.89(4)	31(1)
	spectrum X	0.556(5)	-0.82(5)	30.13(5)	8(1)
	Fe^{3+}	0.457(4)	-0.13(2)	34.78(2)	18(2)
60	group I	0.727(4)	1.28(3)	21.57(2)	42(2)
	group II	0.564(1)	-0.08(1)	29.01(1)	32(1)
	spectrum X	0.563(2)	-0.86(4)	31.83(5)	8(1)
	Fe^{3+}	0.426(1)	-0.06(1)	35.43(2)	18(2)

[h]

Table A.1: Adjusted parameters from some selected Mössbauer spectra of $Fe_{0.8}Cu_{0.2}Cr_2S_4$ in the temperature region between 240 K and 100 K.

T (K)	group of spectra	CS ($mm \cdot s^{-1}$)	QS ($mm \cdot s^{-1}$)	B_{hf} (T)	Area (%)
80	group I	0.688(2)	0.90(1)	21.65(2)	43(2)
	group II	0.616(1)	0.18(3)	28.89(4)	31(1)
	spectrum X	0.556(5)	-0.82(5)	30.13(5)	8(1)
	Fe^{3+}	0.457(4)	-0.13(2)	34.78(2)	18(2)
60	group I	0.727(4)	1.28(3)	21.57(2)	42(2)
	group II	0.564(1)	-0.08(1)	29.01(1)	32(1)
	spectrum X	0.563(2)	-0.86(4)	31.83(5)	8(1)
	Fe^{3+}	0.426(1)	-0.06(1)	35.43(2)	18(2)

Table A.2: Adjusted parameters from some selected Mössbauer spectra of $Fe_{0.8}Cu_{0.2}Cr_2S_4$ in the temperature region between 100 K and 60 K.

T (K)	group of spectra	CS ($mm \cdot s^{-1}$)	QS ($mm \cdot s^{-1}$)	B_{hf} (T)	η	θ (°)	ϕ (°)	Area (%)
40	group I	0.674(2)	-2.91(3)	17.35(2)	0.13(1)	90(1)	55.2(1)	44(2)
	group II	0.737(2)	-0.19(3)	30.29(2)	-	-	-	31(1)
	spectrum X	0.595(3)	-1.39(1)	35.54(1)	-	-	-	8(1)
	Fe^{3+}	0.438(4)	-0.01(2)	35.42(1)	-	-	-	18(2)
20	group I	0.666(1)	-3.24(3)	15.81(1)	0.20(1)	87.7(2)	48(1)	45(2)
	group II	0.759(3)	-0.15(3)	30.79(4)	-	-	-	30(1)
	spectrum X	0.589(1)	-1.65(2)	35.8(1)	-	-	-	8(1)
	Fe^{3+}	0.449(3)	-0.01(1)	35.42(2)	-	-	-	18(2)
15	group I	0.702(5)	-3.28(1)	15.46(1)	0.22(2)	82.9(2)	47.1(2)	44(2)
	group II	0.714(1)	-0.093(2)	31.90(2)	-	-	-	30(1)
	spectrum X	0.590(3)	-1.96(3)	37.60(3)	-	-	-	8(1)
	Fe^{3+}	0.454(2)	-0.07(1)	36.38(3)	-	-	-	18(2)
8	group I	0.690(2)	-3.01(1)	15.71(2)	0.37(1)	90(1)	40.7(1)	42(2)
	group II	0.673(8)	-0.035(2)	31.79(4)	-	-	-	32(1)
	spectrum X	0.592(3)	-1.95(5)	37.63(3)	-	-	-	8(1)
	Fe^{3+}	0.469(3)	-0.07(1)	36.41(2)	-	-	-	18(2)
5	group I	0.653(3)	-2.919(1)	15.28(7)	0.52(3)	90(1)	56.5(2)	43(3)
	group II	0.669(5)	-0.042(1)	31.89(2)	-	-	-	31(2)
	spectrum X	0.591(2)	-1.94(2)	37.95(3)	-	-	-	8(1)
	Fe^{3+}	0.465(1)	-0.05(2)	36.01(2)	-	-	-	18(2)

Table A.3: Adjusted parameters from some selected Mössbauer spectra of $Fe_{0.8}Cu_{0.2}Cr_2S_4$ for temperatures below 60 K.

A.3

$Fe_{0.7}Cu_{0.3}Cr_2S_4$

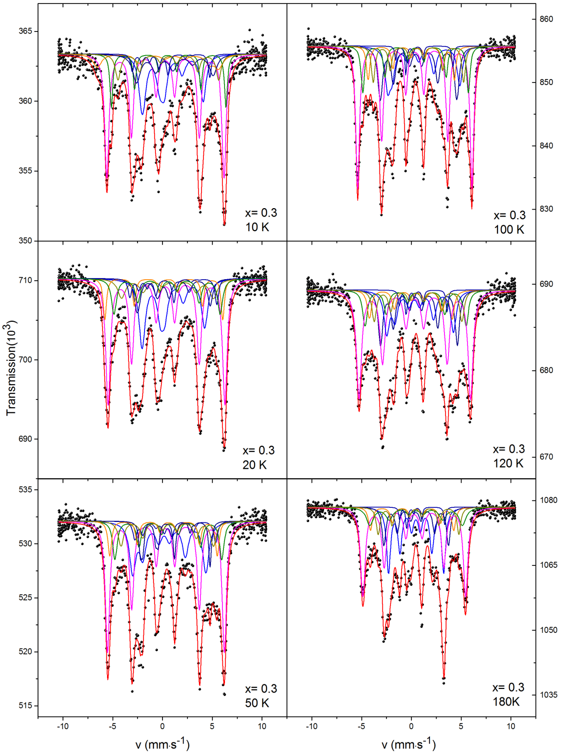

Figure A.6: Mössbauer spectra of the $Fe_{0.7}Cu_{0.3}Cr_2S_4$ (x = 0.3) at various temperatures.

T (K)	Assignment	CS (mm · s^{-1})	*QS* (mm · s^{-1})	HWHM (mm · s^{-1})	Area (%)
290	Fe^{2+}	0.445(8)	0.234(4)	0.14(1)	36(2)
	Fe^{2+}	0.434(9)	0.001	0.14(4)	20(2)
	Fe^{3+}	0.223(4)	0.12(3)	0.14(3)	36(3)
	spectrum *X*	0.251(3)	0.01(3)	0.12(3)	8(1)

Table A.4: The adjusted parameters from Mössbauer spectra of $Fe_{0.7}Cu_{0.3}Cr_2S_4$ at 290 K in paramagnetic regime.

T (K)	group of spectra	CS ($mm \cdot s^{-1}$)	QS ($mm \cdot s^{-1}$)	B_{hf} (T)	Area (%)
250	group I	0.612(1)	0.55(2)	8.23(1)	38(3)
	group II	0.570(2)	0.23(1)	13.80(2)	20(2)
	spectrum X	0.386(2)	-0.71(2)	18.21(1)	8(1)
	Fe^{3+}	0.342(1)	0.07(2)	23.62(1)	36(2)
200	group I	0.593(2)	0.54(1)	14.50(2)	38(1)
	group II	0.556(1)	0.29(1)	25.11(3)	20(2)
	spectrum X	0.386(2)	-0.3(3)	23.5(1)	8(1)
	Fe^{3+}	0.381(1)	0.02(1)	30.5(1)	36(2)
180	group I	0.588(3)	0.14(1)	17.77(3)	38(2)
	group II	0.618(2)	0.15(1)	27.18(2)	20(1)
	spectrum X	0.399(5)	-0.44(1)	25.64(1)	8(1)
	Fe^{3+}	0.384(1)	0.03(1)	32.04(2)	36(2)
150	group I	0.607(2)	0.33(2)	20.07(2)	38(2)
	group II	0.599(1)	0.02(1)	28.68(2)	20(1)
	spectrum X	0.404(1)	-0.25(2)	26.77(1)	8(1)
	Fe^{3+}	0.414(1)	0.03(2)	33.65(2)	36(2)
120	group I	0.705(2)	0.55(1)	21.62(2)	35(2)
	group II	0.594(1)	0.09(1)	26.61(1)	20(1)
	spectrum X	0.42(1)	-0.75(2)	25.78(2)	8(1)
	Fe^{3+}	0.450(2)	0.01(2)	34.74(1)	36(2)
100	group I	0.757(2)	0.81(1)	22.27(1)	37(2)
	group II	0.610(2)	0.09(2)	30.76(3)	20(1)
	spectrum X	0.429(1)	-0.67(2)	26.86(2)	8(1)
	Fe^{3+}	0.449(1)	0.01(1)	35.57(5)	36(2)
90	group I	0.716(1)	0.77(1)	22.58(2)	35(3)
	group II	0.659(2)	0.05(3)	31.01(4)	20(1)
	spectrum X	0.441(1)	-0.41(1)	27.73(2)	8(1)
	Fe^{3+}	0.452(3)	0.01(1)	35.63(2)	36(2)
50	group I	0.614(1)	1.13(1)	21.56(2)	33(2)
	group II	0.737(2)	-0.06(1)	31.14(1)	24(1)
	spectrum X	0.454(2)	-0.5(4)	33.46(5)	8(1)
	Fe^{3+}	0.424(1)	0.06(1)	36.4(2)	36(2)

Table A.5: Adjusted parameters from some selected Mössbauer spectra of $Fe_{0.7}Cu_{0.3}Cr_2S_4$ in the temperature region between 290 K and 50 K.

T (K)	group of spectra	CS ($\mathrm{mm \cdot s^{-1}}$)	QS ($\mathrm{mm \cdot s^{-1}}$)	B_{hf} (T)	η	θ (°)	ϕ (°)	Area (%)
20	group I	0.692(2)	-3.35(2)	15.68(1)	0.3(2)	87(2)	66.9(4)	35(1)
	group II	0.675(1)	-0.17(1)	31.06(2)	-	-	-	20(3)
	spectrum X	0.466(3)	-0.46(3)	36.74(3)	-	-	-	8(1)
	Fe^{3+}	0.453(3)	0.11(1)	36.4(3)	-	-	-	36(3)
10	group I	0.675(2)	-3.39(2)	15.21(2)	0.33(2)	88(1)	47.6(1)	37(3)
	group II	0.692(8)	0.042(2)	33.73(4)	-	-	-	20(1)
	spectrum X	0.475(1)	-1.65(5)	37.82(1)	-	-	-	8(1)
	Fe^{3+}	0.444(1)	0.02(1)	36.7(2)	-	-	-	36(2)
4	group I	0.675(1)	-3.2(1)	15.74(2)	0.39(3)	86.1(1)	52.2(1)	36(3)
	group II	0.634(1)	0.055(1)	33.15(3)	-	-	-	20(2)
	spectrum X	0.473(2)	-1.76(2)	37.64(3)	-	-	-	8(1)
	Fe^{3+}	0.453(4)	0.02(2)	36.8(1)	-	-	-	36(2)

Table A.6: Adjusted parameters from some selected Mössbauer spectra of $Fe_{0.7}Cu_{0.3}Cr_2S_4$ for temperatures below 50 K.

A.4

$Fe_{0.6}Cu_{0.4}Cr_2S_4$

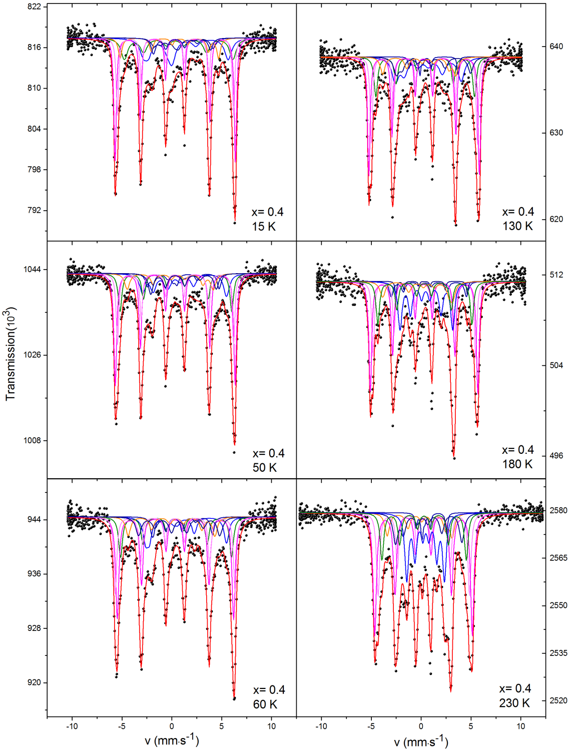

Figure A.7: Mössbauer spectra of the $Fe_{0.6}Cu_{0.4}Cr_2S_4$ ($x = 0.4$) at various temperatures.

T (K)	Assignment	CS $(\mathrm{mm \cdot s^{-1}})$	QS $(\mathrm{mm \cdot s^{-1}})$	HWHM $(\mathrm{mm \cdot s^{-1}})$	Area (%)
320	Fe^{2+}	0.267(2)	0.394(2)	0.13(1)	30(1)
	Fe^{2+}	0.343(2)	0.004(1)	0.13(1)	12(1)
	Fe^{3+}	0.236(2)	0.09(1)	0.17(1)	50(2)
	spectrum X	0.287(1)	-0.68(1)	0.10(3)	8(1)

Table A.7: Adjusted parameters from Mössbauer spectra of $\mathrm{Fe_{0.6}Cu_{0.4}Cr_2S_4}$ at 320 K in paramagnetic regime.

T (K)	group of spectra	CS $(\mathrm{mm \cdot s^{-1}})$	QS $(\mathrm{mm \cdot s^{-1}})$	B_{hf} (T)	Area (%)
295	group I	0.467(1)	0.29(2)	5.45(1)	24(3)
	group II	0.266(2)	-0.08(1)	11.52(2)	19(2)
	spectrum X	0.302(2)	-0.1(2)	14.45(1)	8(1)
	Fe^{3+}	0.301(1)	-0.08(2)	19.37(1)	31(2)
	Fe^{3+}	0.411(4)	0.06(2)	16.88(1)	19(2)
250	group I	0.491(2)	0.38(1)	11.75(2)	29(1)
	group II	0.260(1)	0.01(1)	24.25(3)	13(2)
	spectrum X	0.309(2)	-0.54(3)	18.3(1)	8(1)
	Fe^{3+}	0.320(1)	0.02(1)	38.5(1)	31(2)
	Fe^{3+}	0.430(4)	0.02(2)	26.33(1)	19(2)
230	group I	0.484(1)	0.29(2)	14.20(1)	31(3)
	group II	0.295(3)	0.01(1)	26.23(3)	12(2)
	spectrum X	0.320(5)	-0.72(1)	20.22(1)	8(1)
	Fe^{3+}	0.333(3)	0.01(1)	30.03(2)	30(3)
	Fe^{3+}	0.443(1)	0.01(3)	28.42(1)	19(1)
180	group I	0.523(3)	0.33(1)	18.38(1)	27(3)
	group II	0.330(1)	0.08(1)	29.24(2)	15(1)
	spectrum X	0.325(1)	-1.14(2)	21.76(2)	8(1)
	Fe^{3+}	0.380(2)	0.03(3)	33.44(2)	30(2)
	Fe^{3+}	0.490(3)	0.05(3)	31.92(1)	19(2)
130	group I	0.589(2)	0.81(1)	20.41(2)	28(2)
	group II	0.379(2)	0.04(2)	30.69(2)	14(1)
	spectrum X	0.348(1)	-0.87(2)	22.69(3)	8(1)
	Fe^{3+}	0.396(2)	0.02(1)	34.33(1)	29(2)
	Fe^{3+}	0.506(1)	0.03(2)	33.01(1)	21(2)
80	group I	0.717(2)	1.52(2)	21.01(1)	27(2)
	group II	0.346(3)	0.07(1)	33.89(2)	15(3)
	spectrum X	0.340(1)	-0.86(2)	26.03(2)	8(1)
	Fe^{3+}	0.427(1)	0.01(3)	36.84(5)	31(3)
	Fe^{3+}	0.537(2)	0.05(2)	35.74(1)	20(2)

Table A.8: Adjusted parameters from some selected Mössbauer spectra of $\mathrm{Fe_{0.6}Cu_{0.4}Cr_2S_4}$ in the temperature region between 295 K and 80 K.

T (K)	group of spectra	CS ($mm \cdot s^{-1}$)	QS ($mm \cdot s^{-1}$)	B_{hf} (T)	η	θ (°)	ϕ (°)	Area (%)
60	group I	0.703(3)	-3.08(1)	18.26(2)	0.74(1)	75(2)	72.5(1)	29(1)
	group II	0.370(2)	0.09(2)	34.5(2)	-	-	-	14(3)
	spectrum X	0.344(2)	-0.57(2)	26.95(2)	-	-	-	8(1)
	Fe^{3+}	0.429(2)	0.02(2)	37.3(1)	-	-	-	30(3)
	Fe^{3+}	0.539(1)	0.02(3)	36.20(3)	-	-	-	19(2)
50	group I	0.724(2)	-3.14(1)	18.28(1)	0.64(3)	86(1)	63.9(2)	28(1)
	group II	0.40(1)	0.01(3)	34.75(4)	-	-	-	14(1)
	spectrum X	0.348(2)	-0.79(2)	26.82(3)	-	-	-	8(1)
	Fe^{3+}	0.436(2)	0.01(3)	37.34(3)	-	-	-	31(2)
	Fe^{3+}	0.546(1)	0.06(1)	36.14(2)	-	-	-	19(2)
30	group I	0.706(3)	-3.32(2)	16.87(1)	0.55(2)	74.1(1)	74.1(3)	30(3)
	group II	0.554(3)	0.16(3)	33.01(3)	-	-	-	14(2)
	spectrum X	0.353(3)	-0.95(1)	30.44(1)	-	-	-	8(1)
	Fe^{3+}	0.431(2)	0.018(1)	37.1(2)	-	-	-	30(2)
	Fe^{3+}	0.541(3)	0.02(3)	35.89(1)	-	-	-	19(2)
20	group I	0.742(2)	-3.48(2)	16.45(3)	0.38(1)	84.5(1)	69.4(1)	33(2)
	group II	0.458(3)	0.25(2)	33.84(3)	-	-	-	11(3)
	spectrum X	0.369(3)	-0.97(3)	30.9(1)	-	-	-	8(1)
	Fe^{3+}	0.428(1)	0.014(1)	37.15(3)	-	-	-	29(2)
	Fe^{3+}	0.537(2)	0.05(2)	36.10(3)	-	-	-	20(2)
15	group I	0.726(3)	-3.33(2)	16.57(1)	0.59(1)	87.2(1)	73.3(3)	28(1)
	group II	0.499(2)	0.33(2)	34.3(3)	-	-	-	15(1)
	spectrum X	0.381(2)	-1.01(1)	30.85(2)	-	-	-	8(1)
	Fe^{3+}	0.433(1)	0.02(2)	37.38(2)	-	-	-	31(2)
	Fe^{3+}	0.443(2)	0.07(1)	36.01(2)	-	-	-	19(2)
5	group I	0.719(2)	-3.21(4)	16.05(3)	0.71(1)	77.2(1)	71.4(2)	29(2)
	group II	0.558(1)	0.11(3)	35.4(3)	-	-	-	14(2)
	spectrum X	0.380(1)	-1.39(2)	33.53(1)	-	-	-	8(1)
	Fe^{3+}	0.453(2)	0.01(1)	37.7(2)	-	-	-	29(2)
	Fe^{3+}	0.563(1)	0.08(1)	36.33(1)	-	-	-	20(2)

Table A.9: Adjusted parameters from some selected Mössbauer spectra of $Fe_{0.6}Cu_{0.4}Cr_2S_4$ for temperatures below 80 K.

A.5

$Fe_{0.5}Cu_{0.5}Cr_2S_4$

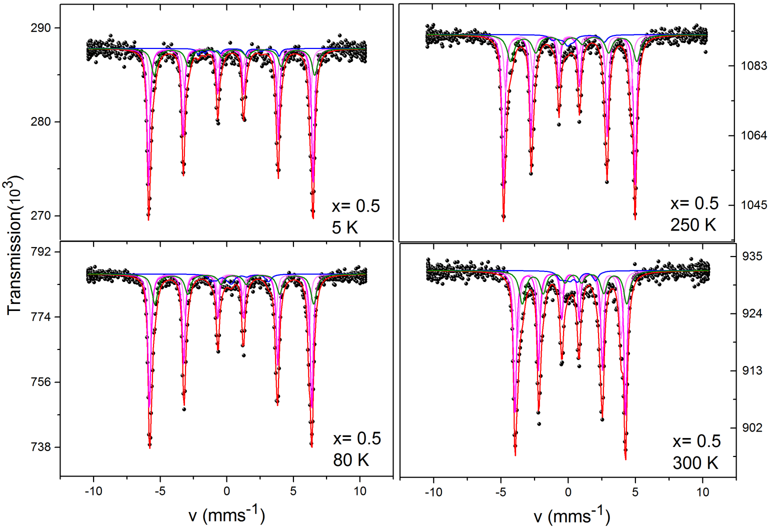

Figure A.8: Mössbauer spectra of the $Fe_{0.5}Cu_{0.5}Cr_2S_4$ ($x = 0.5$) at various temperatures.

T (K)	Assignment	CS ($mm \cdot s^{-1}$)	*QS* ($mm \cdot s^{-1}$)	HWHM ($mm \cdot s^{-1}$)	Area (%)
350	Fe^{2+}	0.222(3)	0.099(1)	0.16(2)	28(1)
	Fe^{3+}	0.130(3)	0.093(2)	0.15(1)	72(1)

Table A.10: The adjusted parameters from Mössbauer spectra of $Fe_{0.5}Cu_{0.5}Cr_2S_4$ at 350 K in paramagnetic regime.

T (K)	group of spectra	CS ($mm \cdot s^{-1}$)	QS ($mm \cdot s^{-1}$)	B_{hf} (T)	Area (%)
300	Fe^{2+}	0.565(2)	1.59(2)	4.15(1)	6(1)
	Fe^{2+}	0.405(3)	0.09(1)	24.10(2)	22(1)
	Fe^{3+}	0.266(1)	-0.01(3)	25.48(1)	45(2)
	Fe^{3+}	0.218(2)	-0.06(1)	23.87(1)	27(2)
250	Fe^{2+}	0.585(3)	1.73(1)	8(2)	5(1)
	Fe^{2+}	0.425(2)	0.11(1)	29.15(3)	21(1)
	Fe^{3+}	0.297(1)	0.002(3)	30.44(1)	50(2)
	Fe^{3+}	0.256(1)	-0.06(1)	28.92(1)	24(2)
200	Fe^{2+}	0.627(2)	1.92(2)	8.77(1)	5(1)
	Fe^{2+}	0.456(1)	0.10(1)	32.80(3)	21(1)
	Fe^{3+}	0.333(3)	-0.01(3)	33.90(2)	52(2)
	Fe^{3+}	0.305(1)	-0.03(2)	32.51(1)	22(2)
150	Fe^{2+}	0.656(1)	2.01(1)	8.8(1)	5(1)
	Fe^{2+}	0.485(2)	0.07(1)	35.15(2)	21(1)
	Fe^{3+}	0.360(2)	0.002(5)	36.10(2)	49(2)
	Fe^{3+}	0.335(1)	-0.03(4)	34.86(1)	26(2)
80	Fe^{2+}	0.666(3)	2.46(1)	8.14(2)	7(1)
	Fe^{2+}	0.536(2)	0.05(2)	37.02(2)	22(1)
	Fe^{3+}	0.395(2)	-0.003(5)	37.82(1)	49(2)
	Fe^{3+}	0.370(3)	-0.01(3)	36.72(1)	23(2)

Table A.11: Adjusted parameters from some selected Mössbauer spectra of $Fe_{0.5}Cu_{0.5}Cr_2S_4$ in the temperature region between 300 K and 80 K.

T (K)	group of spectra	CS ($mm \cdot s^{-1}$)	QS ($mm \cdot s^{-1}$)	B_{hf} (T)	η	θ (°)	ϕ (°)	Area (%)
60	Fe^{2+}	0.671(3)	-2.64(1)	10.50(4)	0.8(3)	90(1)	90(1)	7(2)
	Fe^{2+}	0.536(1)	-0.03(2)	37.1(2)	-	-	-	22(3)
	Fe^{3+}	0.416(2)	0.02(3)	37.71(3)	-	-	-	46(2)
	Fe^{3+}	0.351(3)	-0.06(2)	37.49(3)	-	-	-	26(2)
20	Fe^{2+}	0.679(1)	-3.61(3)	9.24(2)	0.5(2)	86(1)	71(1)	5(1)
	Fe^{2+}	0.555(3)	-0.01(3)	37.02(1)	-	-	-	22(1)
	Fe^{3+}	0.397(1)	0.002(4)	37.84(2)	-	-	-	55(2)
	Fe^{3+}	0.358(1)	0.002(1)	36.75(2)	-	-	-	18(2)
5	Fe^{2+}	0.679(1)	-3.44(1)	10.01(2)	0.8(3)	90(1)	45(1)	4(2)
	Fe^{2+}	0.562(2)	-0.02(4)	37.4(4)	-	-	-	22(2)
	Fe^{3+}	0.403(2)	0.01(3)	38.3(2)	-	-	-	51(2)
	Fe^{3+}	0.373(2)	-0.01(1)	37.2(1)	-	-	-	24(2)

Table A.12: Adjusted parameters from some selected Mössbauer spectra of $Fe_{0.5}Cu_{0.5}Cr_2S_4$ for temperatures below 80 K.

A.6

$Fe_{0.4}Cu_{0.6}Cr_2S_4$

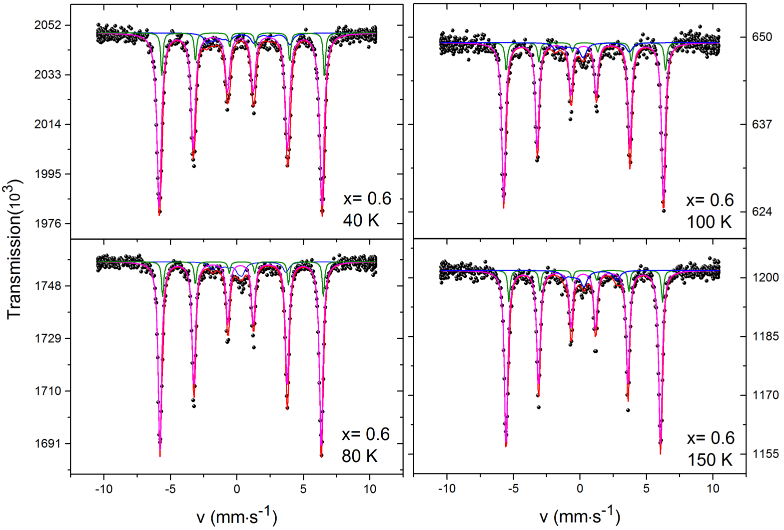

Figure A.9: Mössbauer spectra of the $Fe_{0.4}Cu_{0.6}Cr_2S_4$ ($x = 0.5$) at various temperatures.

T (K)	Assignment	CS (mm · s^{-1})	*QS* (mm · s^{-1})	HWHM (mm · s^{-1})	Area (%)
350	Fe^{2+}	0.273(2)	0.02(4)	0.14(2)	18(1)
	Fe^{3+}	0.129(1)	0.094(1)	0.14(1)	82(1)

Table A.13: Adjusted parameters from Mössbauer spectra of $Fe_{0.4}Cu_{0.6}Cr_2S_4$ at 350 K in paramagnetic regime.

T (K)	group of spectra	CS $(\mathrm{mm}\cdot\mathrm{s}^{-1})$	QS $(\mathrm{mm}\cdot\mathrm{s}^{-1})$	B_{hf} (T)	Area (%)
290	Fe^{2+}	0.566(1)	0.25(2)	2.79(1)	8(1)
	Fe^{2+}	0.42(4)	0.15(1)	25.46(1)	10(1)
	Fe^{3+}	0.292(3)	-0.001(2)	25.88(1)	82(1)
250	Fe^{2+}	0.596(1)	1.09(1)	5.8(1)	8(1)
	Fe^{2+}	0.448(1)	0.14(1)	30.03(2)	10(1)
	Fe^{3+}	0.292(3)	0.002(1)	30.40(3)	82(1)
200	Fe^{2+}	0.625(1)	1.2(2)	7.75(2)	8(1)
	Fe^{2+}	0.46(1)	0.08(1)	33.60(1)	10(1)
	Fe^{3+}	0.319(2)	-0.001(4)	33.80(4)	82(1)
150	Fe^{2+}	0.652(3)	2.03(1)	9.52(3)	8(1)
	Fe^{2+}	0.493(2)	0.09(1)	35.61(3)	10(1)
	Fe^{3+}	0.354(1)	0.002(1)	36.01(3)	82(1)
100	Fe^{2+}	0.688(1)	2.86(1)	10.60(1)	8(1)
	Fe^{2+}	0.522(2)	0.06(2)	37.15(1)	10(1)
	Fe^{3+}	0.378(1)	-0.002(1)	37.27(1)	82(1)

Table A.14: Adjusted parameters from some selected Mössbauer spectra of $Fe_{0.4}Cu_{0.6}Cr_2S_4$ in the temperature region between 290 K and 100 K.

T (K)	group of spectra	CS $(\mathrm{mm}\cdot\mathrm{s}^{-1})$	QS $(\mathrm{mm}\cdot\mathrm{s}^{-1})$	B_{hf} (T)	η	θ (°)	ϕ (°)	Area (%)
80	Fe^{2+}	0.700(3)	-2.92(4)	10.23(2)	0.5(3)	90(1)	69(1)	8(2)
	Fe^{2+}	0.530(1)	0.08(1)	37.48(1)	-	-	-	10(3)
	Fe^{3+}	0.384(1)	0.001(1)	37.62(4)	-	-	-	82(1)
40	Fe^{2+}	0.725(1)	-3.60(3)	10.01(3)	0.7(2)	80(1)	58(1)	8(1)
	Fe^{2+}	0.556(3)	0.04(3)	37.93(4)	-	-	-	10(1)
	Fe^{3+}	0.377(1)	0.01(2)	37.96(1)	-	-	-	82(1)
20	Fe^{2+}	0.739(1)	-4.12(3)	11.31(4)	0.7(3)	90(1)	69(1)	8(2)
	Fe^{2+}	0.566(2)	0.04(2)	37.71(1)	-	-	-	10(2)
	Fe^{3+}	0.399(1)	0.002(1)	38.01(4)	-	-	-	82(1)

Table A.15: Adjusted parameters from some selected Mössbauer spectra of $Fe_{0.4}Cu_{0.6}Cr_2S_4$ for temperatures below 100 K.

A.7

$Fe_{0.3}Cu_{0.7}Cr_2S_4$

T (K)	Assignment	CS ($mm \cdot s^{-1}$)	QS ($mm \cdot s^{-1}$)	HWHM ($mm \cdot s^{-1}$)	Area (%)
355	Fe^{2+}	0.258(1)	0.136(1)	0.11(4)	12(2)
	Fe^{3+}	0.131(4)	0.11(4)	0.14(1)	88(1)

Table A.16: Adjusted parameters from Mössbauer spectra of $Fe_{0.3}Cu_{0.7}Cr_2S_4$ at 355 K in paramagnetic regime.

T (K)	group of spectra	CS ($mm \cdot s^{-1}$)	QS ($mm \cdot s^{-1}$)	B_{hf} (T)	Area (%)
300	Fe^{2+}	0.556(1)	0.15(2)	3.98(1)	11(1)
	Fe^{3+}	0.284(3)	0.001(1)	24.93(1)	46(1)
	Fe^{3+}	0.273(4)	0.02(1)	22.28(1)	28(1)
	Fe^{3+}	0.276(1)	0.001(3)	23.87(1)	16(1)
200	Fe^{2+}	0.660(4)	1.8(2)	5.05(1)	11(1)
	Fe^{3+}	0.342(3)	0.01(1)	33.96(1)	59(1)
	Fe^{3+}	0.347(1)	-0.01(3)	32.20(1)	17(1)
	Fe^{3+}	0.363(4)	-0.003(1)	33.29(1)	14(1)
100	Fe^{2+}	0.675(1)	2.34(1)	10.02(4)	10(1)
	Fe^{3+}	0.453(4)	-0.002(2)	37.36(3)	47(1)
	Fe^{3+}	0.338(1)	-0.01(1)	37.40(2)	29(1)
	Fe^{3+}	0.398(1)	-0.002(1)	36.1(3)	15(1)
20	Fe^{2+}	0.685(1)	3.17(1)	11.01(3)	10(1)
	Fe^{3+}	0.456(1)	0.02(1)	36.37(1)	53(1)
	Fe^{3+}	0.343(4)	0.01(1)	38.32(3)	21(1)
	Fe^{3+}	0.431(4)	0.03(1)	37.20(4)	15(1)

Table A.17: Adjusted parameters from some selected Mössbauer spectra of $Fe_{0.3}Cu_{0.7}Cr_2S_4$ in the temperature region between 300 K and 20 K.

A.8

$Fe_{0.2}Cu_{0.8}Cr_2S_4$

T (K)	Assignment	CS (mm · s^{-1})	*QS* (mm · s^{-1})	HWHM (mm · s^{-1})	Area (%)
355	Fe^{2+}	0.26(1)	0.06(1)	0.10(4)	7(2)
	Fe^{3+}	0.135(1)	0.11(4)	0.12(2)	58(1)
	Fe^{3+}	0.139(1)	0.42(2)	0.14(1)	35(1)

Table A.18: Adjusted parameters from Mössbauer spectra of $Fe_{0.2}Cu_{0.8}Cr_2S_4$ at 355 K in paramagnetic regime.

T (K)	group of spectra	CS (mm · s^{-1})	*QS* (mm · s^{-1})	B_{hf} (T)	Area (%)
300	Fe^{2+}	0.431(5)	0.40(5)	1.71(4)	9(1)
	Fe^{3+}	0.257(3)	0.04(1)	21.01(3)	29(1)
	Fe^{3+}	0.279(1)	-0.05(1)	23.70(3)	32(1)
	Fe^{3+}	0.197(1)	0.71(4)	0.73(3)	31(1)
120	Fe^{2+}	0.567(1)	1.05(1)	3.11(4)	9(1)
	Fe^{3+}	0.389(3)	0.04(1)	35.50(2)	16(1)
	Fe^{3+}	0.384(3)	0.001(2)	36.67(1)	42(1)
	Fe^{3+}	0.350(3)	0.15(1)	19.62(3)	32(1)
80	Fe^{2+}	0.589(2)	1.93(3)	6.70(3)	9(1)
	Fe^{3+}	0.398(3)	0.04(1)	36.22(2)	16(1)
	Fe^{3+}	0.406(1)	0.02(1)	37.18(1)	45(1)
	Fe^{3+}	0.362(2)	0.16(1)	20.44(1)	31(1)
50	Fe^{2+}	0.622(4)	1.94(1)	7.30(3)	9(1)
	Fe^{3+}	0.422(4)	0.001(2)	36.71(3)	26(1)
	Fe^{3+}	0.394(2)	0.03(1)	37.82(3)	36(1)
	Fe^{3+}	0.387(1)	0.25(1)	20.45(1)	29(1)
20	Fe^{2+}	0.636(1)	1.91(4)	8.40(2)	9(1)
	Fe^{3+}	0.407(1)	0.03(1)	36.80(3)	22(1)
	Fe^{3+}	0.412(2)	-0.01(2)	38.01(2)	44(1)
	Fe^{3+}	0.383(2)	0.31(3)	21.42(2)	27(1)

Table A.19: Adjusted parameters from some selected Mössbauer spectra of $Fe_{0.2}Cu_{0.8}Cr_2S_4$ in the temperature region between 300 K and 20 K.

Appendix B

μSR Spectra

B.1

$Fe_{0.9}Cu_{0.1}Cr_2S_4$

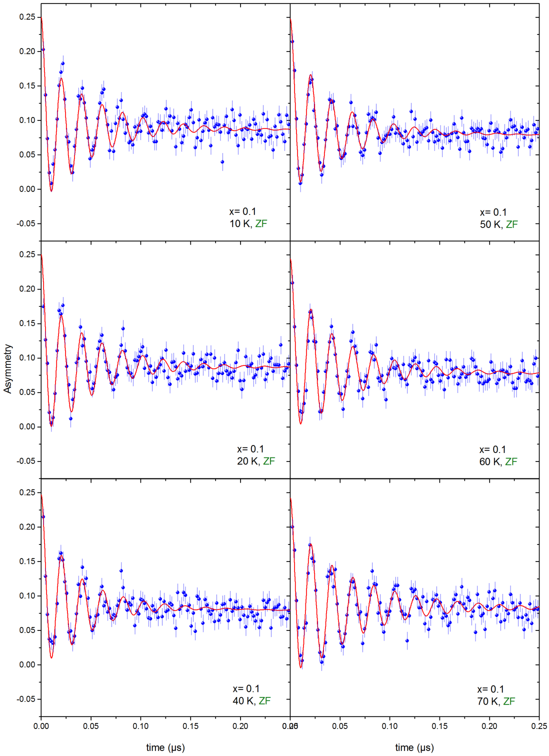

Figure B.1: Zero field μSR spectra of the $Fe_{0.9}Cu_{0.1}Cr_2S_4$ ($x = 0.1$) at various temperatures.

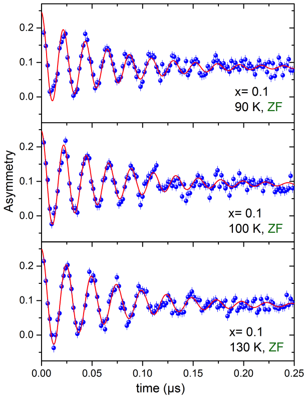

Figure B.2: Zero field μSR spectra of the $Fe_{0.9}Cu_{0.1}Cr_2S_4$ (x = 0.1) at various temperatures.

B.2

$Fe_{0.8}Cu_{0.2}Cr_2S_4$

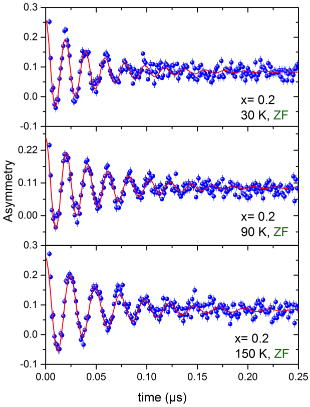

Figure B.3: Zero field μSR spectra of the $Fe_{0.8}Cu_{0.2}Cr_2S_4$ (x = 0.2) at various temperatures.

B.3

$Fe_{0.6}Cu_{0.4}Cr_2S_4$

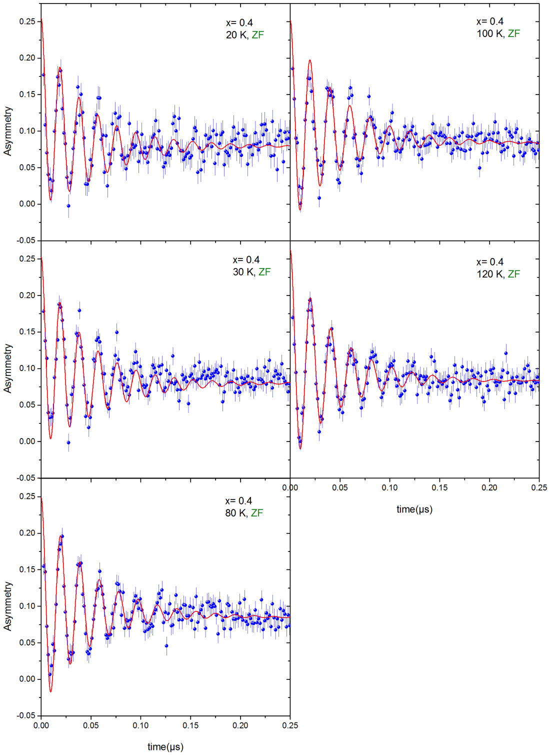

Figure B.4: Zero field μSR spectra of the $Fe_{0.6}Cu_{0.4}Cr_2S_4$ ($x = 0.4$) at various temperatures.

B.4

$Fe_{0.5}Cu_{0.5}Cr_2S_4$

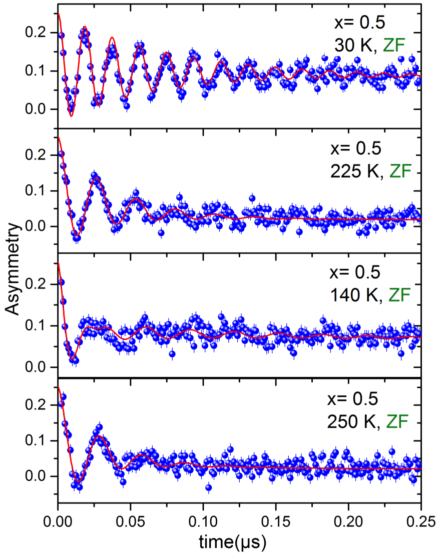

Figure B.5: Zero field μSR spectra of the $Fe_{0.5}Cu_{0.5}Cr_2S_4$ ($x = 0.5$) at various temperatures.

B.5

$Fe_{0.2}Cu_{0.8}Cr_2S_4$

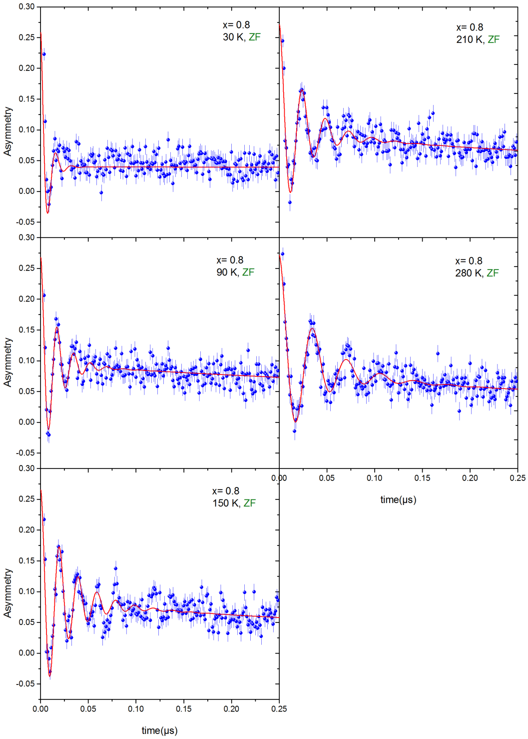

Figure B.6: Zero field μSR spectra of the $Fe_{0.2}Cu_{0.8}Cr_2S_4$ ($x = 0.8$) at various temperatures.

Bibliography

G. Allodi, M. Cestelli Guidi, R. De Renzi, A. Caneiro, and L. Pinsard. Ultraslow Polaron Dynamics in Low-Doped Manganites from $^{139}LaNMR-NQR$ muon spin rotation. *Physical Review Letters*, 87(12):127206, 2001.

C. D. Anderson and S. H. Neddermeyer. Cloud Chamber Observations of Cosmic Rays at 4300 Meters Elevation and Near Sea-Level. *Physical Review*, 50(4):263–271, 1936.

P. W. Anderson. Antiferromagnetism. Theory of superexchange interaction. *Physical Review*, 79(2):350–356, 1950.

J. Bertinshaw, C. Ulrich, A. Günther, F. Schrettle, M. Wohlauer, S. Krohns, M. Reehuis, A. J. Studer, M. Avdeev, D. V. Quach, J. R. Groza, V. Tsurkan, A. Loidl, and J. Deisenhofer. $FeCr_2S_4$ in magnetic fields: possible evidence for a multiferroic ground state. *Scientific reports*, 4:6079, 2014.

N. Blaes, H. Fischer, and U. Gonser. Analytical expression for the Mössbauer line shape of ^{57}Fe in the presence of mixed hyperfine interactions. *Nuclear Instruments and Methods in Physics Research Section B: Beam Interactions with Materials and Atoms*, 9(2):201–208, 1985.

S. Blundell. *Magnetism in Condensed Matter*. Oxford Master Series in Condensed Matter Physics. OUP Oxford, 2001.

S. J. Blundell. Spin-polarized muons in condensed matter physics. *Contemporary Physics*, 40(3):175–192, 1999.

W. H. Bragg. The structure of the spinel group of crystals. *Philosophical Magazine Series 6*, 30(176):305–315, 1915.

R. A. Brand, H. Georges-Gibert, J. Hubsch, and J. A. Heller. Ferrimagnetic to spin glass transition in the mixed spinel $Mg_{1+t}Fe_{2-2t}Ti_tO_4$: a Mossbauer and DC susceptibility study. *Journal of Physics F: Metal Physics*, 15(9):1987, 1985.

L. Brossard, J. L. Dormann, L. Goldstein, P. Gibart, and P. Renaudin. Second-order phase transition in $FeCr_2S_4$ investigated by Mössbauer spectroscopy: An example of orbital para-to-ferromagnetism transition. *Physical Review B*, 20(7):2933–2944, 1979.

N. Büttgen, J. Hemberger, V. Fritsch, A. Krimmel, M. Mücksch, H. A. K. Von Nidda, P. Lunkenheimer, R. Fichtl, V. Tsurkan, and A. Loidl. Orbital physics in sulfur spinels: Ordered, liquid and glassy ground states. *New Journal of Physics*, 6:1–24, 2004.

S. Chillal, M. Thede, F. J. Litterst, S. N. Gvasaliya, T. A. Shaplygina, S. G. Lushnikov, and A. Zheludev. Microscopic coexistence of antiferromagnetic and spin-glass states. *Physical Review B*, 87(22):220403, 2013.

K. Y. Choi, P. Lemmens, P. Scheib, V. Gnezdilov, Yu. G. Pashkevich, J. Hemberger, A. Loidl, and V. Tsurkan. Anomalous electronic, phonon, and spin excitations in the chalcogenide spinel $FeCr_2S_4$. *Journal of Physics: Condensed Matter*, 19(14):145260, 2007.

M. Conversi, E. Pancini, and O. Piccioni. Erratum: On the Disintegration of Negative Mesons. *Physical Review*, 71(8):557, 1947.

P. Dalmas de Reotier. Introduction to muon spin rotation and relaxation, 2010. URL `http://inac.cea.fr/Pisp/pierre.dalmas-de-reotier/introductionmuSR.pdf`.

J. D. Dunitz and L. E. Orgel. Electronic properties of transition-metal oxides-II. *Journal of Physics and Chemistry of Solids*, 3:318–323, 1957.

M. Eibschütz, S. Shtrikman, and Y. Tenenbaum. Magnetically induced electric field gradient in tetrahedral divalent iron: $FeCr_2S_4$. *Physics Letters A*, 24(11):563–564, 1967.

J. Engelke. Magnetic and orbital ordering in the Thiospinel $FeCr_2S_4$. Master's thesis, Technical University Braunschweig, 2010.

J. Engelke, F. J. Litterst, A. Krimmel, A. Loidl, F. E. Wagner, G. M. Kalvius, and V. Tsurkan. Spin re-orientation in $FeCr_2S_4$. *Hyperfine Interactions*, 202(1-3):57–61, 2011.

L. F. Feiner. Pseudo Jahn-Teller effect for a double: effect of a tetragonal field on the cubic $E \bigotimes \epsilon$ system. *Journal of Physics C: Solid State Physics*, 14(14):1955, 1981.

L. F. Feiner. Unified description of the cooperative Jahn-Teller effect in $FeCr_2S_4$ and the impurity Jahn-Teller effect in $CoCr_2S_4$:Fe^{2+}. *Journal of Physics C: Solid State Physics*, 15(7):1515, 1982.

R. Fichtl, V. Tsurkan, P. Lunkenheimer, J. Hemberger, V. Fritsch, H. A Krug Von Nidda, E. W. Scheidt, and A. Loidl. Orbital freezing and orbital glass state in $FeCr_2S_4$. *Physical Review Letters*, 94(2):1–4, 2005.

V. Fritsch, J. Deisenhofer, R. Fichtl, J. Hemberger, H. A. Krug von Nidda, M. Mücksch, M. Nicklas, D. Samusi, J. D. Thompson, R. Tidecks, V. Tsurkan, and A. Loidl. Anisotropic colossal magnetoresistance effects in $Fe_{1-x}Cu_xCr_2S_4$. *Physical Review B*, 67 (14):144419, 2003.

V. Fritsch, J. Hemberger, N. Böttgen, E. W. Scheldt, H. A. Krug Von Nidda, A. Loidl, and V. Tsurkan. Spin and Orbital Frustration in $MnSc_2S_4$ and $FeSc_2S_4$. *Physical Review Letters*, 92(11):2–5, 2004.

M. Gabay and G. Toulouse. Coexistence of Spin-Glass and Ferromagnetic Orderings. *Physical Review Letters*, 47(3):201–204, 1981.

J. R. Gabriel and S. L. Ruby. Computation of Mössbauer spectra. *Nuclear Instruments and Methods*, 36:23–28, 1965.

R. L. Garwin, L. M. Lederman, and M. Weinrich. Observations of the Failure of Conservation of Parity and Charge Conjugation in Meson Decays: the Magnetic Moment of the Free Muon. *Physical Review*, 105(4):1415–1417, 1957.

V. I. Goldanskii and R. H. Herber. *Chemical Applications of Mössbauer Spectroscopy*, volume 66. Academic press New Yourk and London, New York, 1968.

J. B. Goodenough. Jahn-Teller distortions induced by tetrahedral-site Fe^{2+} ions. *Journal of Physics and Chemistry of Solids*, 25:151–160, 1964.

J. B. Goodenough. Tetrahedral-site copper in chalcogenide spinels. *Solid State Communications*, 5(8):577–580, 1967.

J. B. Goodenough. Descriptions of outer d electrons in thiospinels. *Solid State Communications*, 6:i, 1968.

J. A. Ramos Guivar, E. A. Sanches, F. Bruns, **E. Sadrollahi** and M. A. Morales, E. O. López, and F. J. Litterst. Vacancy ordered γ-Fe_2O_3 nanoparticles functionalized with nanohydroxyapatite: XRD, FTIR, TEM, XPS and Mössbauer studies. *Applied Surface Science*, 389:721 – 734, 2016.

P. Gütlich. Fifty Years of Mössbauer Spectroscopy in Solid State Research - Remarkable Achievements, Future Perspectives. *Zeitschrift für anorganische und allgemeine Chemie*, 638(1):15–43, 2012.

P. Gütlich, E. Bill, and A. X. Trautwein. *Mössbauer Spectroscopy and Transition Metal Chemistry*. Springer Berlin Heidelberg, Berlin, Heidelberg, 2011. ISBN 978-3-540-88427-9. doi: 10.1007/978-3-540-88428-6.

G. Haacke and L. C. Beegle. Magnetic properties of the spinel system $Fe_{1-x}Cu_xCr_2S_4$. *Journal of Physics and Chemistry of Solids*, 28(9):1699–1704, 1967.

G. Haacke and A. J. Nozik. Mössbauer effect in $Fe_{1-x}Cu_xCr_2S_4$. *Solid State Communications*, 6(6):363–365, 1968.

Lennart Häggström. Determination of hyperfine parameters 1/2 → 3/2 transitions in Mössbauer spectroscopy. Technical report, University of Uppsala, Sweden, 1974. URL `https://inis.iaea.org/search/search.aspx?orig{_}q=RN:6175966`.

F. S. Ham. Dynamical Jahn-Teller Effect in Paramagnetic Resonance Spectra: Orbital Reduction Factors and Partial Quenching of Spin-Orbit Interaction. *Physical Review*, 138(6A):A1727–A1740, 1965.

S. W. Han, J. S. Kang, S. S. Lee, G. Kim, S. J. Kim, C. S. Kim, J. Y. Kim, H. J. Shin, K. H. Kim, and J. I. Jeong. Photoemission, soft x-ray absorption, and magnetic circular dichroism spectroscopy study of $Fe_{1-x}Cu_xCr_2S_4$ ($0.1 \leq x \leq 0.5$) spinel sulfides. *Journal of Physics: Condensed Matter*, 18(31):7413, 2006.

F. Hartmann-Boutron and P. Imbert. Mossbauer Study of the Electronic and Magnetic Properties of Fe^{2+} Ions in Some Spinel‚ÄêType Compounds. *Journal of Applied Physics*, 39(2):775–785, 1968.

K. M. Hasselbach and H. Spiering. The average over a sphere. *Nuclear Instruments and Methods*, 176(3):537–541, 1980.

R. S. Hayano, Y. J. Uemura, J. Imazato, N. Nishida, T. Yamazaki, and R. Kubo. Zero-and low-field spin relaxation studied by positive muons. *Physical Review B*, 20(3):850–859, 1979.

R. H. Heffner, J. E. Sonier, D. E. MacLaughlin, G. J. Nieuwenhuys, G. Ehlers, F. Mezei, S. W. Cheong, J. S. Gardner, and H. Röder. Observation of two time scales in the ferromagnetic manganite $La_{1-x}Ca_xMnO_3$, $x \approx 0.3$. *Physical Review Letters*, 85(15):3285–3288, 2000.

R. H. Heffner, D. E. MacLaughlin, G. J. Nieuwenhuys, and J. E. Sonier. The origin of multiple spin-relaxation channels below the metal‚Äìinsulator transition in ferromagnetic colossal magnetoresistance (CMR) manganites. *Journal of Physics: Condensed Matter*, 16(40):S4541, 2004.

G. R. Hoy. Effective Field Parameters in Iron Mössbauer Spectroscopy. *The Journal of Chemical Physics*, 47(3):961, 1967.

G. R. Hoy and K. P. Singh. Magnetically Induced Quadrupole Interactions in $FeCr_2S_4$. *Physical Review*, 172(2):514–519, 1968.

G. H. Jonker and J. H. Van Santen. Ferromagnetic compounds of manganese with perovskite structure. *Physica*, 16(3):337–349, 1950.

G. M. Kalvius, O. Hartmann, A. Krimmel, F. E. Wagner, R. Wäppling, V. Tsurkan, H. a. Krug von Nidda, and A. Loidl. Spin-lattice instability in the chromium sulfur spinel $Fe_{0.5}Cu_{0.5}Cr_2S_4$. *Journal of Physics: Condensed Matter*, 20(25):252204, 2008.

G. M. Kalvius, A. Krimmel, O. Hartmann, R. Wäppling, F. E. Wagner, F. J. Litterst, V. Tsurkan, and A. Loidl. Low temperature incommensurately modulated and noncollinear spin structure in $FeCr_2S_4$. *Journal of Physics: Condensed Matter*, 22(5):052205, 2010.

G. M. Kalvius, A. Krimmel, R. Wäppling, O. Hartmann, F. J. Litterst, F. E. Wagner, V. Tsurkan, and A. Loidl. Magnetism of the chromium thio-spinels $Fe_{1-x}Cu_xCr_2S_4$ studied using muon spin rotation and relaxation. *Journal of physics. Condensed matter : an Institute of Physics journal*, 25(18):186001, 2013.

J. Kanamori. Superexchange interaction and symmetry properties of electron orbitals. *Journal of Physics and Chemistry of Solids*, 10(2-3):87–98, 1959.

S. J. Kim, B. S. Son, B. W. Lee, and C. S. Kim. Mössbauer studies of dynamic Jahn-Teller relaxation on the *Cu*-substituted sulfur spinel. *Journal of Applied Physics*, 95(11 II): 6837–6839, 2004.

P. J. C. King, S. P. Cottrell, S. F. J. Cox, G. H. Eaton, A. D. Hillier, J. S. Lord, F. L. Pratt, T. Lancaster, and S. J. Blundell. New science with pulsed muons-development ideas at ISIS. *Physica B: Condensed Matter*, 326(1-4):260–264, 2003.

Z. Klencsár, E. Kuzmann, Z. Homonnay, Z. Németh, I. Virág, M. Kühberger, G. Gritzner, and A. Vértes. Mössbauer study of Cr-based chalcogenide spinels $Fe_{1-x}Cu_xCr_2S_4$. *Physica B: Condensed Matter*, 358(1-4):93–102, 2005.

H. A. Kramers. L'interaction Entre les Atomes Magnétogènes dans un Cristal Paramagnétique. *Physica*, 1(1-6):182–192, 1934.

A. Krimmel, M. Mücksch, V. Tsurkan, M. M. Koza, H. Mutka, C. Ritter, D. V. Sheptyakov, S. Horn, and A. Loidl. Magnetic ordering and spin excitations in the frustrated magnet $MnSc_2S_4$. *Physical Review B*, 73(1):014413, 2006.

R. Kubo. A stochastic theory of spin relaxation. *Hyperfine Interactions*, 8(4-6):731–738, 1981.

K. I. Kugel and D. I. Khomskii. The Jahn-Teller effect and magnetism: transition metal compounds. *Soviet Physics Uspekhi*, 25(4):231, 1982. URL `http://stacks.iop.org/0038-5670/25/i=4/a=R03`.

W. Kündig. Evaluation of Mössbauer spectra for ^{57}Fe. *Nuclear Instruments and Methods*, 48(2):219–228, 1967.

K. Lagarec and D. G. Rancourt. Recoil-Mössbauer spectral analysis software for Windows. *University of Ottawa, Ottawa, ON*, 1998.

O. Lang, C. Felser, R. Seshadri, F. Renz, J. M. Kiat, J. Ensling, P. Gütlich, and W. Tremel. Magnetic and Electronic Structure of the *CMR* Chalcospinel $Fe_{0.5}Cu_{0.5}Cr_2S_4$. *Advanced Materials*, 12(1):65–69, 2000.

F. K. Lotgering, R. P. Van Stapele, G. H. A. M. Van Der Steen, and J. S. Van Wierigen. Magnetic properties, conductivity and ionic ordering in $Fe_{1-x}Cu_xCr_2S_4$. *J. Phys. Chem. Solids*, 30(d):799–804, 1969.

F. K. Lotgering, A. M. van Diepen, and J. F. Olijhoek. Mössbauer spectra of iron-chromium sulphospinels with varying metal ratio. *Solid State Communications*, 17(9):1149–1153, 1975.

P. Majumdar and P. B. Littlewood. Dependence of magnetoresistivity on charge-carrier density in metallic ferromagnets and doped magnetic semiconductors. *Nature*, 395:479–481, 1998.

D. Maurer, V. Tsurkan, S. Horn, and R. Tidecks. Ultrasonic study of ferrimagnetic $FeCr_2S_4$: Evidence for low temperature structural transformations. *Journal of Applied Physics*, 93 (11):9173–9176, 2003.

D. S. McClure. The distribution of transition metal cations in spinels. *Journal of Physics and Chemistry of Solids*, 3(3-4):311–317, 1957.

M. Mertinat, V. Tsurkan, D. Samusi, R. Tidecks, and F. Haider. Low-temperature structural transition in $FeCr_2S_4$. *Physical Review B - Condensed Matter and Materials Physics*, 71 (10):2–5, 2005.

A. J. Millis, P. B. Littlewood, and B. I. Shraiman. Double Exchange Alone Does Not Explain the Resistivity of $La_{1-x}Sr_xMnO_3$. *Physical Review Letters*, 74(25):5144–5147, 1995.

E. Morenzoni. Physics with Muons from Atomic Physics to Condensed Matter Physics, 2017. URL `https://www.psi.ch/lmu/EducationLecturesEN/PhysicsWithMuons-E-Morenzoni-22-5-2017.pdf`.

R. L. Mössbauer. Recoilless Nuclear Resonance Absorption. *Annual Review of Nuclear Science*, 12(1):123–152, 1962.

O. Mustonen, S. Vasala, K. P. Schmidt, **E. Sadrollahi**, H. C. Walker, I. Terasaki, F. J. Litterst, E. Baggio-Saitovitch, and M. Karppinen. Tuning the $S = 1/2$ square-lattice antiferromagnet $\mathrm{Sr_2CuTe_{1-x}W_xO_6}$ from Néel order to quantum disorder to columnar order. *Phys. Rev. B*, 98:064411, Aug 2018a.

O. Mustonen, S. Vasala, **E. Sadrollahi**, K. P. Schmidt, C. Baines, H. C. Walker, I. Terasaki, F. J. Litterst, E. Baggio-Saitovitch, and M. Karppinen. Spin-liquid-like state in a spin-1/2 square-lattice antiferromagnet perovskite induced by d^{10}-d^0 cation mixing. *Nature Communications*, 9(1):1085, 2018b.

S. Najafishirtari, A. Lak, C. Guglieri, S. Marras, R. Brescia, S. Fiorito, **E. Sadrollahi**, Fred Jochen Litterst, Teresa Pellegrino, Liberato Manna, and Massimo Colombo. Manipulating the morphology of the nano oxide domain in aucu,Äìiron oxide dumbbell-like nanocomposites as a tool to modify magnetic properties. *RSC Adv.*, 8:22411–22421, 2018.

S. Nishikawa. Structure of Some Crystals of Spinel Group. *Proceedings of the Tokyo Mathematico-Physical Society. 2nd Series*, 8(7):199–209, 1915.

H. M. Palmer and C. Greaves. Structural, magnetic and electronic properties of $Fe_{0.5}Cu_{0.5}Cr_2S_4$. *Journal of Materials Chemistry*, 9(3):637–640, 1999.

M. S. Park, S. K. Kwon, S. J. Youn, and B. I. Min. Half-metallic electronic structures of giant magnetoresistive spinels: $Fe_{1-x}Cu_xCr_2S_4$ ($x = 0.0, 0.5, 1.0$). *Phys. Rev. B*, 59(15): 10018–10024, 1999.

PSI. General Purpose Surface-Muon Instrument (*GPS*), 2017. URL `https://www.psi.ch/smus/gps`.

P. Radaelli, M. Marezio, and H. Hwang. Charge localization by static and dynamic distortions of the octahedra in perovskite manganites. *Physical Review B - Condensed Matter and Materials Physics*, 54(13):8992–8995, 1996.

A. P. Ramirez, R. J. Cava, and J. Krajewski. Colossal magnetoresistance in *Cr*-based chalcogenide spinels, 1997.

J. A. Ramos Guivar, **E. Sadrollahi**, D. Menzel, E. G. Ramos Fernandes, E. O. López, M. Morales Torres, J. M. Arsuaga, A. Arencibia, and F. J. Litterst. Magnetic, structural and surface properties of functionalized maghemite nanoparticles for copper and lead adsorption. *RSC Advances*, 7(46):28763–28779, 2017.

W. L. Roth. Magnetic properties of normal spinels with only a-a interactions. *Le Journal de Physique*, 25(5):507–515, 1964.

M. B. Salamon and M. Jaime. The physics of manganites: Structure and transport. *Reviews of Modern Physics*, 73(3):583–628, 2001.

D. K. Seo, M. H. Whangbo, and M. A. Subramanian. Electronic band structure study of colossal magnetoresistance in $Tl_2Mn_2O_7$. *Solid State Communications*, 101(6):417–421, 1997.

C. Shen, Z. Yang, R. Tong, G. Li, B. Wang, Y. Sun, and Y. Zhang. Magnetic anisotropy-induced spin-reorientation in spinel $FeCr_2S_4$. *Journal of Magnetism and Magnetic Materials*, 321(19):3090–3092, 2009.

Y. Shimakawa, Y. Kubo, T. Manako, Y. V. Sushko, D. N. Argyriou, and J. D. Jorgensen. Structural and magnetotransport properties of the colossal magnetoresistance material $Tl_2Mn_2O_7$. *Physical Review B*, 55(10):6399–6404, 1997.

G. Shirane, D. E. Cox, and S. J. Pickart. Magnetic Structures in $FeCr_2S_4$ and $FeCr_2O_4$. *Journal of Applied Physics*, 35(3):954–955, 1964.

K. E. Sickafus, J. M. Wills, and N. W. Grimes. Structure of spinel. *Journal of the American Ceramic Society*, 82(12):3279–3292, 1999.

M. R. Spender and A. H. Morrish. A low temperature transition in $FeCr_2S_4$. *Solid State Communications*, 11(10):1417–1421, 1972.

M. A. Subramanian, B. H. Toby, A. P. Ramirez, W. J. Marshall, A. W. Sleight, and G. H. Kwei. Colossal Magnetoresistance Without Mn^{3+}/Mn^{4+} Double Exchange in the Stoichiometric Pyrochlore $Tl_2Mn_2O_7$. *Science*, 273(5271):81–84, 1996.

A. Suter and B. M. Wojek. musrfit: A free platform-independent framework for μSR data analysis. *Physics Procedia*, 30:69–73, 2011.

M. Tachibana, K. Akiyama, M. Yoshizawa, H. Kawaji, and T. Atake. Strongly correlated behavior in magnetoresistive $Fe_{1-x}Cu_xCr_2S_4$ spinels. *Physical Review B*, 71(18):180403, 2005.

C. Taubitz. *Investigation of the magnetic and electronic structure of* Fe *in molecules and chalcogenide systems*. PhD thesis, Osnabrück, 2010.

C. Taubitz, K. Kuepper, M. Raekers, V. R. Galakhov, V. Felea, V. Tsurkan, and M. Neumann. Reinvestigation of the *Fe*, *Cu* and *Cr* valences in $(FeCu)Cr_2S_4$ spinels. *physica status solidi (b)*, 246(7):1470–1475, 2009.

E. Sadrollahi, M. Kraken, N.C. Schmidt, F.J. Litterst, V. Tsurkan, A. Loidl, F. E. Wagner, and G.M. Kalvius. Magnetic and orbital order in the system $\mathrm{Fe}_{1-x}\mathrm{Cu}_x\mathrm{Cr}_2\mathrm{S}_4$ studied by Mössbauer spectroscopy. *DPG, Spring Meeting (Poster)*, 2014.

E. Sadrollahi, J. Engelke, F. J. Litterst, V. Tsurkan, A. Krimmel, A. Loidl, F. E. Wagner, and G. M. Kalvius. Mössbauer study of the Chromium thio-spinels $\mathrm{Fe}_{1-x}\mathrm{Cu}_x\mathrm{Cr}_2\mathrm{S}_4$. *ICAME (Poster)*, 2015.

E. Sadrollahi, J. Engelke, F. J. Litterst, V. Tsurkan, A. Loidl, and G. M. Kalvius. Magnetism of the Chromium thio-spinels $\mathrm{Fe}_{1-x}\mathrm{Cu}_x\mathrm{Cr}_2\mathrm{S}_4$ studied with Mössbauer spectroscopy and μSR. *Hyperfine interaction and their applications (Oral)*, 2016.

The Chemistry LibreTexts library. Introduction to Crystal Field Theory, 2017. URL `https://chem.libretexts.org/Core/Inorganic{_}Chemistry/Crystal{_}Field{_}Theory/Introduction{_}to{_}Crystal{_}Field{_}Theory`.

V. Tsurkan, M. Baran, R. S. Szymczak, H. Szymczak, and R. Tidecks. Spin-glass like states in the ferrimagnet $FeCr_2S_4$. *Physica B: Condensed Matter*, 296(4):301–305, 2001a.

V. Tsurkan, J. Hemberger, M. Klemm, S. Klimm, A. Loidl, S. Horn, and R. Tidecks. Ac susceptibility studies of ferrimagnetic $FeSc_2S_4$ single crystals. *Journal of Applied Physics*, 90(9):4639–4644, 2001b.

V. Tsurkan, V. Fritsch, J. Hemberger, A. Krimmel, M. Muecksch, N. Buettgen, H. A. Krug von Nidda, D. Samusi, S. Koerner, E. W. Scheidt, M. Honal, S. Horn, R. Tidecks, and A. Loidl. Orbital Glass in $FeCr_2S_4$. *Scientific Reports*, 4(1):6079, 2004.

V. Tsurkan, J. Groza, G. Bocelli, D. Samusi, P. Petrenco, V. Zestrea, M. Baran, R. Szymczak, H. Szymczak, M. Mücksch, F. Haider, and R. Tidecks. Influence of cation substitution on the magnetic properties of the $FeCr_2S_4$ ferrimagnet. *Journal of Physics and Chemistry of Solids*, 66(11):2040–2043, 2005.

V. Tsurkan, O. Zaharko, F. Schrettle, C. Kant, J. Deisenhofer, H. A. Krug Von Nidda, V. Felea, P. Lemmens, J. R. Groza, D. V. Quach, F. Gozzo, and A. Loidl. Structural anomalies and the orbital ground state in $FeCr_2S_4$. *Physical Review B - Condensed Matter and Materials Physics*, 81(18):1–7, 2010.

Y. J. Uemura. Probing spin glasses with zero-field μSR. *Hyperfine Interactions*, 8(4-6): 739–748, 1981.

Y. J. Uemura, T. Yamazaki, D. R. Harshman, M. Senba, and E. J. Ansaldo. Muon-spin relaxation in $AuFe$ and $CuMn$ spin glasses. *Physical Review B*, 31(1):546–563, 1985.

R. Vali and **E. Sadrollahi**. Spin-dependent transmission of holes through a semiconductor quantum wire with multiple stub. *Physica E: Low-dimensional Systems and Nanostructures*, 40(10):3155 – 3159, 2008.

A. M. van Diepen and R. P. van Stapele. Mössbauer Effect of ^{57}Fe in Cubic $Cd_{0.98}Fe_{0.02}Cr_2S_4$. *Physical Review B*, 5(7):2462–2466, 1972.

Wikibooks. Introduction to Inorganic Chemistry, 2017. URL `https://en.wikibooks.org/wiki/Introduction{_}to{_}Inorganic{_}Chemistry/Ionic{_}and{_}Covalent{_}Solids{_}-{_}Structures`.

C. Zener. Interaction between the d-shells in the transition metals. II. Ferromagnetic compounds of manganese with Perovskite structure. *Physical Review*, 82(3):403–405, 1951.

Acknowledgment

My journey of PhD has been a life changing experience for me and it would not have been possible without constant support and guidance from my supervisor Prof. Dr. F. J. Litterst. Apart from his academic supervision, I found him extremely inspiring, who ignited the quest for knowledge in me. I am in deficit of word to write about his role in this thesis and my life.

Prof. Litterst gave me the opportunity to spend some productive weeks with Prof. Dr. E. Baggio Saitovitch's research group at the Centro Brasileiro de Pesquisas Físicas in the beautiful city of Rio de Janeiro. Her efforts to make a great time there was admirable.

I had the precious chance to collaborate with several research groups. I would like to thank Dr. D. Menzel (IPKM) for magnetization measurements, Ms. N. Schmidt for using her earlier measured Mössbauer data, Dr. V. Tsurkan for preparation of samples and their structural characterization, him and the Augsburg group of Prof. Dr. A. Loidl for valuable fundamental information on relevant contemporary research and previous data, Prof. Dr. G. M. Kalvius for allowing the reanalysis of previously measured μSR data. Special thanks go to the colleagues at PSI for their help and patience for a newcomer to the μSR experiments at the accelerator.

The members of the IPKM had a big influence on the great working atmosphere in the institute. Special thanks to Ms. Bosse for preparing the paperwork for me, which included, renewal of my contract, extension of my visa etc. I am grateful to Dr. Mathias Kraken for his support and encouragement throughout this tenure. K. P. Schmidt was helping me with the final formatting and printing of my thesis. I thank to Mr. Franz Körkemeyer for installing the ***musr*** fit program and miscellaneous help regarding software problems. I extend my thanks to all those helpful people from the workshop, who helped me to prepare the sample boxes for Mössbauer measurements.

I am grateful for financial support by a joint DFG-FAPERJ project DFG Li-244/12, the DAAD financial support for my stays at Rio de Janeiro and the lower Saxony Grant of Prof. Litterst.

I owe a special thanks to my family. Words cannot express how grateful I am to my mother, father, my brother Reza, my sisters Alemeh and Fatemeh for all of the sacrifices they made on my behalf. Special thanks to my sister-in-law Hanieh, for being next to me in first hard moments, when I entered to Germany.

Lastly, I am highly indebted to my husband Majid for his patience and strong persistent support. I must say, my beloved son Sajjad, is a big mental strength for me.

Curriculum Vitae

Personal Information

Elaheh Sadrollahi
Institut für Physik der kondensierten Materie, TU Braunschweig,
Mendelssohnstrasse 3
38106 Braunschweig

Tel.: +49 (0)531 391-5128
E-Mail: e.sadrollahi@tu-bs.de

Date of birth: 21. 09. 1983 in Damghan, Iran

Academic Background

Since 2013	**PhD student in group of Prof. Dr. Jochen Litterst at TU Braunschweig.** The title of my doctoral thesis: $Fe_{1-x}Cu_xCr_2S_4$ Studied by Mössbauer Spectroscopy and Muon Spin Rotation and Relaxation.
2005–2008	**M.Sc. of Solid State Physics, Damghan University, Iran.** The title of my M.Sc. thesis: Spin Transport through GaAs/GaMnAs Quantum Wire.
2001–2005	**B.Sc. of Solid State Physics, Damghan University, Iran.**

Research Interest

Magnetism in correlated electron systems and nanomaterials studied by Mössbauer spectroscopy, and muon spin rotation and relaxation.

Publications

2008	R. Vali and **E. Sadrollahi**. Spin-dependent transmission of holes through a semiconductor quantum wire with multiple stub. *Physica E: Low-dimensional Systems and Nanostructures*, 40(10):3155 – 3159, 2008
2016	J. A. Ramos Guivar, E. A. Sanches, F. Bruns, **E. Sadrollahi** and M. A. Morales, E. O. López, and F. J. Litterst. Vacancy ordered γ-Fe_2O_3 nanoparticles functionalized with nanohydroxyapatite: XRD, FTIR, TEM, XPS and Mössbauer studies. *Applied Surface Science*, 389:721 – 734, 2016

2017	J. A. Ramos Guivar, **E. Sadrollahi**, D. Menzel, E. G. Ramos Fernandes, E. O. López, M. Morales Torres, J. M. Arsuaga, A. Arencibia, and F. J. Litterst. Magnetic, structural and surface properties of functionalized maghemite nanoparticles for copper and lead adsorption. *RSC Advances*, 7(46):28763–28779, 2017
2018	O. Mustonen, S. Vasala, **E. Sadrollahi**, K. P. Schmidt, C. Baines, H. C. Walker, I. Terasaki, F. J. Litterst, E. Baggio-Saitovitch, and M. Karppinen. Spin-liquid-like state in a spin-1/2 square-lattice antiferromagnet perovskite induced by d^{10}-d^0 cation mixing. *Nature Communications*, 9 (1):1085, 2018b
2018	O. Mustonen, S. Vasala, K. P. Schmidt, **E. Sadrollahi**, H. C. Walker, I. Terasaki, F. J. Litterst, E. Baggio-Saitovitch, and M. Karppinen. Tuning the $S = 1/2$ square-lattice antiferromagnet $Sr_2CuTe_{1-x}W_xO_6$ from Néel order to quantum disorder to columnar order. *Phys. Rev. B*, 98: 064411, Aug 2018a
2018	S. Najafishirtari, A. Lak, C. Guglieri, S. Marras, R. Brescia, S. Fiorito, **E. Sadrollahi**, Fred Jochen Litterst, Teresa Pellegrino, Liberato Manna, and Massimo Colombo. Manipulating the morphology of the nano oxide domain in aucu,Äìiron oxide dumbbell-like nanocomposites as a tool to modify magnetic properties. *RSC Adv.*, 8:22411–22421, 2018

Presentation at Conferences

2014	**E. Sadrollahi**, M. Kraken, N.C. Schmidt, F.J. Litterst, V. Tsurkan, A. Loidl, F. E. Wagner, and G.M. Kalvius. Magnetic and orbital order in the system $Fe_{1-x}Cu_xCr_2S_4$ studied by Mössbauer spectroscopy. *DPG, Spring Meeting (Poster)*, 2014
2015	**E. Sadrollahi**, J. Engelke, F. J. Litterst, V. Tsurkan, A. Krimmel, A. Loidl, F. E. Wagner, and G. M. Kalvius. Mössbauer study of the Chromium thio-spinels $Fe_{1-x}Cu_xCr_2S_4$. *ICAME (Poster)*, 2015
2016	**E. Sadrollahi**, J. Engelke, F. J. Litterst, V. Tsurkan, A. Loidl, and G. M. Kalvius. Magnetism of the Chromium thio-spinels $Fe_{1-x}Cu_xCr_2S_4$ studied with Mössbauer spectroscopy and μSR. *Hyperfine interaction and their applications (Oral)*, 2016

Participation in μSR Projects at PSI

Magnetic phases in the double perovskites $La_{2-x}Ca_xCoIrO_6$ ($x = 0.2$ and 0.8) and $La_{1.5}A_{0.5}CoMnO_6$ ($A = Ca, Sr, Ba$).

μSR study of $Sr_2CuTe_{1-x}W_xO_6$.

Magnetic phases in the new skyrmion host compound GaV_4S_8.

Magnetism in a new family of transition metal antimony oxofluorides $M_3Sb_4O_6F_6$ (M = Co, Ni).